# Effect of strength mismatch on fracture behavior of ferrite-austenite interface in Ni-base alloy dissimilar metal welds

**Teemu Sarikka**

Aalto University

# Effect of strength mismatch on fracture behavior of ferrite-austenite interface in Ni-base alloy dissimilar metal welds

**Teemu Sarikka**

A doctoral dissertation completed for the degree of Doctor of Science (Technology) to be defended, with the permission of the Aalto University School of Engineering, at a public examination held at the lecture hall M1 of the Aalto University on the 30th of September 2016 at 12:00.

**Aalto University**
**School of Engineering**
**Department of Mechanical Engineering**
**Engineering Materials**

NORDIC ECOLABEL

441    697
Printed matter

**Abstract**

Dissimilar metal welds (DMW) are extensively used in energy production applications, such as nuclear power plants (NPP), to join the ferritic steel nozzles of reactor pressure vessels (RPV) to the austenitic stainless steel pipings using different types of safe-end designs. Traditional, V-groove safe-end designs made using filler metal Alloys 82/182 are being replaced by modern safe-end designs manufactured using narrow gap (NG) welding technique with filler metal Alloy 52/152. The higher Cr-containing Alloy 52/152 provides improved corrosion resistance, especially resistance to stress corrosion cracking (SCC), and NG technique provides technical and economical benefits.

The difference in filler metal and NG technique require thorough understanding of the metallurgical and mechanical properties of the resulting weld as the changes may have an effect on the structural integrity of the DMW. The objective of this thesis was to determine the microstructural properties, mechanical properties, and mechanical mismatch across a ferritic-austenitic interface of a traditional V-groove DMW and a modern NG DMW. The mechanical mismatch was determined using tensile testing and microhardness and nanoindentation testing. The different mismatch states were compared to the fracture mechanical behavior of the ferritic-austenitic interface.

Microstructural properties of the different DMWs were found to differ from each other in terms of the existence of a carbon-depleted zone (CDZ) and a narrow carbon pile-up near the fusion boundaries of the DMWs. The existence of the CDZ and carbon pile-up caused high mechanical mismatch at the fusion boundary region of the NG DMW and affected the fracture propagation behavior near the fusion boundary region of the NG DMW. The mechanical mismatch was observable with nanoindentation testing, but the tensile tests even with small-sized specimen did not reveal the high mechanical mismatch near the fusion boundary region.

**A″** Aalto-yliopisto

**Tiivistelmä**

**Tekijä**
Teemu Sarikka

**Väitöskirjan nimi**
Paikallisen yli-/alilujuuden vaikutus nikkelipohjaisten ferriittis-austeniittisten eriparihitsausliitosten murtumiskäyttäytymiseen

**Tiivistelmä**

Eriparihitsausliitoksia käytetään yleisesti erilaisissa energiantuotantoon liittyvissä sovelluksissa, kuten ydinvoimalaitoksissa, yhdistämään ferriittisen reaktoripaineastian yhteet austeniittiseen ruostumaton teräs putkistoon erilaisten safe-end-liitosten avulla. Perinteiset, nikkelipohjaista Alloy 82/182 lisäainetta käyttäen V-railoon valmistetut safe-end-liitokset on uusissa laitoksissa korvattu moderneilla, nikkelipohjaista Alloy 52/152 lisäainetta sisältävillä kapearailotekniikalla valmistetuilla safe-end-hitsausliitoksilla. Korkeakromisella Alloy 52/152 lisäaineella saavutetaan parempi korroosionkestävyys ja kapearailomenetelmän käytöstä saadaan sekä teknisiä että taloudellisia etuja.

Uuden hitsauslisäaineen ja modernin kapearailotekniikan käyttäminen eriparihitsausliitosten valmistuksessa vaatii liitoksen metallurgisten ja mekaanisten ominaisuuksien syvällistä ymmärtämistä, koska muutokset lisäaineessa ja hitsaustekniikassa vaikuttavat liitoksen rakenteelliseen eheyteen. Väitöstutkimuksen tavoitteena oli traditionaalisen sekä modernin safe-end-liitoksen mikrorakenteellisten ja mekaanisten ominaisuuksien sekä rajapinnan yli vallitsevan paikallisen yli-/alilujuustilan selvittäminen. Paikallinen yli-/alilujuus määritettiin vetokokeiden sekä mikrokovuus- ja nanoindentaatiokokeiden avulla ja eri mismatch-tiloja verrattiin rajapinnan murtumismekaaniseen käyttäytymiseen.

Eriparihitsausliitosten mikrorakenteelliset ominaisuudet erosivat toisistaan siten, että kapearailohitsin rajapinnasta löytyi hiiliköyhä vyöhyke sekä paikallinen hiilikasauma, joita ei ollut V-railoon valmistetussa traditionaalisessa eriparihitsausliitoksessa. Hiiliköyhä vyöhyke sekä hiilikasauma aiheuttivat korkean yli-/alilujuustilan hitsin rajapintaan ja siten vaikuttivat särön etenemiseen hitsin rajapinnassa. Yli-/alilujuus oli havaittavissa nanoindentaatiokokeiden tuloksista, mutta vetokoetulokset, edes pienellä sauvakoolla, eivät osoittaneet paikallisia eroja lujuudessa.

# Acknowledgements

Espoo, 17 August 2016
Teemu Sarikka

# Contents

# Original Features

The study consisted of microstructural, mechanical, and fracture mechanical characterization of ferritic-austenitic interfaces in two Ni-base dissimilar metal welds (DMW) representing two different safe-end designs connecting ferritic light water reactor pressure vessel nozzles to austenitic stainless steel pipings. The studied safe-end DMW designs were: (1) a traditional V-groove design representing a safe-end DMW of an older boiling water reactor pressure vessel (BWR-DMW) and (2) a moderm narrow-gap welded design representing a safe-end DMW of a modern pressurized water reactor pressure vessel (NG-DMW). The research focused on the effect of the local microstructural zones with varying mechanical properties on the fracture mechanical properties of the DMWs and the crack propagation behavior near the fusion boundary area. The following features are believed to be original:

1. Thorough microstructural and mechanical characterization of the DMW manufactured using narrow-gap welding technique.

2. A detailed comparison of the microstructural and mechanical properties of the NG-DMW to a traditional V-groove DMW design.

3. The use of the nanoindentation testing for characterization of the mechanical properties of the different structures near the fusion boundary region enhancing the precision of the testing results.

4. The microstructural characterization of the DMWs revealed the existence of a carbon-depleted zone and a narrow carbon pile-up near the fusion boundary of the NG-DMW.

5. The presence of the local microstructural zones near the fusion boundary area of the NG-DMW caused high hardness mismatch, which clearly affected the crack propagation behavior near the interface region and caused the crack to deviate and propagate towards and in the ferritic carbon-depleted zone, which was the microstructural zone with the lowest hardness in NG-DMW.

6. In the BWR-DMW interface, the crack deviated and propagated towards and in the austenitic side of the fusion boundary, which was the location with the lowest hardness.

7. The strength mismatch determined via tensile testing was not able to predict the crack propagation behavior near the fusion boundary. The hardness mismatch using nanoindentation predicted the crack propagation near the fusion boundary region properly due to significantly higher measurement resolution.

# List of Abbreviations and Symbols

| | |
|---|---|
| A | Elongation to fracture |
| $A_g$ | Uniform elongation |
| BCC | Body-centered cubic |
| BCT | Body-centered tetragonal |
| BU | Buttering layer |
| BWR | Boiling water reactor |
| CCT | Continuous-cooling transformation |
| CDF | Crack driving force |
| CDZ | Carbon-depleted zone |
| CGHAZ | Coarse grained heat-affected zone |
| CMOD | Crack-mouth-opening displacement |
| C(T) | Compact tension |
| CTE | Coefficient of thermal expansion |
| CTOD | Crack-tip-opening displacement |
| DMW | Dissimilar metal weld |
| DZ | Dilution zone |
| E | Elastic modulus, Young's modulus |
| EAC | Environmentally-assisted cracking |
| EBSD | Electron backscatter diffraction |
| EBSP | Electron backscatter diffraction pattern |
| EDS | Energy dispersive X-ray spectroscopy |
| EPFM | Elastic-plastic fracture mechanics |
| EPR | European pressurized water reactor |
| FAD | Failure assessment diagram |

| | |
|---|---|
| FAZ | Fully austenitic zone |
| FB | Fusion boundary |
| FBR | Fast breeder reactor |
| FCC | Face-centered cubic |
| FESEM | Field emission scanning electron microscope |
| FITNET FFS | European Fitness-for-service Network fitness for service procedure |
| FL | Fusion line |
| FSD | Forescattered detector |
| FZ | Fusion zone |
| GB | Grain boundary |
| GCR | Gas-cooled and graphite-moderated reactor |
| GMAW | Gas metal arc welding |
| GTAW | Gas tungsten arc welding |
| HAZ | Heat-affected zone |
| HVxx | Hardness in Vickers scale with applied load of xx kgf |
| IPF | Inverse pole figure |
| J | A line or surface integral that encloses the crack front from one crack surface to the other, J-integral |
| $J_{0.2mm}$ | J value at 0.2 mm crack extension |
| $J_{1mm}$ | J value at 1 mm crack extension |
| $J_Q$ | Interim J value at ductile fracture initiation |
| $J_{IC}$ | J value at ductile fracture initiation |
| JIS | Japanese Industrial Standard |
| K | Stress intensity factor |
| KAM | Kernel average mis-orientation |
| K-S | Kurdjumov-Sachs |
| LAS | Low-alloy steel |
| LEFM | Linear elastic fracture mechanics |
| LLD | Load-line displacement |
| LWGR | Light-water-cooled and graphite-moderated reactor |
| LWR | Light water reactor |

8

| | |
|---|---|
| M | The strength mismatch factor |
| $M_s$ | The starting temperature of martensite transformation |
| MAG | Metal active gas |
| MGB | Migrated grain boundary |
| MIG | Metal inert gas |
| MNZ | Martensitic zone |
| n | Strain hardening exponent |
| NG | Narrow-gap |
| NG-DMW | Narrow-gap dissimilar metal weld |
| NIZ | Near interface zone |
| PAW | Plasma arc welding |
| PHWR | Pressurized heavy-water reactor |
| PMZ | Partially melted zone |
| PWHT | Post-weld heat treatment |
| PWR | Pressurized water reactor |
| $R_{p0.2}$ | Yield strength/0.2 proof strength |
| $R_m$ | Ultimate tensile strength |
| RPV | Reactor pressure vessel |
| SAW | Submerged arc welding |
| SCC | Stress corrosion cracking |
| SE(B) | Single-edge bend |
| SEM | Scanning electon microscope |
| SGB | Solidification grain boundary |
| SIF | Stress intensity factor |
| SINTAP | Structural Integrity Assessment Procedures for European Industry |
| SMAW | Shielded metal arc welding |
| SS | Stainless steel |
| SSGB | Solidification subgrain boundary |
| SSYC | Small scale yielding correction |
| TIG | Tungsten inert gas |

| | |
|---|---|
| UMZ | Unmixed zone |
| WM | Weld metal |
| 3PB | Three point bend |
| $\sigma$ | Strength |
| $\sigma_y$ | Yield strength |
| $\sigma_U$ | Ultimate tensile strength |
| $\sigma_{BM}$ | Yield strength of base metal |
| $\sigma_{WM}$ | Yield strength of weld metal |

# 1 Introduction

The operational concept of a nuclear power plant (NPP) is to produce energy by using the heat generated by the fission reaction of the fissile elements occurring in the core of a nuclear power plant. The fission heat is used to heat up coolant, which is then vaporized and further lead to a turbine. The steam will spin the turbine bound to a generator, which will transform the turbine's kinetic energy into electricity. As of 2016, there are a total of 438 nuclear power reactors in operation producing about 380 000 $MW_e$, 2 reactors in long-term shutdown, and 68 reactors under construction (IAEA 2016). Nuclear reactors are divided into either fast reactors or thermal reactors depending on the energies of the fission neutrons used to maintain the controlled fission chain reaction. In the thermal reactors, the fission neutrons are slowed down from MeV energies into eV energies before causing a new fission reaction whilst in the fast reactors the fission reaction is maintained by the MeV energy-state fission neutrons.

Majority of the nuclear reactors in commercial use are light water reactors (LWR), which means that they use normal water both as a coolant and as a moderator. Two of the most commonly used LWR types are the boiling water reactor (BWR) and the pressurized water reactor (PWR). As of 2016, there are a total of 279 PWRs and 78 BWRs in operation worldwide (IAEA 2016). The other types of reactors in commercial use include pressurized heavy-water reactor (PHWR, 49 in operation), light-water-cooled and graphite-moderated reactor (LWGR, also known as RBMK, 15 in operation), gas-cooled and graphite-moderated reactor (GCR, 15 in operation), and fast breeder reactor (FBR, 2 in operation) (IAEA 2016).

Basically all thermal nuclear reactors contain the following basic components: a core, a moderator, a reflector, a control rod system, a thermal shield, a reactor pressure vessel (RPV), and a biological shield. The purpose of the core is to maintain the nuclear reaction itself and, thus, to produce the heat required to heat up the coolant. In thermal reactors, the core consists of fuel, moderator, and coolant. In PWRs and BWRs, the fuel is around $2 - 3$ wt. % $U_{235}$ enriched uranium oxide and water acts as a coolant and, also, as a moderator, whose purpose in thermal reactors is to slow down fast fission neutrons into thermal energies for better fission triggering. Reactor pressure vessel also contains reflector, whose purpose is to reflect a part of escaping neutrons back into the core, and control rods, which are constructed from strongly neutron-absorbing material, such as silver or cadmium. The purpose of the control rods is to absorb

the fission neutrons in a nuclear power plant shut down situation. Reactor pressure vessel contains all of the components mentioned above and shields them from the environment and vice versa. In addition to the reactor pressure vessel, thermal nuclear reactor also contains a biological shield to protect the personnel from radiation and a containment to prevent radiation leaks to the environment in case of an accident.

## 1.1 LWR safe-end DMWs

Dissimilar metal welds (DMW) are extensively used in NPPs to join the ferritic steel nozzles of RPVs, steam generators, and pressurizers to the austenitic stainless steel piping with different type safe-end designs (Hänninen et al. 2007).
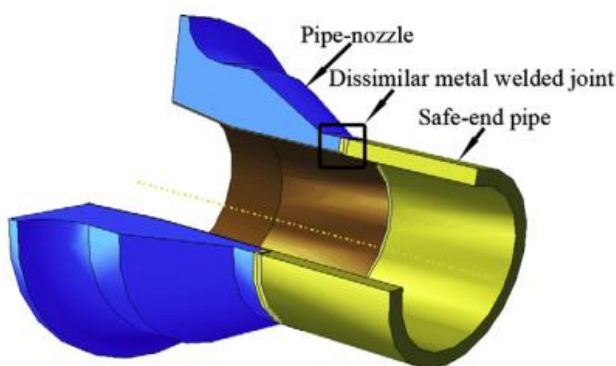


**Figure 1.1.** DMW joining the ferritic RPV nozzle to the austenitic safe-end (Wang et al. 2013A).

The ferritic steels are used as the structural material of the RPVs because of their relatively good mechanical properties and low cost whereas the austenitic stainless steels are used in components in which a good corrosion resistance is mandatory. The simultaneous use of these two types of crystallographically different materials makes the presence of DMWs in NPPs obligatory. One of the most critical DMW in an NPP is the one joining the RPV through its nozzle to the main coolant piping. For a number of reasons, the assembly is facilitated using a transition piece called safe-end in between the ferritic RPV nozzle and the austenitic stainless steel piping. The safe-ends are made of either austenitic stainless steel or Ni-base alloy, depending on the plant design. Figure 1.1 shows location of the DMW joining the RPV nozzle to the safe-end (Wang et al. 2013A). The main purpose of the safe-end is to enable the manufacturer to weld the difficult dissimilar metal joint at the RPV manufacturing site and, thus, leave the easier similar metal joint between the austenitic materials to be welded at the plant construction site.

## 1.2 V-groove DMW design

A conventional NPP safe-end weld design is a V-grooved DMW consisting of the heat-affected zones (HAZs) of the base metals, the fusion boundary area/near interface zone (NIZ), the interface between the weld metal/buttering and the base metals, the buttering layer, and the weld metal (Lippold and Kotecki 2005). The welds are manufactured by welding the buttering layer to the ferritic steel nozzle and then manufacturing the weld itself by starting at the root of the V-groove and gradually building up the weld pass by pass. The total amount of the filler metal required in manufacturing a V-grooved DMW is quite high since the cross-sectional area of the V-groove is large resulting in a large weld volume. The larger weld volumes result in higher manufacturing costs due to longer welding times (Biswas et al. 2010) as well as higher distortions due to weld shrinkage and higher residual stresses in the weld (Nelson and Lewis 1967, Biswas et al. 2010).

In traditional BWR designs, Alloy 600 based filler metal Alloy 82/182 is used in welding of the safe-end DMWs. Alloy 82/182 has a face-centered cubic (FCC) solid solution structure and the thermal expansion coefficient of Alloy 82/182 is between the thermal expansion coefficients of the ferritic RPV steel and austenitic stainless steel. In addition, Alloy 82/182 retards the carbon diffusion from the ferritic RPV steel to the weld metal significantly. The main problem with the Alloy 82/182 is that there has been concerns about the integrity of the Alloy 82/182 containing DMWs due to the Alloy 82/182's high susceptibility to stress corrosion cracking (SCC) in different LWR environments (Hänninen et al. 2007, Andresen and Morra 2008, Hänninen et al. 2008, Seifert et al. 2008, Karlsen and Pakarinen 2009, Hänninen et al. 2009, Hou et al. 2010B, Hänninen et al. 2011).

## 1.3 Narrow-gap DMW design

In modern PWR designs, the safe-end DMWs are manufactured using a narrow-gap (NG) welding technique without a separate buttering layer and with Alloy 690 based filler metal, Alloy 52 (Joly et al. 2014). The transition from Alloy 600 based filler metals to Alloy 690 based filler metals with higher Cr contents and the new weld design using NG welding technique are made to ensure the structural integrity of the welds as well as to decrease the joining costs due to the higher productivity of the narrow gap welding technique (Engelhard et al. 2000, Joly et al. 2014). NG weld is more economical than the conventional V-groove weld as it requires less welding consumable, shorter welding times, and reduces the volume of inspection. In addition, the reduced amount of weld metal and lower heat input used in NG welding leads to less shrinkage, distortion and smaller residual stresses/strains. A schematic image of the difference in the weld design and the reduction of the total weld volume due to the difference in the weld design is further presented in Figure 1.2.

**Narrow Gap Welding**
material: stainless steel
thickness: 90mm

**Conventional Weld**
material: carbon steel
thickness: 90mm

**Reduction of weld volume using GTA Narrow Gap Welding**
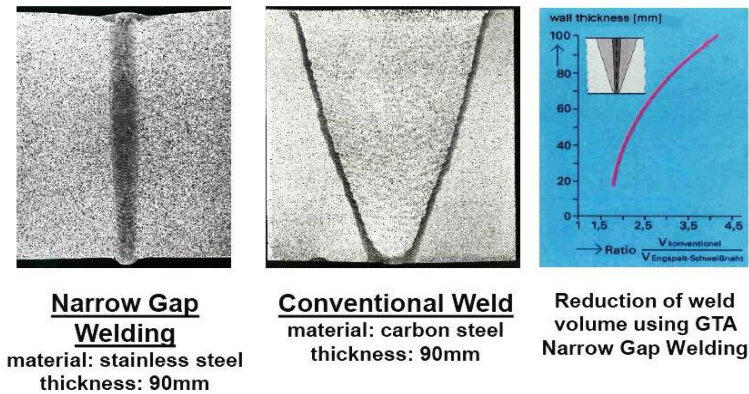
**Figure 1.2.** Reduction of the weld volume using NG-GTAW technique compared to a conventional V-groove weld. The reduction of weld volume, e.g. for 90 mm wall thickness, is a factor of 4 (Engelhard et al. 2000).

Similarly to the Alloy 82/182, Alloy 52 has an FCC solid solution structure, which is designed to take Ni, Cr, Cu, and Fe into solution upon dilution from the base metals whilst keeping a normal single-phase dendritic structure. Typically, a planar growth zone without precipitates appears at the weld interface followed by a cellular dendritic zone with precipitates in the interdendritic regions. Further in the weld metal, a columnar dendritic zone results from solidification along preferential growth directions and temperature gradients (Alexandrov et al. 2012). Compared to the Alloy 82/182, the Alloy 52 contains less Nb and more Ti and it has a smaller solidification temperature range (Naffakh et al. 2009). The main consequence is a coarser dendritic structure with less Nb-rich precipitates. The precipitates are mostly TiN and TiC, distributed in the interdendritic regions and at the grain boundaries (GB). Their number is lower than in Alloy 82/182 weld metal, although the precipitation is increased with post-weld heat treatment (PWHT) (Soares et al. 2007). Alloy 52 hardness is therefore in average lower than that of the Alloy 82/182 welds (Kuo and Lee 2002). In addition, it has a lower tensile strength (Lee and Jeng 2001). Due to its higher Cr content, Alloy 52 exhibits superior corrosion resistance compared to the Alloy 82/182. However, it can contain dynamically recrystallized zones, which may decrease SCC resistance (Morra et al. 2011).

## 1.4 Cracking in DMWs

Cracking associated with DMWs has been a constant problem and may typically occur near the fusion boundary either along the martensitic boundary adjacent to the fusion boundary or along the Type II boundary in the weld metal side of the fusion boundary (Nelson et al. 1999). A number of in-service cracking of dissimilar metal welds have been associated with Type II boundaries (Lippold et al. 2009). A major reason for the cracking susceptibility associated with the Type II boundaries is the difference in thermal expansion coefficients between the ferritic and austenitic sides of a bimetallic interface. The thermal expansion

mismatch combined with thermal cycling induces strains and, thus, makes the Type II boundary susceptible to cracking.

SCC is considered one of the most important ageing and cracking mechanism of Ni-base DMWs used in LWR applications. SCC field failures of LWR pressure boundary components have caused significant forced outages with associated high costs for repairs and replacement power as well as significant perssonel radiation exposures and occasional safety hazards (Hänninen et al. 2003). Most of the components and materials used in NPPs have been affected by SCC (Scott 1985, Hänninen et al. 1987, Danko 1987, Kilian and Roth 2002). Materials related failures in large components do not occur often, but when they do occur, outages may extent for months causing major capacity factor and economical losses (Hänninen 2003). Environmental parameters known to influence the SCC growth rate in LWR-type environements include temperature, pressure, solute species and their concentration and activity, pH value, electrochemical potential, and flow rate including stirring and mixing. In addition to the environmental parameters, SCC is influenced also by magnitude of the applied stress or stress intensity factor and strain rate, stress state, loading mode at the crack tip, alloy composition including impurity and tramp elements, metallurgical condition, and crack geometry (Jones 1987).

Even though Ni-base alloys are generally very resistant to SCC, it does occur under certain combinations of environment, microstructure, and stress (Hänninen 2003). Alloy 82/182 containing Ni-base DMWs have been found susceptible to SCC in BWR conditions where their microstructures and prevailing residual stresses and residual strains affect the SCC susceptibility (Hänninen et al. 2007). Alloy 82/182 Ni-base DMWs have also been found to suffer from the stress corrosion cracking susceptibility in primary water conditions (PWSCC) (Hänninen et al. 2007, Andresen and Morra 2008, Hänninen et al. 2008, Seifert et al. 2008, Karlsen and Pakarinen 2009, Hänninen et al. 2009, Hänninen et al. 2011). The SCC in Alloy 600 and corresponding filler metal Alloys 82/182 has been found to be mainly intergranular/interdendritic (Andresen et al. 2002, Peng et al. 2007, Seifert et al. 2008). Alloys 600/82/182 have been found clearly more susceptible to SCC than Alloy 690 and its filler metal Alloys 52/152, which show hardly any crack initiation susceptibility even in more agressive environments (Karlsen and Pakarinen 2009, Hänninen et al. 2009, Hänninen et al. 2011) and low SCC growth rates without a sufficient amount of cold-work induced in the material (Peng et al. 2012).

Currently there are no standards available to assess the structural integrity of DMW components or to test materials of DMWs. Therefore, ensuring safe service of a DMW component requires complete strength and fracture toughness based information from all microstructural zones of a DMW. To ensure the structural integrity of the modern DMWs, the changes in the weld design require extensive knowledge of the correlations and relationships between the dilution by the base metal and the compositional gradients of alloying elements, the resulting microstructures, and the resulting mechanical and fracture mechanical properties as well as the damage and failure mechanisms of the DMWs.

The properties affecting the structural integrity of a modern narrow-gap dissimilar metal safe-end weld manufactured using Alloy 52 filler metal have not yet been completely understood and the distribution of alloying elements and resulting microstructural characteristics as well as the widths of the local microstructural zones with different mechanical properties in the NIZ can be expected to differ from those of a conventional V-groove DMW manufactured using Alloy 82/182 filler metals.

# 2 Typical characteristics of Ni-base alloy DWMs

The importance of joining metallic alloys with different crystallographic properties has increased significantly during the past decades and the typical applications of DMWs include cladding for increased corrosion resistance and joining base metals that exhibit large differences in metallurgical, physical, and mechanical properties (Nelson et al. 1999). DMWs are commonly divided into two different types: joining of two different base metals, usually with addition of a third different filler metal; and joining similar base metals with different filler metal (Karlsson et al. 1995). The structure of a typical DMW consists of the HAZs of the base metals, the fusion boundary area/NIZ, the interface between the weld metal/buttering and the base metals, the buttering layer, and the weld metal (Lippold and Kotecki 2005). The exact chemical composition of the weld metal is affected by the chemical compositions of the base metals, the filler metal, and the welding procedure. The chemical composition of the weld metal and the chemistry and microstructural features of the near interface areas are the most important parts of a successful DMW.

DMWs have some unique characteristics due to the crystallographical and compositional differences between the joined metals. The composition variation across the fusion line from the composition of the base metal to the composition of the weld metal is often significant. This may lead to sudden changes in the microstructure, mechanical properties, and corrosion resistance across the fusion area. A characteristic feature of a DMW is the metallurgical and material property mismatch resulting from changing narrow compositional and microstructural zones with significantly different strength and toughness properties across the weld between two physically different materials. This results in metallurgical mismatch which affects the entire failure behavior of a DMW under external operational loads, not only from the crack initiation standpoint, but especially regarding the development of the crack driving force, subsequent crack growth behavior and development of local plastic constraint that can result in crack path deviation (Nevasmaa et al. 2000, Faidy et al. 2004, Laukkanen et al. 2007). The metallurgical mismatch can also result in the formation of, for example, a Type II boundary paralleling the fusion boundary in the weld metal side close to the fusion boundary. Also, a characteristic typical to DMWs is the formation of residual stress distribution caused by, in addition to the weld shrinkage, the unequal values of thermal expansion coefficients between the

joined metals. All these characteristics result in a gradient of microstructural and mechanical properties across the fusion boundary of a DMW (Hou et al. 2010A).

## 2.1 Welding metallurgy and microstructure of Ni-base alloy DMWs

All fusion welds contain a distinct fusion zone (FZ), HAZs in base metal, and unaffected base metal. In addition, a partially melted zone (PMZ) and an un-mixed zone (UMZ) may be present between the FZ and HAZ. The existence of these zones is due to the heat cycles caused by a fusion welding process. A schematic presentation of these zones and corresponding areas of a Fe-C-phase diagram is shown in Figure 2.1.
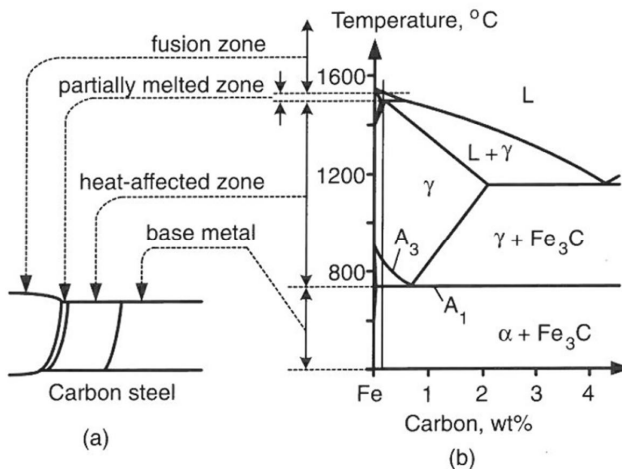


**Figure 2.1.** The different zones of a fusion weld (a) and Fe-C-phase diagram (b). The corresponding areas betweem the different weld zones and the phase diagram can be seen as the combination of figures (a) and (b) (Kou 2003).

The FZ is the completely melted portion of the weld after being heated above the liquidus temperature of the alloy during the welding, as shown in Figure 2.1. At the edge of the FZ, there may be a narrow zone in which the convection forces in the weld pool have not been able to overcome the friction forces of the fluid resulting in a possible UMZ. In a PMZ, which can be found between the FZ and HAZ, the temperature during the welding process has been between the solidus and the liquidus temperatures of the alloy resulting in a coexistence of liquid and solid phases during the welding process. The HAZ consists of the portion of the weld remained under the solidus temperature of the alloy to the portion of the weld in which the temperature and time have been high enough to cause the base material to go through a solid-state transformation. The FZ and HAZ are separated from each other by a fusion boundary (Messler 1999). In low-carbon steels, the formation of the different weld zones can be correlated to the Fe-C phase diagram if the kinetic effect of rapid heating on phase transformation during welding is neglected. As presented in Figure 2.1, it is possible to consider the HAZ to correspond to the area of the base metal where the temperature during

the welding process reaches between the alloy's eutectoid temperature $A_1$ and the peritectic temperature. Respectively, the PMZ can be defined as the area between the peritectic temperature and the liquidus temperature and the FZ as the area above the liquidus temperature. Due to fast changes in temperature in welding and changes in alloying elements, the phase changes often occur in practice at slightly higher temperatures than $A_1$ and $A_3$, denoted as $A_{C1}$ and $A_{C3}$.

### 2.1.1 HAZ of ferritic low-alloy steel base metal

The HAZ of low-carbon steel consists typically of three basic microstructural regions called partially grain-refined, grain-refined, and grain-coarsened region (Kou 2003). Figure 2.2 shows images of the different low-carbon steel HAZ regions of a gas-tungsten arc weld (GTAW) of 1018 steel and the corresponding formation of areas at a Fe-C-phase diagram. Partially grain-refined region forms when prior pearlite colonies transform to austenite and expand slightly into prior ferrite grains upon heating above $A_{C1}$. During cooling, this region decomposes into fine colonies and grains of pearlite and ferrite. The prior untransformed ferrite remains unchanged upon postweld cooling. In the grain-refined region, transformation of pearlite and ferrite into new grains of austenite is complete. Upon cooling, the austenite grains decompose into small pearlite colonies and ferrite grains. The distribution of the resulting pearlite and ferrite is nonuniform because rapid heating and cooling prevent the complete diffusion and leveling of carbon.

In the grain-coarsened region, the austenite grains formed from prior pearlite colonies and ferrite grains are larger because the temperature during welding has been well above the $A_{C3}$. Because of the high cooling rates in this highest-temperature HAZ region and the larger grain size, acicular ferrite, rather than blocky ferrite, may form at grain boundaries. This structure is often called a Widmanstätten structure (Messler 1999). In addition, such high temperatures lead to progressive dissociation of precipitates that finally go into solution. This increases the prior-austenite grain size and hardenability of the austenite. Large austenite grains formed at this temperature, combined with rapid cooling, encourage Widmanstätten ferrite and upper-bainite to form at the sides of the grains. Sufficient material hardenability coupled with very rapid weld cooling rates can finally lead to the formation of lower bainite and martensite into grain-coarsened region (Kou 2003).

If heating and cooling rates next to the fusion line are reasonably high, high-carbon martensite may form amongst the prior-pearlite colonies. The hardness of martensite is much higher than that of the surrounding ferrite and, thus, the martensite formation can significantly degrade the mechanical properties of the HAZ (Kou 2003). Martensite can be transformed into tempered martensite through PWHT. Tempering the martensite decreases the martensite's hardness and increases its ductility and, thereby, increases its mechanical properties. In general, the austenite that forms in the low-alloy steel (LAS) HAZ as a consequence of the base metal being heated above the $A_{C1}$ temperature will transform upon cooling to some combination of ferrite, acicular ferrite, Widmanstätten ferrite, pearlite, bainite, and martensite (Thewlis et al. 1997, Francis et al. 2007).
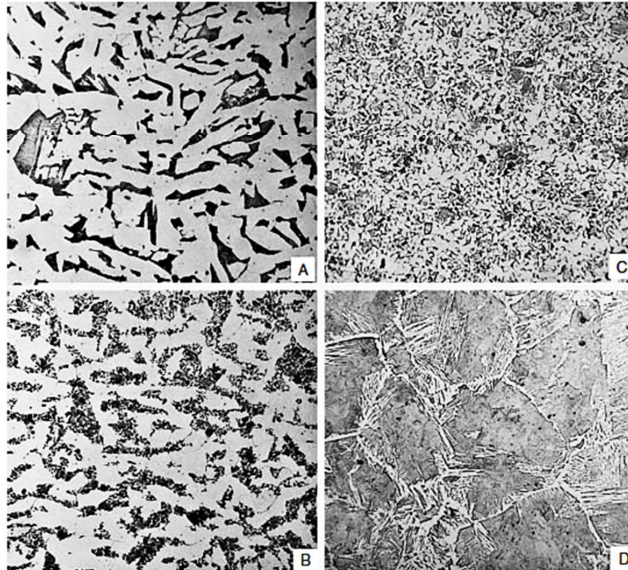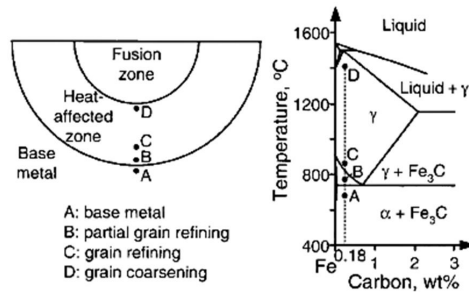
**Figure 2.2.** Microstructural characteristics of the different parts of the HAZ of a gas-tungsten arc weld of 1018 steel (Kou 2003).

### 2.1.2 Ni-base alloy fusion zone

Ni-base alloy weld metals are used frequently as a weld metal in dissimilar metal joints, such as ferritic-austenitic joints, for multiple reasons. The difference in coefficients of thermal expansion (CTE) between ferritic steel and austenitic stainless steel may lead to fatigue and creep failures in the HAZ of the ferritic steel (Lippold and Kotecki 2005). The CTE of Ni-base alloys is between the CTEs of ferritic steel and austenitic stainless steel. Therefore, as a results of using Ni-base alloy as a weld metal in a joint between ferritic and austenitic steels, the CTE gradient decreases across the weld joint, and further, the thermal stress originated from the differences in the CTEs across the joint distributes better. Ni-base alloy weld metals have a good corrosion resistance (Kiser 1990) and a good impact strength at low temperatures (Hilkes et al. 2004).

*2.1.2.1 Weld metal solidification*
In fusion welding, the existing base metal grains at the fusion boundary act as the substrate for nucleation. The grain structure near the fusion boundary of a

weld is dominated either by a mechanism known as epitaxial growth or by nucleation of new grains. When welding without a separate filler metal, nucleation in the liquid upon the substrate occurs so that the crystallographic orientation of the nucleation remains the same with the substrate grains. Such a growth initiation process, schematically presented in Figure 2.3, is called epitaxial growth (Kou 2003).
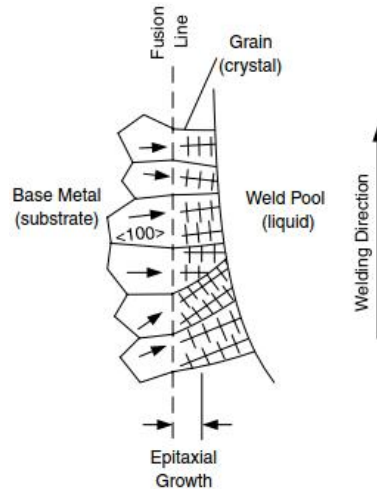


**Figure 2.3.** Epitaxial growth of weld metal near fusion line (Kou 2003).

When welding with a filler metal, the base metal and the weld metal differ from each other making the epitaxial growth not possible and, thus, new grains will have to nucleate at the fusion boundary (Kou 2003). When the crystal structures of the base metal and weld metal are different at the solidification temperature, nucleation of solid weld metal occurs in heterogeneous sites on the partially melted base metal at the fusion boundary (Nelson et al. 1999). As a result, the fusion boundary exhibits random misorientations between the base metal and the weld metal grains.

Farther away from the fusion boundary in the bulk weld metal the grain structure resulting from the solification is dominated by a mechanism known as competitive growth, schematically presented in Figure 2.4. During the solidification of weld metal, the resulting grains tend to grow in the direction perpendicular to the weld pool boundary because that is the direction of the maximum temperature gradient (Kou 2003). Simultaneously, columnar dendrites or cells within each grain grow preferably in the easy-growth direction, which for both FCC and BCC materials is <100> (Chalmers 1964). Thus, during the weld metal solidification, the grains with their easy-growth direction perpendicular to the pool boundary will grow more easily and crowd out the grains with less favorable orientation relationship between the easy-growth direction and the weld pool boundary.
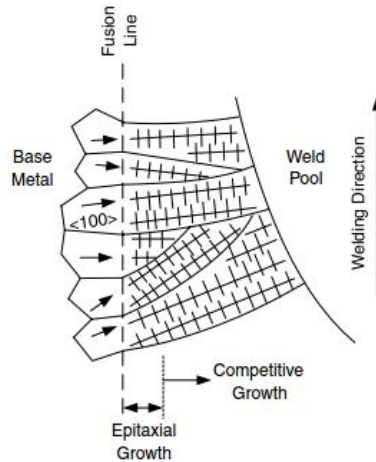
**Figure 2.4.** Epitaxial growth of weld metal near fusion line (Kou 2003).

### 2.1.2.2 Microstructure

A few different types of metallographically observable boundaries exist in Ni-base weld metals. These boundaries can be divided into solidification grain boundaries (SGB), solidification subgrain boundaries (SSGB), and migrated grain boundaries (MGB). Figure 2.5 shows a schematic image of the formation of different types of boundaries during and after welding process.
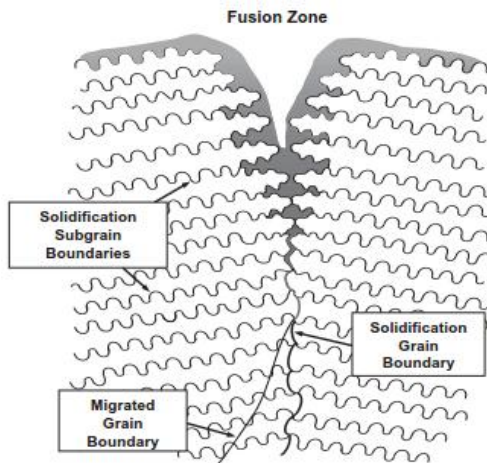


**Figure 2.5.** A schematic image showing the different types of boundaries observed in weld metals that solidify as austenite (Lippold et al. 1992).

SSGBs, also called as dendrite boundaries, are essentially boundaries which form when the dendrites within the same grain grow parallel to each other with a small crystallographic misorientation between each other. Thus, the crystallographic misorientation across an SSGB is quite low, typically less than five degrees (Lippold et al. 1992). SGBs form when the dendrite packets intersect with

one another. The SGBs usually have clearly higher crystallographic misorientation across them than the SSBGs because each of the intersecting dendrite packets have their independent growth direction (Lippold et al. 2009).

The third boundary type, the MGBs, are boundaries which form in a situation in which an SGB starts to migrate to a position with lower boundary energy. The chemical boundary still remains where the SGB was located after the solidification but the crystallographic boundary moves to a new, energetically more favorable location. MGBs usually occur only in fully austenitic weld metal because second phase particles are effective in pinning the SGBs and, thus, preventing the grain boundary migration (Lippold et al. 2009). The different boundaries are important due to many of the defects, impurities, and precipitates in weld metal microstructure being associated with the existence of the different boundaries.

### 2.1.2.3 Ni-base alloy phases and precipitates

The phase transformations observed in Ni-base alloys are dependant on the chemical composition of the alloy. The solid-solution strengthened Ni-base alloys are strengthened primarily by the addition of substitutional elements, such as Cr, Fe, Mo, W, and Cu, which provide solid-solution strengthening of the FCC crystal structure. The precipitiation hardenable alloys contain several percent Al and Ti and possibly substantial amounts of Nb (Davis 2000, Lippold et al. 2009).

The most typical non-carbide phases found from the Ni-base alloys are the intermetallic gamma prime (γ') and gamma double prime (γ") phases. The γ' has a composition of $Ni_3Al$ or $Ni_3(Al, Ti)$ with Co or Cr being able to replace some of the Ni and Fe being able to replace either Ni or Al. The γ' has an ordered FCC crystal structure with the lattice parameter similar to the Ni-base austenitic matrix, thus, making the γ' precipitates coherent with the γ matrix (Doi et al. 2004). The γ" has a composition of $Ni_3Nb$ with a body-centered tetragonal (BCT) crystal structure (Davis 2000, Lippold et al. 2009). The γ" is a metastable phase with a tendency of coarsening rapidly when exposed to temperatures above 700 °C. Also, when the lattice mismatch between the γ' phase and the surrounding γ matrix is high, extended exposure of alloy to temperatures above 700 °C causes formation of undesirable η ($Ni_3Ti$) and orthorhombic δ ($Ni_3Nb$) phases (Davis 2000).

Carbides are important precipitates in Ni-base alloys because their precipitation to the grain boundaries increases the strength of the grain boundaries. The carbide precipitation also has an effect on the corrosion behavior of the alloy through the formation of Cr-carbides and following depletion of Cr from the matrix (Davis 2000, Lee et al. 2004). The different types of carbides commonly present in Ni-base alloys are MC, $M_6C$, $M_7C_3$, and $M_{23}C_6$ carbides.

The MC carbides have an FCC crystal structure and tend to form at the end of solidification by eutectic-type reactions with the γ matrix (DuPont et al. 1988). Hence, the MC carbides are often distributed at the SGB and SSGB regions. The most prominent MC carbide formers are Nb and Ti due to their strong tendency to segregate to the liquid during weld metal solidification. In addition to Nb and Ti, Ta, Hf, Th, and Zr are able to form MC carbides (Davis 2000).

$M_{23}C_6$ carbides are considered the most important type of carbides in Ni-base alloys and they have an FCC (Davis 2000) or complex cubic (Lippold et al. 2009) crystal structure. The $M_{23}C_6$ carbides form on the grain boundaries (Davis 2000) during aging or in the cooling portion of the weld thermal cycle (Lippold et al. 2009) and, when the morphology of the carbides is proper, the formation of the carbides increases the strength of the grain boundaries and restricts grain boundary sliding. Cr is the primary element forming the $M_{23}C_6$ carbides but Ni, Co, Fe, Mo, and W can substitute for the Cr in the formation of $M_{23}C_6$ carbides (Davis 2000). The formation of $M_{23}C_6$ carbides has been found to cause Cr depletion near the grain boundaries in austenitic stainless steels (Peckner and Bernstein 1977, Kekkonen et al. 1985) and in Ni-base alloys (Thomas et al. 2009).

### 2.1.3 DMW fusion boundary and NIZ

Depending on the weld metal, the grain structure near the fusion boundary is dominated by either epitaxial growth or by nucleation of new grains. Epitaxial growth generally takes place in the interfaces where the joined metals have the same crystal structure, i.e. similar metal welds.
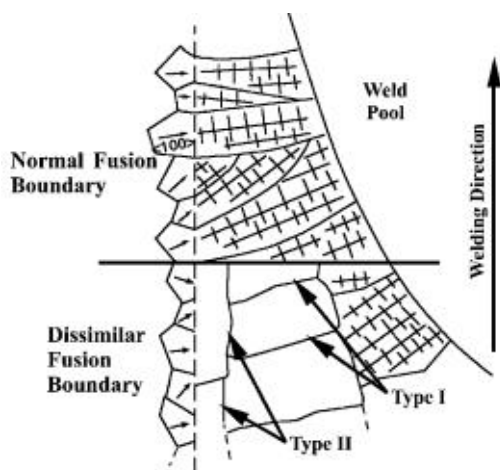


**Figure 2.6.** The formation of the Type II boundary when austenitic weld metal solidifies in contact with ferritic base metal (Nelson et al. 2000).

In DMWs, where the joined metals have different crystal structures at the temperatures near the melting point, the grain structure next to the fusion boundary is formed by the nucleation of new grains, more precisely, by heterogeneous nucleation of the FCC grains in the weld metal. The heterogeneous nucleation at the weld pool boundary results in a fusion boundary that exhibits random misorientations between the base metal grains and the weld metal grains (Kou 2003). Figure 2.6 shows a schematic presentation of the difference in the fusion boundary microstructures between a similar metal weld and a DMW near the

solidification temperature. Grain boundaries running approximately perpendicular to the fusion boundary are called Type I boundaries and boundaries running parallel to the fusion boundary are called Type II boundaries.

### 2.1.3.1 Martensitic zone

At the interface of ferritic base metal and austenitic weld metal, dilution of the weld metal by the base metal may result in a formation of a thin martensitic-like layer with high hardness next to the weld fusion boundary (Pan et al. 1990, Rajeev et al. 2001, Peng et al. 2005, Hou et al. 2010A, Hou et al. 2010B, Peng et al. 2011, Choi et al. 2013). The martensitic-like layer may, with higher dilutions, be followed by a formation of a soft layer in the weld metal, which has been associated with high dilution and significant chromium and nickel depletion (Rajeev et al. 2001). In a case of a dissimilar weld interface between A508III and Inconel 82, the crystal structure of the martensitic-like layer has been proved to consist of lenticular martensite with a Kurdjumov-Sachs (K-S) orientation relationship between the martensitic-like layer and the weld metal (Chen and Lu 2015). The presence of the K-S orientation relationship between the martensitic layer and the weld metal indicates the shear formation of the FCC weld metal (Kurdjumov and Sachs 1930), thus confirming that the layer consists of martensite. The martensitic layer has been found to occur thinner when using Ni-base filler metal than when using austenitic stainless steel filler metal (Lippold et al. 2009). Figure 2.7 shows a schematic picture showing the martensitic layer in the fusion boundary region of an austenitic-ferritic interface.
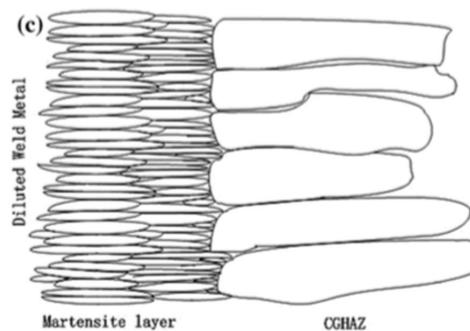


**Figure 2.7.** Schematic picture showing the martensitic layer in the fusion boundary region of an austenitic-ferritic interface (Chen and Lu 2015).

The existence of the martensitic zone has been credited to the change in the hardenability caused by the change in the exact chemical composition across the ferritic-austenitic interface (Laha et al. 2001). Figure 2.8a shows a TEM-EDS line scan across an A508-Inconel 82 interface in which a gradual change in the chemical composition across the martensitic layer-weld metal interface is clearly visible (Chen and Lu 2015). A sharper change in the chemical composition takes place right at the martensite-weld metal interface. The change in the chemical composition across the interface can be estimated to affect the starting temperature of martensite transformation, $M_s$, according to the following equation (Gooch 1977, DuPont and Kusko 2007):

$$M_s(°C) = 540 - (497\%C + 6.3\%Mn + 36.3\%Ni$$

$$+10.8\%Cr + 46.6\%Mo). \qquad (2.1)$$

Accroding to Equation (2.1), the change in the chemical composition causes a change in the $M_s$ temperature across the ferrite-austenite interface. Figure 2.8b shows a change in the $M_s$ temperature across the A508-Inconel 82 interface according to the TEM-EDS line scan in Figure 2.8a (Chen and Lu 2015). In the martensitic layer side, the $M_s$ temperature is decreasing with the chaging composition whilst staying above the room temperature making the martensite transformation possible. At the martensitic layer-weld metal boundary, the $M_s$ temperature drops drastically below the room temperature preventing the martensite transformation from occurring. In a narrow region immediately adjacent to the martensite layer-weld metal boundary in the martensite layer's side, the $M_s$ temperature is below the room temperature indicating that the martensite transformation will not occur only due to the chemical composition. The formation of martensite to this narrow region may be caused by the stresses generated during welding as stress and deformation raise the $M_s$ temperature.
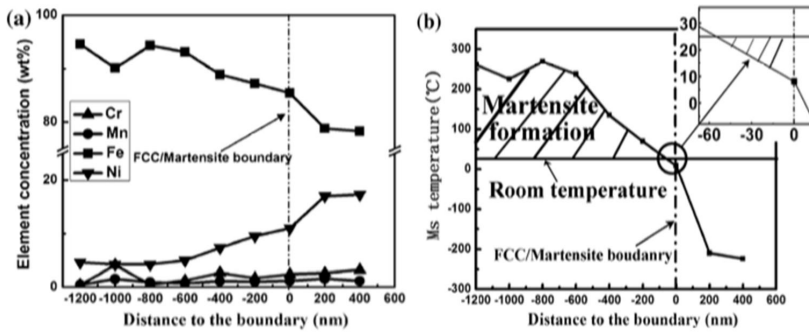


**Figure 2.8.** TEM-EDS line scan across an A508III-Inconel 82 interface (a) and the calculated $M_s$ temperature across the interface (b) (Chen and Lu 2015).

### 2.1.3.2 Type II boundary

A Type II boundary is basically a grain boundary located within a short distance, typically less than 100 μm, from a fusion boundary into a fusion zone of a DMW (Nelson et al. 1999, Lippold et al. 2009). The formation mechanism of Type II boundaries has been found to depend on the solidification behavior of the weld metal and the nature of the solid-state transformation in the base metal. The occurrence of the allotropic δ-γ transformation at elevated temperature is assumed to be necessary in the formation of a Type II boundary (Nelson et al. 2000). In those base metals that undergo a δ-γ transformation, the fusion boundary becomes a γ-FCC grain boundary with a various misorientation between the base and the weld metals within the austenitic temperature range. As both the base and the weld metals are austenite of similar lattice parameters, this boundary is mobile by short range diffusion across the grain boundary interface. Within the austenite temperature range, the γ-FCC fusion boundary migrates into the weld metal as a result of a strong driving force. The driving forces

promoting this migration include steep temperature and composition gradients, strain energy produced by differences in lattice parameter and coefficient of thermal expansion, and non-equilibrium cooling accosiated with welding (Nelson et al. 2000). Figure 2.9 shows a schematic representation of the formation mechanism of the Type II boundaries formed as a result of welding of a DMW between ferritic base metal and austenitic weld metal.



**Figure 2.9.** Mechanism for the formation of Type II boundaries during welding of a DMW between an austentic weld metal and carbon/low alloy steel (Nelson et al. 2000).

### 2.1.3.3 Formation of hard and soft zones at the fusion interface

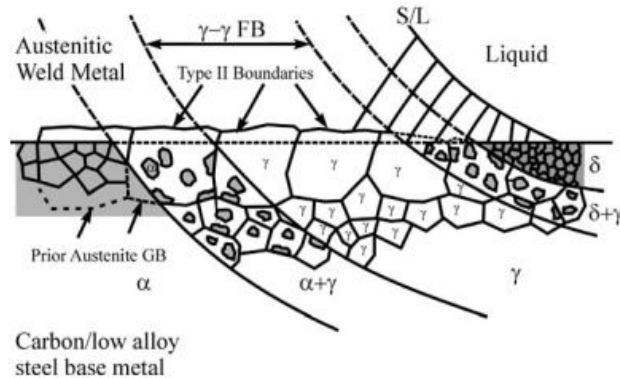During a welding process, the peak temperatures in the HAZ of a weld rise above the $A_{c1}$ temperature causing the ferrite to austenite phase transformation next to the fusion boundary. Within an immediate adjancency of the fusion boundary the peak temperature rises well above the $A_{c1}$ and $A_{c3}$ temperatures resulting in full austenitization and grain coarsening in the HAZ. The following rapid cooling from these temperatures may result in a formation of martensitic and bainitic microstructures in the HAZ next to the fusion boundary, thus, introducing a locally harder microstructural zones at the immediate adjancy of the fusion boundary and further inducing an increased mechanical mismatch at the interface.

DMWs between low alloy steels and austenitic stainless steels with differing Cr contets often contain a softer carbon-depleted zone (CDZ) in the low Cr alloy and higher concentration of carbide precipitates in high Cr side of the interface. The CDZ in the LAS and the precipitate-rich zone in the austenitic weld metal are typically formed as a result of welding process (Lippold et al. 2009) or PWHT (Sudha et al. 2002). The existence of the CDZ and the precipitate-rich zone may lead to higher mechanical mismatch at the interface, which may affect the failure behaviour of the DMW (Rajeev et al. 2001, Lippold et al. 2009). Correspondingly, carbon migration in a dissimilar metal joint between LAS and Ni-base weld metal results in a formation of a CDZ in the HAZ of LAS and a precipitate-rich zone in the Ni-base weld metal adjacent to the interface. The formation of the precipitate-rich zone is due to the lower diffusion of carbon in the Ni-base alloy (Chung et al. 2011). The most significant factors in the migration of carbon across a weld interface and the resulting formation of the CDZ and the

precipitate-rich zone are the Cr content of the joined metals as well as the temperature and the time of the exposure at elevated temperature (Celik and Alsaran 1999, Sudha et al. 2002).

*2.1.3.4 Carbon migration at the fusion interface*

The formation of the CDZ and the precipitate-rich zone are a result of the carbon migrating from the lower Cr-containing side of the fusion boundary to the higher Cr-containing side of the fusion boundary. The driving force for the diffusion of carbon across the interface is the difference in carbon activity caused by the difference in Cr contents in each side of the fusion boundary. The activity of carbon in the lower Cr-containing side is higher than the higher Cr-containing side according to the following equation

$$a_C = N_C \left( e^{N_A \varepsilon_C^A + N_B \varepsilon_C^B} \right), \tag{2.2}$$

where $a_C$ is the activity of carbon, $N_A$, $N_B$, and $N_C$ are the numbers of constituent A and B atoms and carbon atoms present in the alloy, and $\varepsilon_C^A$ and $\varepsilon_C^B$ are the Wagner interaction parameters in ferrite. $\varepsilon_C^{Cr}$ is negative for Cr resulting in the activity of carbon being greater on lower Cr-containing side than the higher Cr-containing side of the interface (Sudha et al. 2002). Thus, carbides dissolve into the solution, carbon in the solution migrates towards the higher Cr-containing side of the interface, and the reduced amount of carbon remaining in the solution leads to a formation of a ferritic-bainitic structure to sole ferrite grains in the CDZ (Sudha et al. 2002). In the higher Cr-containing side of the interface, the carbon content is significantly increased up to the point where the solubility limit of carbon into the austenitic matrix is exceeded. This results in a formation of carbides and the precipitate-rich zone with increased hardness in the austenitic weld metal (DuPont and Mizia 2010).

## 2.2 Mechanical properties of Ni-base alloy DMWs

### 2.2.1 Mechanical properties of ferritic-austenitic DMWs

The local, microstructurally different, narrow zones present in ferritic-austenitic DMW interfaces often have varying mechanical properties. The determination of the mechanical properties of each separate microstructural zone requires specimen small enough so that the sampling size of the specimens takes into account each of the different zones present at the interface. In practice, this means that the stress-strain behavior of the different weld zones should be determined using tensile specimens of significantly small size. Tensile testing of the ferritic-austenitic DMW interfaces can be done using small-sized tensile testing specimens, which should provide the same material characteristics as the standard-sized specimens.

A disadvantage of the small-sized specimens is that the small specimen size restricts the sampled area, and while it is required and beneficial in the sense of sampling the desired microstructural zone, it may lead to case-dependent results. In order for the specimens to be representative of the material and the

obtained results to be reliable, the specimen thickness should be more than 4-6 times the grain size of the material (Kim et al. 2009). Small-sized tensile testing specimens have been used in several studies concerning mechanical testing of different DMW zones (Nevasmaa et al. 2000, Sireesha et al. 2000, Laukkanen et al. 2007, Jang et al. 2008, Kim et al. 2009, Hou et al. 2010A, Wang et al. 2013B), but there is currently no standard for the dimensions or geometries of these specimens and the employed dimensions vary from study to study.

Nevasmaa et al. (2000) and Laukkanen et al. (2007) studied the mechanical properties of a DMW manufactured between SA 508 ferritic steel and AISI 304 austenitic stainless steel using Ni-rich AISI 309L as buttering layer metal and AISI 308L as weld metal with 1.0x2.0 mm flat-bar specimens as well as ∅2.0-5.0 mm round bar specimens. Figure 2.10 shows the yield strength mismatch profiles across the DMW acquired using different specimen geometries. They found the highest strength values from the coarse-grained heat-affected zone (CGHAZ), which showed the strength values of nearly 2 times those of the buttering layer and the weld metal, and the lowest elongation values also from the CGHAZ, which showed the elongation values of 0.2-0.25 to those of the buttering layer and the weld metal. Thus, a substantial mismatch in strength and ductility was observed across the DMW.
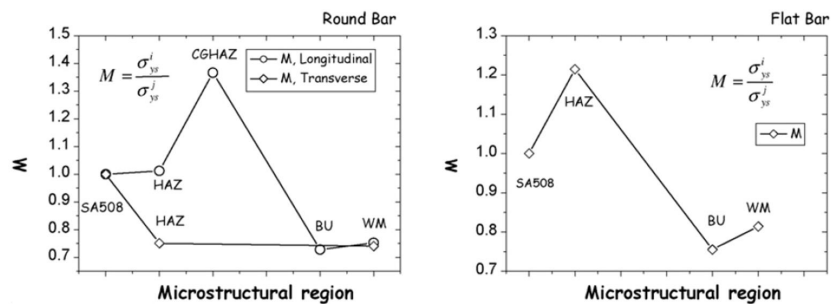


**Figure 2.10.** Yield strength mismatch across the DMW studied by Laukkanen et al. (2007).

Jang et al. (2008) studied the mechanical properties of an Alloy 82/182 DMW manufactured between SA508 Cl.3 ferritic steel and F316 stainless steel using ∅4 mm round-bar tensile testing specimens, 0.28x1.2 mm flat bar tensile testing specimens, and with microhardness measurements. They found the yield strength and the ultimate tensile strength to be higher at the bottom of the weld than at the top of the weld and similar differences were also observed in microhardness tests. They also observed an increase in hardness in a narrow HAZ in the SA 508 Cl.3, which they missed with the tensile tests. That is due to the HAZ being less than the width of the mini-sized specimen and, thus, the HAZ may have been completely or partially missed by the too large sampling size of a tensile testing specimen.

Kim et al. (2009) examined the distribution of tensile properties in a DMW between SA508 Gr.1a and F316 SS with Alloy 82/182 filler metal using 0.5x2.0 mm flat bar specimens at a room temperature and at 320 °C. They found the small-sized flat bar specimens to provide reliable local tensile properties for the different microstructural zones in the DMW. The yield strength of the Alloy

82/182 weld metal was overmatched with respect to both base metals, but undermatched with respect to both HAZs, including the HAZ of F316 SS. The undermatch was found most significant at the interface between the buttering layer and the HAZ of SA508 Gr.1a at 320 °C. At both test temperatures, the minimum ductility in the DMW was found to occur in the HAZ of SA508 Gr.1a. Significant gradients in the yield strength and ultimate tensile strength were observed within the HAZ of SA508 Gr.1a, as shown in Figure 2.11, which shows the changes in yield strength and ultimate tensile strength across the DMW. The gradients were attributed to the different microstructures within the HAZ resulting from the phase transformation during welding.
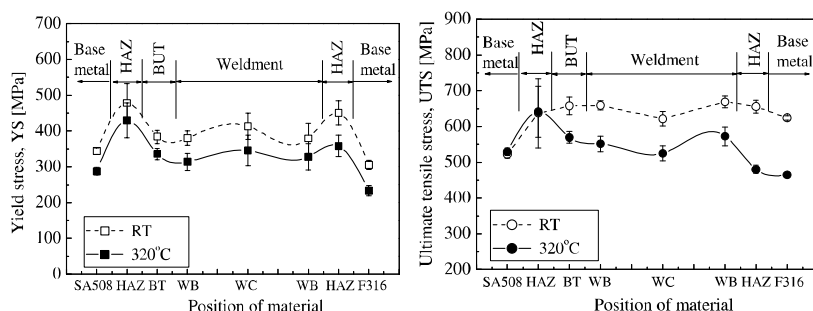


**Figure 2.11.** Changes in yield strength and ultimate tensile strength across a SA508-Alloy82/182-F316 weld (Kim et al. 2009).

Hou et al. (2010A) investigated mechanical properties of a DMW between Alloy 182 and A533 LAS with microhardness measurements and tensile tests using small-sized, ⌀1.5 mm, round bar specimens and normal-sized round bar specimens according to the Japanese Industrial Standard (JIS). They found the yield strength in the HAZ to be higher than that of the dilution zone (DZ), weld metal and base metal, which was somewhat compatible with the microhardness profile across the fusion boundary of the DMW. The hardness in the DZ immediately adjacent to the fusion boundary was much higher than the hardness of the HAZ or the other locations of DZ, as can be seen in Figure 2.12. The location showing the highest hardness was found to be in a narrow zone in the Alloy 182 weld metal between the Type-II boundary and the fusion boundary. The similar kind high hardness zone located between a Type II boundary and a fusion boundary was also found by Peng et al. (2011).
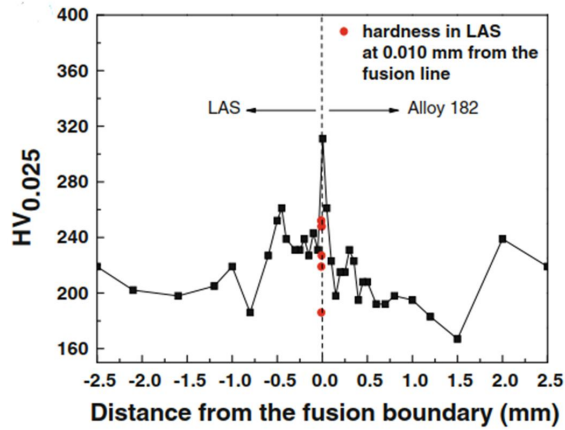
**Figure 2.12.** The microhardness profile across the DMW fusion boundary region by Hou et al. (2010).

Figure 2.13 shows the yield strength of the LAS base metal, Alloy 182 weld metal, the DZ, and the HAZ measured by Hou et al. (2010A). The highest hardness values observed adjacent to the fusion boundary in the DZ do not cause an increase in the measured yield strength of the DZ. According to Hou et al. (2010A), this indicates that the small-sized specimens are still too large, and thus insufficient to characterize the localized hardening adjacent to the fusion boundary. The strengths of the base and the weld metals from the small-sized and JIS specimens showed little difference, indicating that the small-sized specimens are reliable for measuring the mechanical properties of the DMW zones.
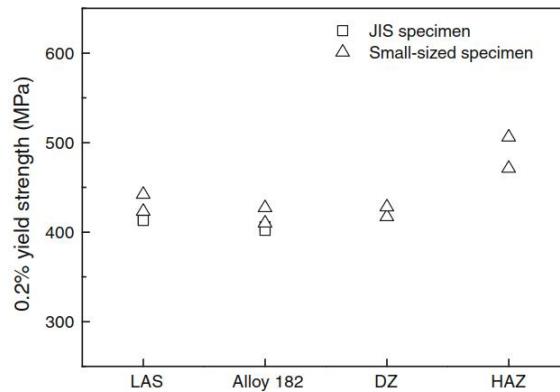


**Figure 2.13.** The yield strengths obtained from the different areas of the DMW by Hou et al. (2010).

Wang et al. (2013B) studied the local mechanical properties of an Alloy 52M DMW between SA508 ferritic steel and 316L stainless steel using 0.5x2.5mm flat bar tensile specimens and microhardness measurement. They found heterogeneous mechanical properties present in the DMW, especially in the three interface regions of SA508-Alloy 52M buttering, Alloy 52M buttering-Alloy 52M

weld metal, and Alloy 52M weld metal-316L. They concluded that the heterogeneous mechanical properties were mainly related to the different, local microstructural zones present at various locations in the DMW. Figure 2.14 shows a microhardness profile and Figure 2.15 shows variations in yield strength, ultimate tensile strength, and fracture strain across the DMW measured by Wang et al. (2013B). In the SA 508 HAZ near the interface, there existed about a 1.5 mm wide zone with maximum hardness and maximum strength. This hardening zone resulted from the presence of lath martensite in the microstructure of the SA 508 HAZ.
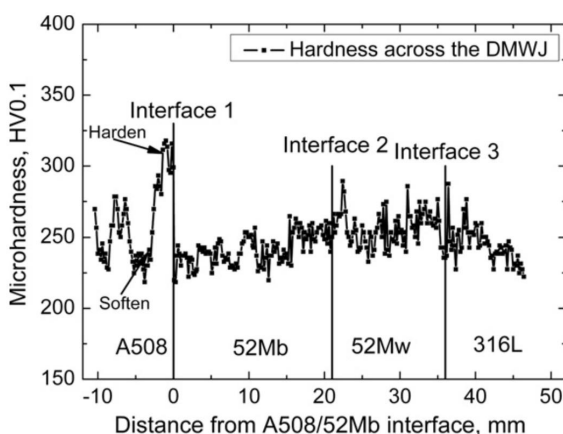


**Figure 2.14.** Microhardness profile across the DMW studied by Wang et al. (2013B).
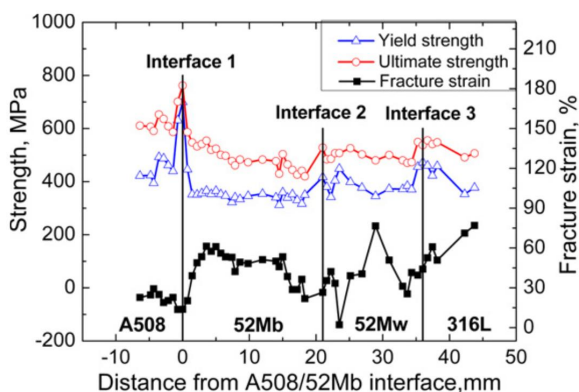


**Figure 2.15.** Variations in yield strength, ultimate tensile strength, and fracture strain along the DMW by Wang et al. (2013B).

Most of the used miniature specimen geometries and dimensions have turned out to provide reliable results, while some results have been seen as case-dependent. According to previous studies, the smallest round-bar specimens with diameters of 1.5 mm and 2.0 mm have been found to be unreliable in the determination of the local mechanical properties. The thinnest flat bar specimens have been found to underestimate the tensile test results of the weld metal. Flat bar specimens with a thickness of 0.5 and 1.0 mm have been found to provide reliable results and hence proven appropriate to determine the mechanical

properties of the local microstructural zones of a DMW and further to characterize the strength mismatch states in DMWs.

In general, mechanically weak points in austenitic-ferritic DMWs are often the microstructures formed near the fusion boundary region, for example in the UMZ and PMZ, due to the chemical composition gradients present in these zones. The CGHAZ has also been found a critical region in terms of the mechanical performance of the DMWs. The local increase of strength and hardness and the subsequent degradation of toughness in weld joints is attributed to the formation of often upper-bainitic CGHAZ microstructure, as well as a narrow martensitic zone, CDZ, and precipitate-rich zone in the austenitic weld metal, which all form as a result of carbon diffusion from the ferritic LAS to the austenitic weld metal (Celik and Alsaran 1999, Nevasmaa et al. 2000, Sireesha et al. 2000, Laukkanen et al. 2007, Jang et al. 2008, Kim et al. 2009, Hou et al. 2010A, Wang et al. 2013B).

### 2.2.2 Mechanical mismatch in ferritic-austenitic DMWs

In the existing structural integrity assessment procedures, such as R6 (R6 2007), the Brite Euram structural integrity assessment procedure for European industry (SINTAP) (SINTAP 1999), and European Fitness-for-service Network's fitness for service procedure (FITNET FFS) (FITNET FFS - MK8 2008), weld joints are simplified to consist only of base metal and weld metal with the microstructural and mechanical properties of the interface region and the HAZ being ignored. The traditional concept of mechanical mismatch in welds in terms of structural integrity assessment focuses on the different strength levels of the weld metal and the base metal in a form of strength mismatch factor M, defined in the SINTAP as the ratio of the yield strength of the weld metal $\sigma_{WM}$ to that of the base material $\sigma_{BM}$ (Kim et al. 2000A).

If an initial crack is located at the interface region or at the HAZ and only the mechanical properties of base metal and the weld metal are used in an integrity assessment, the results of the assessment are potentially either non-conservative or excessive conservative (Wang et al. 2013B). This is due to the large variations in mechanical properties along the DMW. The local mechanical properties in the interface regions and HAZ are often very different from those of the base metals and the weld metal. When the initial crack is located in the interface region or HAZ, the crack-tip plastic deformation and further crack propagation may occur and the crack growth path may change from one zone to the other across the DMW interface (R6 2007, Samal et al. 2009). In these cases, the crack-tip fracture parameters and plastic deformation behavior of the structure are difficult to define due to complex local mechanical mismatch effect in the DMW (Wang et al. 2013B).

The mismatches in local mechanical properties in the different microstructural zones of a DMW have significant effects also on local fracture resistance and crack growth path. If the mechanical mismatch situation is considered from the fracture mechanical point of view, overmatching the weld metal has traditionally been used as a way to secure the weld metal against plastic strains and existing flaws (Moran and Shih 1998). As a result of overmatching the defects

and cracks within the weld metal will less likely develop into fractures since overmatching the weld improves the tensile properties and the stress-strain behavior of the weld metal with respect to the base metal.

In ferritic-austenitic DMWs, the interface regions have been found to have generally higher strength than the surrounding base and weld metals (Wang et al. 2013B). The plastic deformation in materials with higher strength ahead of the crack tip is difficult and, thus higher crack tip opening stress will be induced. That, in turn, may promote the initiation and propagation of brittle fracture (Wang and Wang 2007). With increasing load, the crack tip plastic deformation will mainly develop towards and in the lower strength material or microstructural zone, and higher stress triaxiality will be produced in the material or microstructural zone with lower strength. The higher stress triaxiality can promote the ductile void nucleation, growth, and coalescence, and may thus lead to lower fracture resistance and crack path deviation towards the lower strength material or microstructural zone (Wang et al. 2011, Wang et al. 2013C).

## 2.3 Fracture mechanical properties of Ni-base DMWs

Linear-elastic fracture mechanics (LEFM) can be considered valid as long as nonlinear material deformation is limited only to a small region surrounding the crack tip. This is often not the case with more ductile materials and, thus, an alternative fracture mechanics model is required to describe the fracture mechanical behavior of the material. Elastic-plastic fracture mechanics (EPFM) applies to materials exhibiting larger amounts of crack tip plasticity. The two common EPFM parameters are the crack-tip-opening displacement (CTOD) and the J contour integral. In principle, both parameters describe the crack tip conditions in elastic-plastic materials and each can be used as a fracture criterion. There are applicability limits also to the EPFM parameters J and CTOD, but these limits are much less restrictive than the validity requirements of the LEFM (Anderson 2005, Wallin 2011).
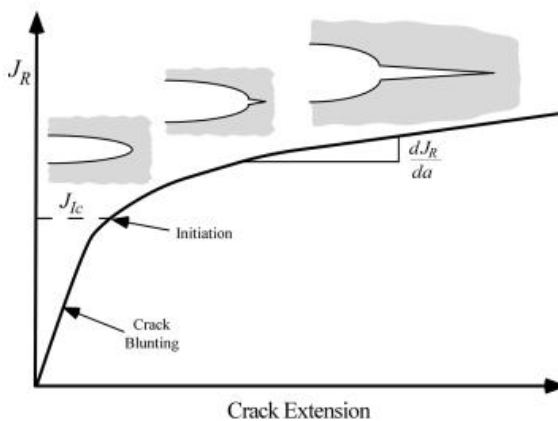


**Figure 2.16.** Schematic fracture resistance curve of ductile material (Anderson 2005).

High toughness materials are not typically susceptible to a catastrophic failure at a particular J or CTOD value but rather display a rising fracture resistance curve where J or CTOD increases simultaneously with crack growth. In metals, the rising resistance curve is usually associated with the growth and coalescemce of microvoids. Figure 2.16 shows a schematic of a typical fracture resistance curve of ductile material. In the early stages of deformation, the slope of the resistance curve is very high, which means that there is only a very small amount of apparent crack growth which is due to blunting of the crack tip. When the J increases, the material at the immediate crack tip fails locally and the crack is able to advance further. Perhaps the most used individual measure of fracture toughness determined from the fracture resistance curve is $J_{Ic}$, which is the J value defined near the initiation of stable crack growth. The precise point at which the stable crack growth begins is, however, often quite hard to define, which makes the definition of $J_{Ic}$ a bit arbitrary (Anderson 2005).

The initial crack growth is usually stable, which shows as a rising J curve. However, an instability in crack growth can encounter later in some instances (Anderson 2005). While the initiation toughness provides some information, the entire fracture resistance curve gives a more complete description of the fracture behavior of a ductile material. The slope of the fracture resistance curve at a given amont of crack extension indicates the relative stability of the crack growth. Material with a steep fracture resistance curve is less likely to experience unstable crack propagation and vice versa.

### 2.3.1 Fracture mechanics of ferritic-austenitic DMWs

The varying metallurgical and mechanical properties across a ferritic-austenitic DMW cause the different microstructural zones of the DMW to have varying fracture mechanical properties. Laukkanen et al. (2007) studied the fracture mechanical properties of a DMW manufactured from AISI 309L buttering layer and AISI 308L weld metal between SA 508 ferritic steel and AISI 304 austenitic stainless steel using Charpy-size 10x10x55 mm three-point bend (3PB) specimens for different microstructural regions and base and weld metals. They found the fracture resistance to be the lowest near the fusion boundary; the fracture resistance curves acquired by Laukkanen et al. (2007) are shown in Figure 2.17. In addition, they observed cases involving unstable crack propagation after ductile initiation. They attributed the decreased fracture resistance near the fusion boundary regions to low-toughness ductile rupture mechanism occurring near the fusion boundary at the buttering layer side and at the fusion boundary.
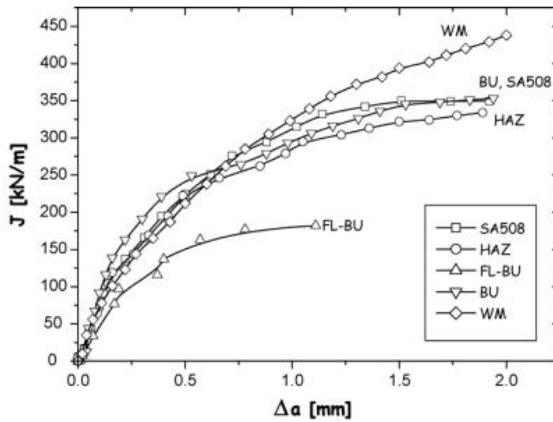
**Figure 2.17.** Fracture resistance curves of the SA 508-AISI 309L/308L-AISI 304 DMW regions by Laukkanen et al. (2007).

Wang et al. (2011) examined an Alloy 82/182 DMW between SA 508 ferritic steel and AISI 316L stainless steel and Wang et al. (2013A) and Wang et al. (2013C) studied an Alloy 52M DMW between A508 ferritic steel and 316L stainless steel. Figures 2.18 and 2.19 show the fracture resistance curves from their studies, respectively.
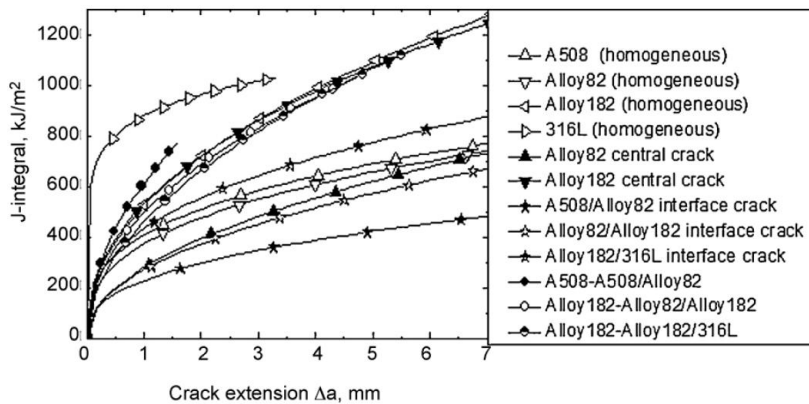


**Figure 2.18.** Fracture resistance curves of the SA 508-Alloy 82/182-AISI 316L DMW regions by Wang et al. (2011).
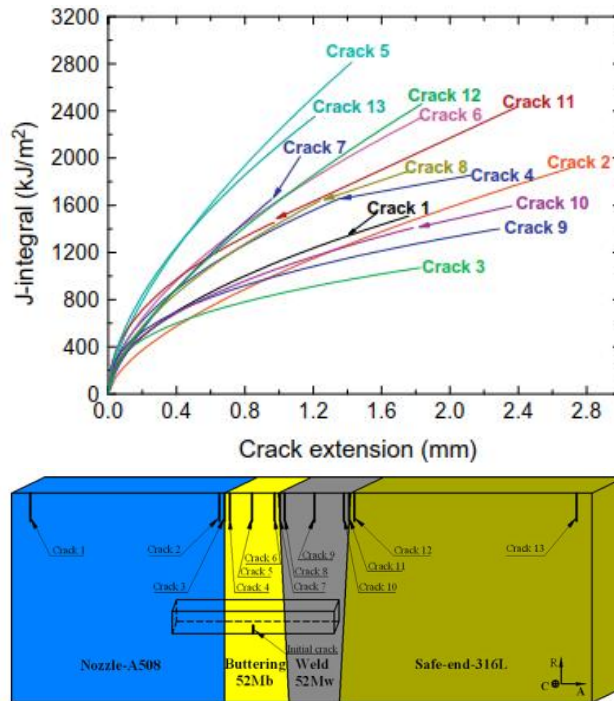
**Figure 2.19.** Fracture resistance curves and initial crack locations of the SA 508-Alloy 52-316L DMW regions by Wang et al. (2013A).

Both studies showed the lowest fracture resistance curve, and hence, the fracture mechanically weakest zone in the DMW to be near the interface region between the A508 and Alloy 82/182/Alloy 52M. A mixed brittle and ductile fracture mechanism dominated by the brittle mechanism was found to be the fracture mechanism in the A508-Alloy 52M interface. The existence of the dominantly brittle fracture mechanism and, thus, the lowest fracture resistance, was attributed to the existing strength mismatch and predominantly martensitic microstructure near the interface region. The cracks in the interface region and HAZ were found to generally grow towards the material with lower strength and the crack path deviation was attributed to local strength mismatch, which had an effect on the measured fracture resistance.

Overall, within the different DMW regions, the fusion boundary and the NIZ have been found to exhibit the lowest fracture toughness in terms of initiation of a stable crack growth and tearing resistance (Nevasmaa et al. 2000, Laukkanen et al. 2001, Faidy et al. 2004, Laukkanen et al. 2007). The lowest fracture resistance within the different zones of a DMW has reportedly also been found from the buttering layer and the interface of the buttering layer and the weld metal (Schwalbe et al. 2004, Samal et al. 2011).

### 2.3.2 Crack growth in ferritic-austenitic DMW interfaces

The crack growth mechanisms and directions in DMWs have been studied quite widely in the past decades (Hutchinson et al. 1987, Homma et al. 1995, Lin et al.

1999, Nevasmaa et al. 2000, Jiang et al. 2003, Neves and Loureiro 2004, Schwalbe et al. 2004, Laukkanen et al. 2007, Wang et al. 2011, Wang et al. 2013A, Wang et al. 2013C, Yang et al. 2014A, Yang et al. 2014B) and found to depend on the mismatch in mechanical properties, the position of the different zones in relation to each other, the dimensions of the zones, and the local strength and toughness properties of the adjacent weld zones. Crack growth behavior differs significantly between materials with low heterogeneity, such as bulk materials and welds where the base metal, the HAZ, and the weld metal possess similar mechanical properties, and materials with high heterogeneity, such as DMWs (Homma et al. 1995).

In materials with low heterogeneity, the crack growth resistance is dominated by the properties of the material in which the crack tip is located. In materials with high heterogeneity, in contrast, the crack growth resistance is affected also by the material other than the one in which the crack tip is located. Mismatch in mechanical properties across a dissimilar metal interface causes different kinds of deformation on the two sides of the crack tip and higher stress triaxiality in the softer metal's side, even if the loading is symmetrical (Jiang et al. 2003). Therefore, a crack may grow along the interface or deviate into the softer metal but the crack does not turn into the harder metal. The resistance to crack growth has been found lower along the dissimilar metal interface than in the respective counterpart metals. The strength mismatch between different materials or microstructural regions produces different local plastic constraints which further affect the local stress triaxiality and plastic strain ahead of the crack tip locating at the interface (Wang et al. 2013C). Irrespective of the existence of the original flaw or defect in a weld, the actual damage formation can therefore occur and escalate in a neighboring microstructure (Nevasmaa et al. 2000, Laukkanen et al. 2007).

The combination of stress triaxiality and asymmetric plastic strain is considered as the principal driving force for damage formation and ductile fracture in DMWs. Thus, the significance of mechanical mismatch can be seen as an increase in constraint and the localized deformation experienced by the softer regions and the resulting compatibility requirements set to the harder microstructures. A notch or a crack-like defect at the interface of two materials of which one exhibits plastic behavior that affects the crack tip plasticity development while the other still behaves practically linear-elastically has been concluded to represent the worst mismatch scenario in terms of structural integrity (Nevasmaa et al. 2000, Laukkanen et al. 2007).

Figure 2.20 shows the size of the plastic zone in front of the crack tip simulated by Xue et al. (2009). This schematically demonstrates the effect of mechanical mismatch on the asymmetric localization of plastic strain at the crack tip. The plastic strain concentrates on the softer side of the crack tip while the harder side withstands higher amount of stress. The concentration of deformation to the softer side eventually results in crack tip deflection towards the more deformed side.
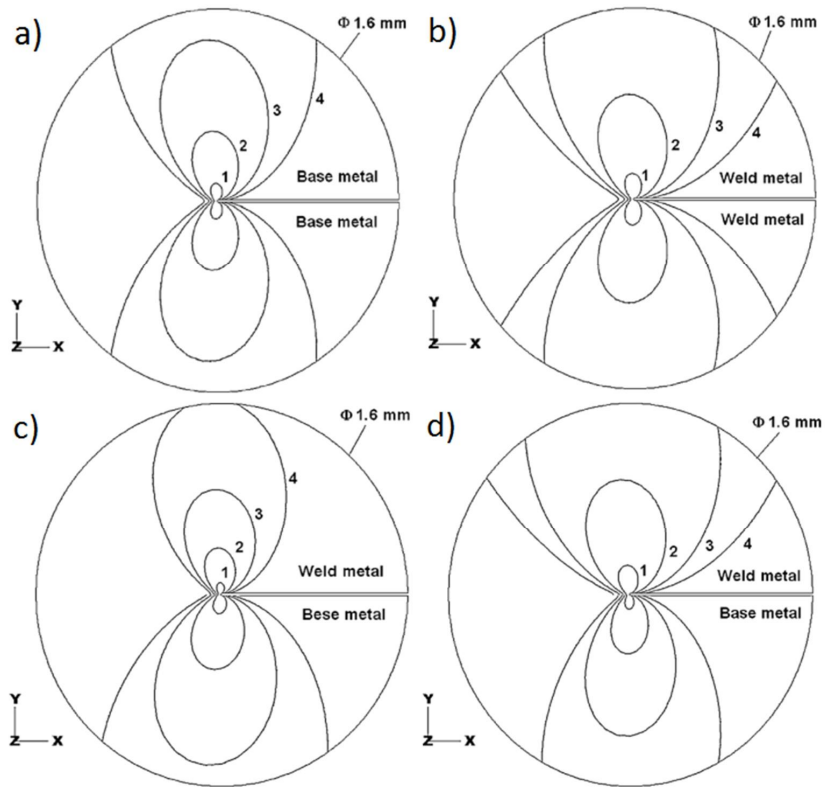
**Figure 2.20.** Simulations of the size of the plastic zone in front of a stationary crack tip with a) the crack in base metal, b) the crack in weld metal, c) the crack in base metal-weld metal interface with the weld metal overmatched, and d) the crack in base metal-weld metal interface with the weld metal undermatched (Xue et al. 2009).

In dissimilar metal interfaces, unstable crack growth has been found to occur after a ductile initiation in the fusion boundary and NIZ of the DMW (Nevasmaa et al. 2000, Laukkanen et al. 2001, Faidy et al. 2004, Laukkanen et al. 2007). A combination of several adjacent microstructures, such as a CDZ in the ferritic HAZ, a weld interface with discontinuous martensitic regions, and a fully austenitic region in the first buttering layer, all with mismatching mechanical properties, has been considered responsible for unstable crack growth occurring in a dissimilar metal interface. Laukkanen et al. (2007) presented two possible low-toughness fracture types for a ferritic-austenitic SA 508-AISI309L/AISI308L dissimilar metal interface: 1) low-toughness ductile fracture and 2) unstable crack growth preceded by ductile initiation, shown in Figures 2.21 and 2.22, respectively.
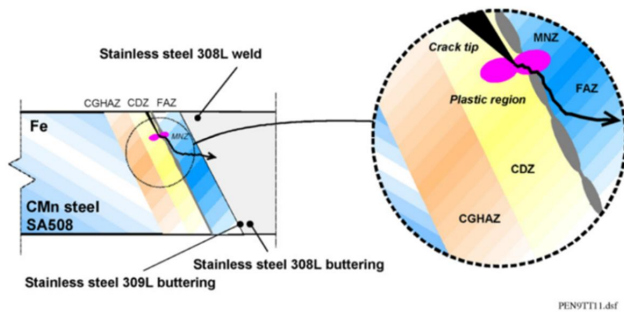
**Figure 2.21.** Crack propagation mechanism associated with low-toughness ductile fracture (Lauk-kanen et al. 2007).

The low-toughness ductile fracture at the fusion boundary was associated with the initial crack locating closer to the fusion boundary than with the unstable crack growth. The tip of the initial crack locating closer to the fusion boundary results in a development of a relatively symmetric plastic region at the crack tip, which is followed by a ductile initiation at the weld interface. This results in a crack deviation through the fully austenitic zone (FAZ) to the buttering/weld metal and further ductile crack growth at the buttering/weld metal by ductile tearing (Laukkanen et al. 2007).

The unstable crack growth, in contrast, was associated with a propagating fracture having initiated in a ductile manner in the ferritic CGHAZ and deviated towards the fusion boundary, which was farther away from the original crack tip. The initial crack tip locating in the CGHAZ results in a development of an asymmetric plastic region at the crack tip towards the adjacent CDZ of lower strength. The asymmetricity of the plastic region is caused by the strength mis-match between the CGHAZ and the CDZ. This is followed by a ductile crack in-itiation in the CGHAZ and crack deviation trough the softened CDZ by quasi-cleavage to the weld interface containing discontinuous martensitic zone (MNZ) and further followed by a cleavage fracture of the MNZ and crack propagation along the interface either by deflecting to the FAZ or to the CDZ (Laukkanen et al. 2007).
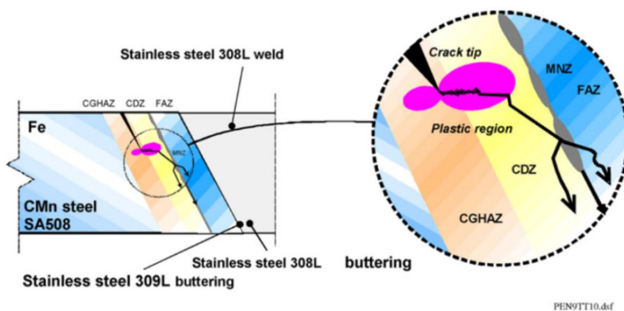


**Figure 2.22.** Crack propagation mechanism associated with unstable rupture of CGHAZ (Lauk-kanen et al. 2007).

According to Laukkanen et al. 2007, if the crack tip is located in the CGHAZ, the asymmetric plasticity gives rise to a generally high level of crack driving force producing an energy supply leading to an unstable failure after the crack deflection to the interface due to its lower ductility. If, on the other hand, the crack is located near or at the fusion boundary and hence closer to the interface, the failure can occur as ductile fracture with a generally lower lever of driving force.

# 3 Experimental procedures

The main objective of this thesis was to determine the microstructure and mechanical properties of a ferritic-austenitic interface of a Ni-base dissimilar metal weld and to assess the effect of the mechanical properties on the fracture mechanical behavior of the ferritic-austenitic interface of the DMW. The research consisted of studies conducted for two different types of weld mock-ups representing the Ni-base safe-end DMWs used in commercial LWR pressure vessel designs.

## 3.1 DMW mock-up specification and manufacturing

The first studied DMW design was a traditional V-groove DMW representing the safe-end weld of a BWR pressure vessel. The BWR-DMW mock-up consisted of SA 508 pressure vessel steel with AISI 309L/308L cladding and AISI 304 piping steel, Alloy 182 buttering layer welded perpendicular to the outer surface of the SA 508 base metal, and Alloy 82 and 182 weld metals. A technical drawing showing the dimensions and materials of the BWR-DMW mock-up is presented in Figure 3.1.
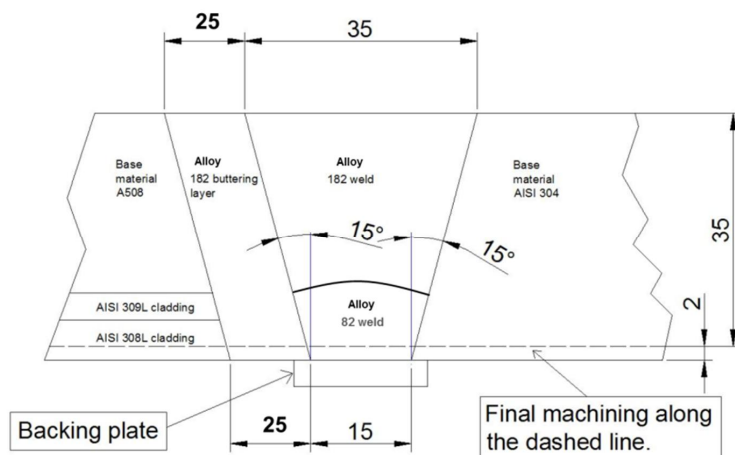


**Figure 3.1.** Technical drawing showing the dimensions and materials of the BWR-DMW mock-up.

The second studied weld was a narrow-gap DMW representing the safe-end weld of a modern PWR design. The NG-DMW mock-up consisted of SA 508

pressure vessel steel with AISI 309L/308L cladding and AISI 304 piping steel with Alloy 52 weld metal. Figure 3.2 presents a technical drawing showing the dimensions and materials of the NG-DMW.
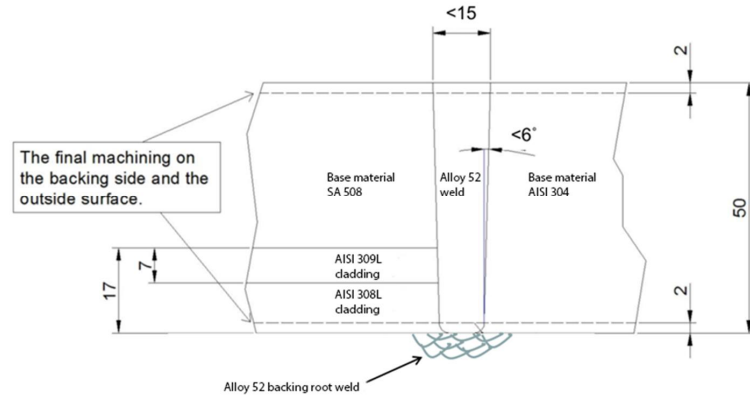


**Figure 3.2.** Technical drawing showing the dimensions and materials of the NG-DMW mock-up.

The DMW mock-ups were manufactured using the alloys used in corresponding components of commercial BWR and PWR designs. The chemical compositions of the different materials used in the manufacturing the weld mock-ups are presented in Table 3.1.

**Table 3.1.** Chemical compositions of the materials used in the DMW mock-ups.

|    | SA 508 | AISI 304 | AISI 308L | AISI 309L | Alloy 82 | Alloy 182 | Alloy 52 |
|----|--------|----------|-----------|-----------|----------|-----------|----------|
| C  | 0.21   | 0.019    | 0.007     | 0.012     | 0.039    | 0.03      | 0.03     |
| Si | 0.17   | 0.4      | 0.37      | 0.33      | 0.03     | 0.7       | 0.13     |
| Mn | 0.78   | 1.77     | 1.9       | 1.8       | 2.98     | 5.9       | 0.24     |
| P  | 0.002  | 0.03     | 0.013     | 0.014     | 0.001    | 0.01      | <0.001   |
| S  | 0.009  | 0.001    | 0.001     | 0.001     | 0.004    | 0.006     | <0.001   |
| Cr | 0.45   | 18.16    | 20.3      | 23.8      | 19.94    | 16        | 29.2     |
| Ni | 0.85   | 8.07     | 10.3      | 13.2      | 72.6     | 69        | 59.28    |
| Mo | 0.62   | 0        | 0.1       | 0.1       | 0        | 0         | 0.03     |
| Nb | 0      | 0        | 0         | 0         | Nb+Ta 2.47 | 1.7     | Nb+Ta  <0.02 |
| N  | 0.014  | 0.05     | 0.04      | 0.06      | 0        | 0         | 0        |
| Ti | 0.002  | 0        | 0         | 0         | 0.34     | 0.1       | 0.51     |
| Fe | 0      | 0        | 0         | 0         | 0.2      | 5.6       | 9.8      |
| Al | 0.016  | 0        | 0         | 0         | 0        | 0         | 0.72     |
| Co | <0.003 | 0        | 0         | 0         | 0.01     | 0         | 0.009    |
| Cu | 0.06   | 0        | 0.05      | 0.05      | 0.01     | < 0.01    | 0.04     |

The weld mock-ups were manufactured using shielded metal arc welding (SMAW) and gas tungsten arc welding (GTAW) methods. In addition, the AISI 309L/308L claddings of the both mock-ups were manufactured using submerged arc welding (SAW) method. The welding details and parameters used in the manufacturing of the DMW mock-ups are thoroughly presented in a "Structural Integrity of Ni-Base Alloy Welds" report by Hänninen et al. (2014).

Before the characterization, both DMW mock-ups were post-weld heat treated to simulate the effect of the residual stress relief post-weld heat treatment performed on an actual welded component. In the case of the BWR-DMW, after the Alloy 182 buttering was welded, a post-weld heat treatment of 1 h at 575 °C with a cooling and heating rate of 30 °C/h was performed. After the manufacturing of the weld was complete, the BWR-DMW specimens were further post-weld heat treated at 605 °C for 6 h. As for the NG-DMW, a two-step post-weld heat treatment was performed to the finished mock-up. The first step consisted of a heat treatmen at 550±15 °C for 17.1 h followed by the second step of 7.4 h at 610±15 °C. The maximum heating and cooling rate of the NG-DMW PWHT was 50 °C/h.

## 3.2 Microstructural characterization

Figures 3.3 and 3.4 show optical macrographs of the manufactured BWR-DMW and NG-DMW mock-ups. The focus of this thesis is on the characterization of the ferritic-austenitic interface which in case of the BWR-DMW is the SA 508-Alloy 182 buttering interface and in the case of the NG-DMW it is the SA 508-Alloy 52 weld metal interface.
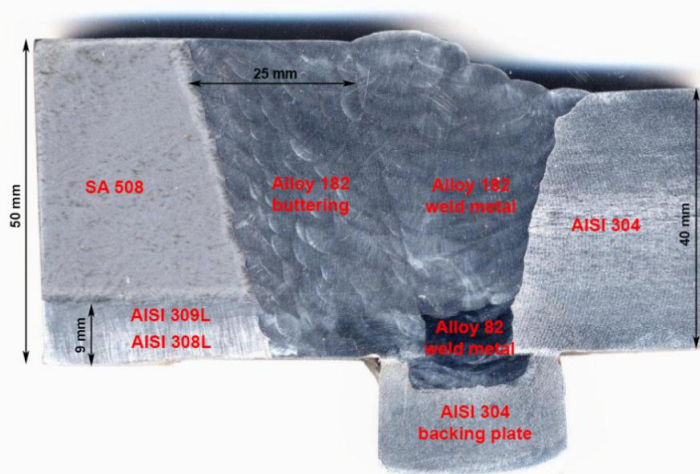


**Figure 3.3.** Cross-section macrograph of the BWR-DMW mock-up.

Microstructural characterization was performed using optical microscopy and SEM with EBSD and EDS measurement techniques to the PWHT condition BWR-DMW and to the NG-DMW in PWHT as well as in as-welded condition. The focus of the microstructural characterization was in the SA 508 HAZs and the ferritic-austenitic interfaces of the studied welds.
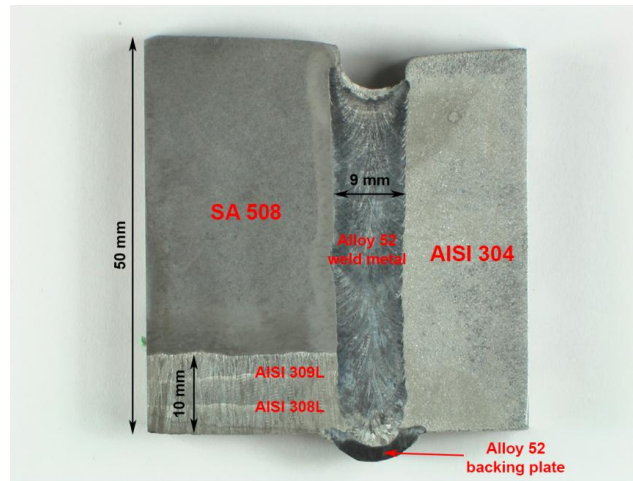
**Figure 3.4.** Cross-section macrograph of the NG-DMW mock-up.

The specimens for the microstructural characterization were extracted from the ferritic-austenitic interfaces of the welds using electrical discharge machining (EDM). After the extraction, the specimens were mounted in a conductive resin, grinded using SiC paper up to 4 000 grit and further polished using diamond suspension with grit sizes of 3, 1, and 0.25 μm. The final polishing of the electron backscatter diffraction (EBSD) specimens was done in a vibratory polisher using colloidal silica suspension. The optical microscopic specimens were etched immersing the specimens either into 2 % Nital solution or Aqua regia depending on whether the studied zone was the SA 508 HAZ or the Alloy 182/52 buttering/weld metal.

### 3.2.1 Optical microscopy

Optical microscopy involves passing visible light transmitted through or reflected from a specimen through a lens system to magnify images of small specimens allowing visual identification of the different microstructural features of a specimen. The optical microscopy in this study was performed using a Nikon Epiphot 200 inverted metallurgical microscope.

### 3.2.2 Scanning electron microscopy

Scanning electron microscopy (SEM) is based on irradiating the area of interest with a finely focused electron beam, which is rastered across the surface of the specimen to form an image of the studied area. The electron beam interacts with the interaction volume of the studied specimen to produce secondary electrons, backscattered electrons, characteristic X-rays, and other photons of various energies, which are further used to examine different characteristics of the studied specimen. A schematic image showing the SEM electron beam-specimen interaction volume and the different types of signals produced as a result of the electron beam-specimen interactions is presented in Figure 3.5. From the imaging

point of view, the important types of signals produced by the electron beam-specimen interactions are the secondary and backscattered electrons.
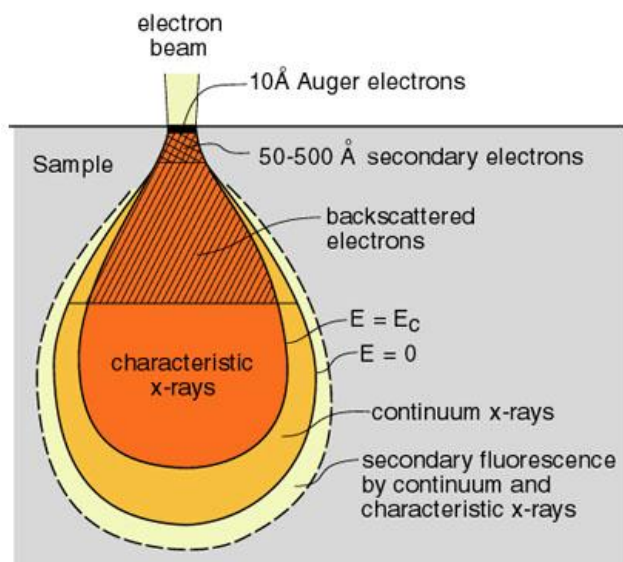


**Figure 3.5.** Schematic picture showing the SEM electron beam-specimen interaction volume (Northern Arizona Univeristy 2016).

One of the key features of an SEM is the electron gun whose purpose is to provide a stable beam of electrons of adjustable energy. A few different types of electron guns are used in commercial SEMs. Generally, older and less expensive SEMs use tungsten or $LaB_6$ thermionic emitters to produce the electron beam and newer and more expensive microscopes are equipped with field emission gun (FEG) with either a cold field emitter (CFE) or Schottky field emitter (SFE). The thermionic emittes rely on the use of high temperatures to enable electrons in the cathode to overcome the work function energy barrier and escape into the vacuum whereas in the case of the field emission emitters, the emitter is held at several kilovolts negative potential relative to a nearby electrode. That provides a sufficient potential gradient at the emitter surface to cause field electron emission.

The advantages of field emission guns in electron microscopes with respect to the conventional guns with thermionic emitters are smaller electron beam diameter, more coherent electron beam with significantly greater current density or brightness. The result is significantly improved signal-to-noise ratio and spatial resolution, and greatly increased emitter life and reliability compared with thermionic devices. The SEM studies in this thesis were performed using Zeiss Ultra 55 and Merlin VP compact field emission scanning electron microscopes (FESEM).

### 3.2.3 Energy dispersive X-ray spectroscopy

Energy dispersive X-ray spectroscopy (EDS) makes use of the characteristic X-ray spectrum emitted as a result of the electron beam-specimen interactions to obtain a localized chemical analysis. The EDS analysis is based on the fundamental principle that each element has a unique atomic structure resulting in a unique set of peaks in its characteristic X-ray emission spectrum.
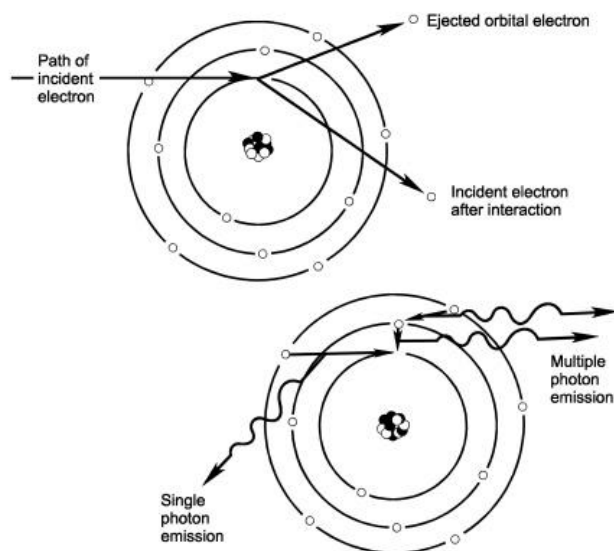


**Figure 3.6.** Schematic picture showing the principle of characteristic X-ray formation (Northern Arizona University 2016).

Atoms within the specimen contain unexcited electrons in discrete energy levels or electron shells bound to their nuclei. The incident electron beam excites electrons in inner electron shells ejecting them from the shells while creating electron vacancies. That results in electrons from outer, higher-energy shells to drop in energy level to fill the vacancies in the lower-energy shells. The difference in energies between the higher-energy shells and the lower-energy shells is released in the form of an X-ray, which is unique to each element, thus allowing the characterization of elements. Schematic presentation showing the principle of characteristic X-ray formation is shown in Figure 3.6. In principle, the EDS can detect all elements from Be (Z =4) to U (Z=92), although not all systems are optimal to detect lighter elements (Z < 10) (Goldstein et al. 2003).

### 3.2.4 Electron backscatter diffraction

EBSD is an SEM based technique to characterize the crystallographic properties of materials. EBSD technique is based on the acquisition and analysis of Kikuchi diffraction patterns acquired from the specimen surface in an SEM. The formation of the Kikuchi patterns is a result of the backscattered electrons diffracting from the specimen's crystal planes in a Bragg's angle to form so called Kossel cones, which are captured by the EBSD detector's phosphor screen to form

Kikuchi bands. A schematic image showing the principle of the pattern acquisition in EBSD is shown in Figure 3.7.
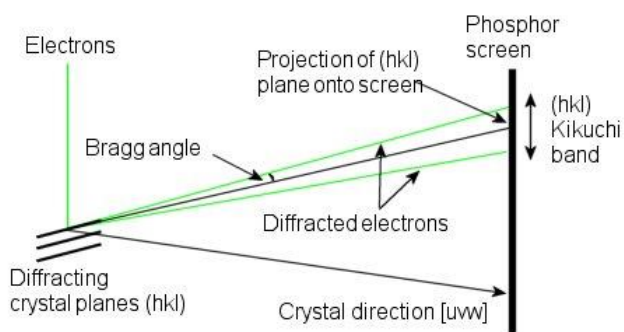


**Figure 3.7.** Schematic picture showing the principle of EBSD acquisition (Oxford Instruments 2016).

The Kikuchi diffraction pattern consists of a set of Kikuchi bands, which are characteristic of the crystal structure and orientation of the studied specimen. The centerlines of the Kikuchi bands correspond to the projection of the diffracting planes on the phosphor screen and can then be indexed by the Miller indices of the diffracting crystal plane, which formed it. The Kikuchi band positions are found using the Hough transform, which is a transform between the coordinates (x, y) of the diffraction pattern and the coordinates ($\rho$, $\theta$) of Hough space. The crystallographic properties, i.e., orientation and structure can then be determined by comparing the acquired Kikuchi diffraction patterns to simulated Kikuchi diffraction patterns formed by a known crystal structure and orientation.

In this study, the EBSD technique was used to analyse the crystallographic characteristics of the ferritic-austenitic interafaces and SA 508 HAZs of the studied DMWs. The EBSD characterization was performed using HKL Nordlys EBSD detector and post-processing of the acquired EBSD data was done using Channel 5 post-processing software. Figure 3.8 shows the inverse pole figure (IPF) key describing the color-orientation relationship for the IPF-maps shown in the results section.
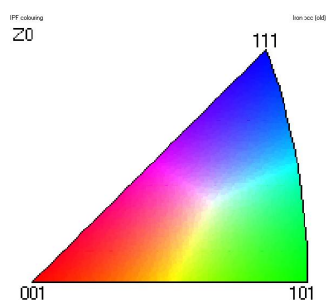


**Figure 3.8.** IPF key for the IPF maps shown in the results section.

## 3.3 Hardness testing

Hardness is a material property representing material's resistance to localized plastic deformation. Quantitative hardness measurement techniques are based on an indenter being forced into a surface of material under controlled load and loading rate. The geometric properties of the resulting indentation are measured and related to a hardness number. Softer material results in larger and deeper indentation and lower hardness number. Hardness tests are commonly divided into hardness testing, microhardness testing, and nanoindentation testing based on the indentation load and volume of material tested.

### 3.3.1 Vickers hardness testing

Figure 3.9 shows the principle of the Vickers hardness test. A diamond indenter with a square based pyramid head is forced into the surface of a test piece and the diagonal lengths of the resulting indentation are measured after the removal of the test force. The resulting Vickers hardness value is then obtained by dividing the test force by the sloping area of the indentation according to the following equation (ISO 6507-1:2005):

$$HV = Constant \times \frac{F}{A} = 0.102 \frac{2F sin\frac{136°}{2}}{d^2} \approx 0.1891 \frac{F}{d^2}, \qquad (3.1)$$

where F = test force, A = area of the indentation, d = arithmetic mean of the two diagonals $d_1$ and $d_2$, and the constant = 0.102 ≈ 1/9.80665 where 9.80665 is the conversion factor from kgf to N.
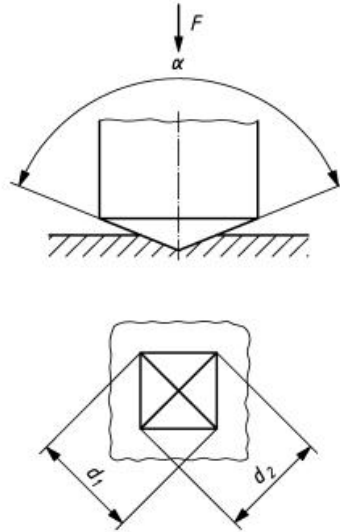


**Figure 3.9.** Schematic showing the principle of the Vickers hardness test (ISO 6507-1:2005).

The Vickers indenter produces a geometrically similar indentation over a very wide range of test loads and thereby the HV value is constant, within statistical

precision, over a very wide test load range as long as the test specimen is reasonably homogeneous (ASTM E384 – 11e1). However, numerous studies of microindentation hardness test results conducted over a wide range of test loads show that test results usually differ at loads below 100 gf (Vander Voort 1984, Vander Voort 1989A, Vander Voort 1989B). The distance between two adjacent indentations has to be sufficient to avoid the effect of strain hardnening resulting from the former indentation to the latter indentation. For harder materials, it is considered that the distance of three times the indentation diameter (ISO 6507-1:2005) is sufficient enough so that the strain hardening of the first indentation does no affect the measurement of the second indentation.

In this study, the Vickers hardness measurements were performed to ferritic-austenitic interfaces of both welds, BWR-DMW and NG-DMW. The hardness profiles were determined using a Buehler Micromet 2104 hardness measurement system equipped with a Vickers tip using an indentation load of 300 gf with a step size of 0.1 mm between the indentations.

### 3.3.2 Nanoindentation testing

Modern indentation techniques and instruments, which make the continuous measurement of force and displacement during indentation testing possible, allow the determination of mechanical properties directly from the indentation load and displacement data without the need to separately image and measure the indentation marks (Oliver and Pharr 1992, Oliver and Pharr 2004). This allows indentation measurements at very low indentation loads where the indentation area is difficult to be conveniently measured due the resolution limitations of optical microscopy. The indentation analysis presented in the following and performed in the nanoindentation measurements presented in this thesis is made according to the Oliver and Pharr method developed and published by Oliver and Pharr in 1992.
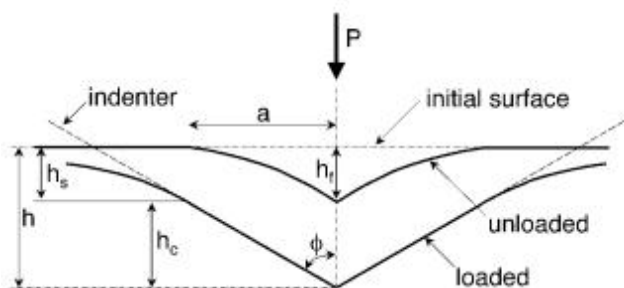


**Figure 3.10.** A schematic presentation of a section through an indentation showing various parameters used in an indentation analysis (Oliver and Pharr 1992).

Figure 3.10 shows a cross-section of an indentation with parameters used in an indentation analysis. The total displacement, h, caused by the load, P, can at any time during the loading be expressed as a sum of the vertical distance along which contact is made, $h_c$, and the displacement of the surface at the perimeter of the contact, $h_s$. During the maximum load, $P_{max}$, the maximum displacement

is $h_{max}$ and the radius of the contact area is a. During unloading, the elastic displacements are recovered resulting in the final depth of the residual hardness impression, $h_f$, after the indenter is fully withdrawn.

Simultaneously with the loading and unloading stages, the load and the displacement of the indenter are recorded to form a load-displacement curve. A schematic representation of a load-displacement data with the experimental parameters needed to determine hardness and elastic modulus are shown in Figure 3.11. The three key parameters are the maximum load, $P_{max}$, the depth at the maximum load, $h_{max}$, and the initial unloading contact stiffness, $S_{max}$ (Oliver and Pharr 1992).
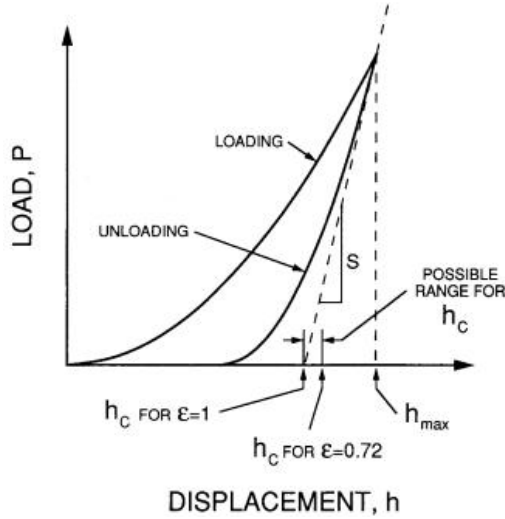


**Figure 3.11.** A schematic representation showing the load versus indenter displacement data for an indentation experiment (Oliver and Pharr 1992).

The Oliver and Pharr method is based on a concept of the material conforming to the shape of the indenter to some depth at a maximum load. If this depth can be established from the load displacement data, the projected area of the contact can be estimated directly from the indenter shape function according to the equation

$$A = F(h_c), \tag{3.2}$$

where A is the projected area of the indentation and $h_c$ is the contact depth. The function F has to be determined experimentally for the used indenter tip prior to the analysis. According to the Oliver and Pharr method, the unloading portion of the load displacement data can best be described with a power law relation

$$P = \alpha(h - h_f)^m, \tag{3.3}$$

where $\alpha$, m, and $h_f$ are constants determined by a least squares fitting procedure. The initial unloading slope S can be found by analytically differentiating

the power law relation and evaluating the derivative at the maximum load and displacement. Since

$$h_c = h_{max} - h_s,$$ (3.4)

and $h_{max}$ can be experimentally measured, the key thing for the analysis is to solve the displacement of the surface at the contact perimeter, $h_s$. This can be derived using the following equation

$$h_s = \epsilon \frac{P_{max}}{S},$$ (3.5)

where $\epsilon$ is a geometric constant, which is 0.72 for conical indenter, 0.75 for paraboloid of revolution, and 1 for the flat punch. Solving the $h_s$ allows the solving of $h_c$ and further deriving the projected area of indentation, A. By using the contact stiffness, S, and the projected area of indentation, A, the reduced modulus $E_r$, can be derived by using the following equation.

$$E_r = \frac{\sqrt{\pi}}{2} \frac{S}{\sqrt{A}}.$$ (3.6)

The reduced modulus is used to take into account the effects of non-rigid indenters on the load displacement behavior and the Young's modulus, E, can now be solved using a following equation

$$\frac{1}{E_r} = \frac{(1-v^2)}{E} + \frac{(1-v_i^2)}{E_i},$$ (3.7)

where E and v are the Young's modulus and Poisson's ration for the specimen and $E_i$ and $v_i$ are the corresponding parameters for the indenter. In addition to the modulus, the obtained projected area of indentation can also be used to determine the hardness, H, using the equation

$$H = \frac{P_{max}}{A}.$$ (3.8)

It should be noted that the hardness measured using the projected area of indentation determined from the load displacement data may differ from the hardness obtained using the conventional definition in which the area is determined by direct measurement from the optical image of the indentation. The reason for the difference is that a portion of the contact area under the load may not be plastically deformed in all materials and, as a result, the contact area measured by observation of the indentation be less than the size of the indentation at a maximum load (Oliver and Pharr 1992).

The nanoindentation profiles for the ferritic-austenitic interfaces of both welds were measured using a CSM Nanoindentation tester with a Berkovich tip using an indentation load of 15 mN with a step size of 25 μm between the indentations. In addition, to further characterize the fusion boundary properties of the NG-DMW, nanoindentation profiles with indentation load of 3 mN and a step size of 5 μm were determined for the NG-DMW.

## 3.4 Tensile testing and mechanical mismatch determination

Tensile tests were performed for both DMWs in order to determine the stress-strain behavior of the different weld zones of the DMWs. Tensile tests were performed in a room temperature using small-sized flat bar specimens with a cross-section diameter of 1x2 mm and a gauge length of 8 mm. The purpose of using small-sized specimens was to make the sample size of a specimen to be as small as possible to allow more precise determination of the tensile properties of local weld zones, such as the fusion boundary area and the SA 508 HAZ regions. The small-sized flat bar specimens were extracted from the different parts of the SA 508 HAZ, fusion boundary, SA 508 base metal, and Alloy 52/182 weld metals and Alloy 182 buttering.

In addition to the small-sized flat-bar specimens, the SA 508 base metal as well as the Alloy 182 buttering and weld metal and the Alloy 52 wel metal was tested using round bar specimens with a cross-section diameter of ⌀8 mm and a gauge length of 30 mm. The purpose of the round bar specimens was to provide a comparison results to the results obtained using the small-sized flat-bar specimens and, thus, to ensure that the flat bar specimens were of adequate size. The tensile testing specimen geometries and dimensions are shown in Figures 3.12 and 3.13 and Tables 3.2 and 3.3 show the tensile testing matrices of each DMW.
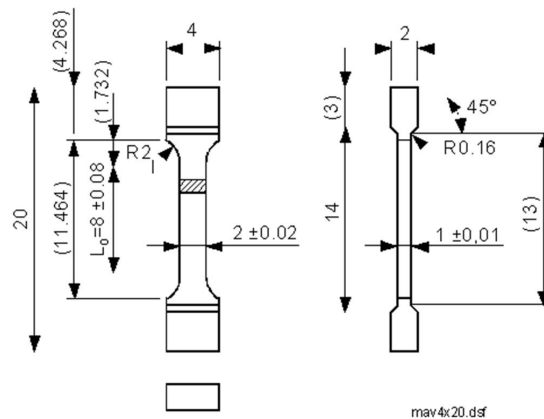


**Figure 3.12.** Techincal drawing of the flat-bar tensile testing specimen.
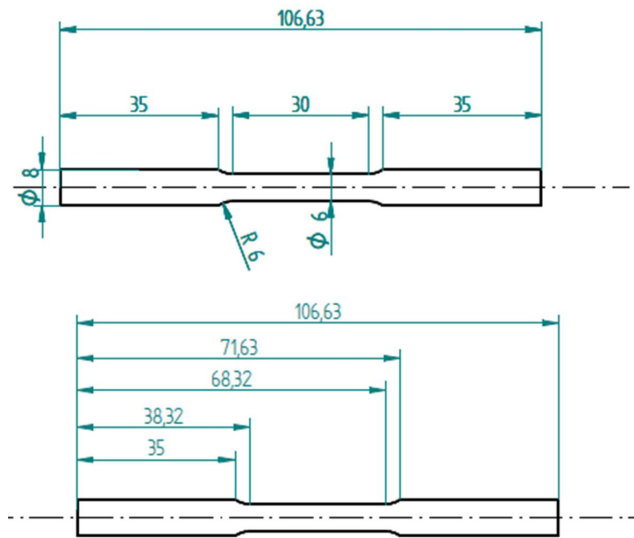
**Figure 3.13.** Techincal drawing of the round bar tensile testing specimen.

**Table 3.2.** BWR-DMW tensile testing matrix.

| DMW zone | Cross-section | Gauge length | n | Specimen notations |
|---|---|---|---|---|
| SA 508 BM round bar | ⌀8 mm | 30 mm | 4 | SA 508 BM 1 - SA 508 BM 4 |
| Alloy 182 butter round bar | ⌀8 mm | 30 mm | 4 | Alloy 182 butter 1 - Alloy 182 butter 4 |
| Alloy 182 WM round bar | ⌀8 mm | 30 mm | 5 | Alloy 182 WM 1 - Alloy 182 WM 5 |
| SA 508 BM flat bar | 1x2 mm | 8 mm | 8 | SA 508 s1 - SA 508 s8 |
| FB + 1 mm flat bar | 1x2 mm | 8 mm | 6 | FB+1 s1 - FB+1 s6 |
| FB flat bar | 1x2 mm | 8 mm | 7 | FB s1 - FB s7 |
| Alloy 182 butter flat bar | 1x2 mm | 8 mm | 8 | 182 butter s1 - 182 butter s8 |
| Alloy 182 WM flat bar | 1x2 mm | 8 mm | 8 | 182 WM s1 - 182 WM s8 |
| Transverse flat bar | 1x2 mm | 8 mm | 8 | Transverse s1 - Transverse s8 |

**Table 3.3.** NG-DMW tensile testing matrix.

| DMW zone | Cross-section | Gauge length | n | Specimen notations |
|---|---|---|---|---|
| SA 508 BM round bar | ⌀8 mm | 30 mm | 4 | SA 508 BM 1 - SA 508 BM 4 |
| Alloy 52 WM round bar | ⌀8 mm | 30 mm | 4 | Alloy 52 WM 1 - Alloy 52 WM 4 |
| SA 508 BM flat bar | 1x2 mm | 8 mm | 3 | SA 508 s1 - SA 508 s3 |
| FB + 2.3 mm flat bar | 1x2 mm | 8 mm | 7 | FB+2.3 s1 - FB+2.3 s7 |
| FB + 2 mm flat bar | 1x2 mm | 8 mm | 3 | FB+2 s1 - FB+2 s3 |
| FB + 1 mm flat bar | 1x2 mm | 8 mm | 3 | FB+1 s1 - FB+1 s3 |
| FB flat bar | 1x2 mm | 8 mm | 3 | FB s1 - FB s3 |
| Alloy 52 WM flat bar | 1x2 mm | 8 mm | 4 | 52 WM s1 - 52 WM s4 |
| Transverse flat bar | 1x2 mm | 8 mm | 3 | Tranverse s1 - Transverse s3 |

Both DMWs were tensile tested in PWHT condition and the testing was performed using an MTS tensile testing system. The displacements during the testing were measured using a strain gage in the case of the round bar specimens.

In the case of the small-sized flat-bar specimens, the displacements were measured without a strain gage since there was a desire to perform digital image correlation (DIC) and, thus, a separate strain gage could not be used.

The stress-strain behavior of each weld zone was charaterized separately by combining the results of all the tested specimens from the specific zone together and using the Hollomon equation (Hollomon 1945)

$$\sigma = K\varepsilon^n \tag{3.9}$$

from the onset of yielding to the maximum load. True stresses and strains were required for the use of Hollomon equation. The true stresses and strains were calculated for each specimen according to the following equations (Hertzberg 1996)

$$\varepsilon_{true} = ln(\varepsilon_{eng} + 1) \tag{3.10}$$

$$\sigma_{true} = \sigma_{eng}(1 + \varepsilon_{eng}) \tag{3.11}$$

and the strain hardening exponent, n, and the material constant, K, were extrapolated from the true stress-strain curve of each specimen. The tensile testing results obtained using small-sized flat-bar specimens were used to calculate the strength mismatch factors for each weld zone according to the SINTAP, which defines the strength mismatch factor M as the ratio of the yield strength of the weld metal $\sigma_{WM}$ to that of the base material $\sigma_{BM}$:

$$M = \frac{\sigma_{WM}}{\sigma_{BM}}. \tag{3.12}$$

## 3.5 Fracture mechanical testing

The fracture mechanical characterization of the DMWs consisted of the determination of J-R curves for the fusion boundary areas, the SA 508 HAZs, and the weld metal or the buttering layer, depending on the DMW mock-up. After the fracture resistance testing, all the tested specimens were fractographically studied and the fracture propagation paths with respect to the local DMW microstructures were determined by preparing cross-section specimens from the relevant fracture mechanical specimens.

### 3.5.1 Fracture mechanical testing specimens

Both welds were characterized using 10x20x100 mm single-edge bend (SE(B)) specimens. The dimensions of the SE(B) specimens used in fracture mechanical testing are presented in Figure 3.14. The specimens were side-grooved prior the fracture mechanical testing and all the specimens, with the exception of the Alloy 182 buttering layer specimens, were extracted so that the referred crack propagation direction was aimed parallel to the weld fusion boundary and the direction of the crack growth was from the inner surface to the outer surface of the mock-up.

**Figure 3.14.** Techincal drawing of the 10x20x100 mm SE(B) specimens used in the fracture mechanical testing.

The BWR-DMW fracture mechanical specimens were extracted from the following locations of the mock-up: notch in the middle of the buttering layer, notch aimed at the fusion boundary, and notch aimed at 2 mm from the fusion boundary into the HAZ of SA 508. The fusion boundary and the SA 508 HAZ specimens were extracted in a tilted position with respect to the plate orientation in order for the fusion boundary to be parallel to the referred crack growth direction. The NG-DMW fracture mechanical specimens were extracted from the fusion boundary, 1 mm from the fusion boundary into the HAZ of SA 508, and 1 mm from the fusion boundary into the Alloy 52 weld metal. The test matrices of the BWR-DMW and NG-DMW fracture mechanical tests are presented in Tables 3.4 and 3.5, respectively.

**Table 3.4.** BWR-DMW fracture mechanical testing matrix.

| DMW zone | 10x20x100 mm SE(B) | |
|---|---|---|
| | n | Specimen notations |
| Alloy 182 buttering layer (PWHT) | 4 | PU1 – PU4 |
| Fusion boundary (PWHT) | 3 | FB1A, FB2B, and FB3C |
| 2 mm from the FB into the HAZ of SA 508 (PWHT) | 3 | FB+2A, HB+2B, and FB+2C |

**Table 3.5.** NG-DMW fracture mechanical testing matrix.

| DMW zone | 10x20x100 mm SE(B) | |
|---|---|---|
| | n | Specimen notations |
| 1 mm from the FB into the Alloy 52 weld metal (As-welded) | 4 | AWFB-1_i1 – AWFB-1_i4 |
| Fusion boundary (As-welded) | 4 | AWFB_i1 – AWFB_i4 |
| 1 mm from the FB into the HAZ of SA 508 (As-welded) | 4 | AWFB+1_i1 – AWFB+1_i4 |
| 1 mm from the FB into the Alloy 52 weld metal (PWHT) | 4 | HTFB-1_i1 – HTFB-1_i4 |
| Fusion boundary (PWHT) | 4 | HTFB_i1 – HTFB_i4 |
| 1 mm from the FB into the HAZ of SA 508 (PWHT) | 4 | HTFB+1_i1 – HTFB+1_i4 |

### 3.5.2 J-R curve determination

Fracture mechanical testing was performed according to the ASTM E1820 standard at a room temperature using the elastic compliance method. The J-R curves were determined according to the ASTM E1820 using a modified construction line and the tensile properties obtained from the flat-bar tensile testing specimens. The construction line slope, M, was calculated for each specimen by fitting the least squares linear regression line to the initial J-R curve data calculated with M = 2 in the region $0.2J_Q \leq J_i \leq 0.6J_Q$. If the data set included less than 6 data points in the evaluation region or if the linear regression gave a value less than M = 2, the value of M was set to 2.

There are also several criteria which have to be met in order for the test to be classified as a valid J-R test according to the ASTM E1820. The shape of the crack needs to fulfill several geometrical requirements and the acceptable specimen size is dependant on the toughness and flow stress of the tested material. In general, the fracture mechanics standards, including ASTM E1820, are designed for testing of homogeneous materials. The specimens of this study were heterogeneous, i.e. had inhomogeneous microstructure and mechanical properties, which may result in crack path deflection and, thus, unevenness in the crack front shape. The specimens were also quite inhomogeneous in terms of toughness and flow stress, which resulted in quite different specimen size requirements. Therefore, it should be noted that the crack geometry and the specimen size acceptability requirements were not always fulfilled and all the J-R tests presented in this study are necessarily not valid according to the ASTM E1820.

### 3.5.3 Fractography and crack path characterization

The determination of fracture mechanical properties of the local microstructural zones of a DMW requires the fatigue precrack to be positioned as accurately as possible to the zone reguired to be tested. The accurate positioning of fatigue precrack can be very challenging due to the curved fusion boundary as well as the tendency for sudden crack path deflection towards another microstructural zone after a ductile dimple initiation event. It has been shown (Nevasmaa et al. 2000, Laukkanen et al. 2001, Keinänen et al. 2003, Faidy et al. 2004) that even in the case of ductile fracture behavior, the acquired fracture resistance curve can vary a lot depending on the accurate position of the fatigue precrack and the subsequent crack propagation within the DMW. Detailed post-test fractography and metallography are, therefore, necessary to identify the actual crack initiation site and propagation path in order to relate the obtained fracture resistance to the correct microstructural zone.

After the fracture mechanical testing, the fracture surfaces of all the tested SE(B) specimens were analysed using optical 3D profilometry. The 3D profilometric measurements were performed for the SA 508 side halves of the BWR-DMW specimens and Alloy 52 side halves of the NG-DMW specimens. The results of the 3D profilometry measurements are 3D topography maps showing optical representations of the fracture surface roughnesses with the differences

in altitudes illustrated with a colour scale from blue to red. All the fracture surfaces were also charaterized by FESEM/EDS study. The fracture propagation paths with respect to the local DMW microstructures were determined by preparing cross-section samples from the fracture mechanical specimens. The cross-section specimens were cut perpendicular to the crack propagation direction and the specimens were grinded and polished similarly with the microstructural specimens and studied using optical microscopy and FESEM.

# 4 Results

The results section consists of the results obtained from the microstructural characterization, Vickers hardness and nanoindentation measurements, tensile testing, and fracture mechanical testing and analysis. The results include the comparison between the tensile testing and fracture mechanical testing results as well as calculation of the mismatch factors based on the tensile testing results of the flat-bar tensile specimens. Fractography and crack path examination of the fracture mechanical specimens are presented as well. The results have also been published in Holmström et al. (2013), Sarikka et al. (2014), Sarikka et al. (2016A), and Sarikka et al. (2016B). The tensile testing with the miniature-sized flat-bar specimens and the fracture mechanical testing were performed at VTT and the microstructural characterization, hardness testing, and the analysis of the test results were performed at Aalto University.

## 4.1 Microstructural characterization

Figure 4.1 shows optical micrographs of the SA 508-Alloy 182 interface of the BWR-DMW showing the SA 508 HAZ and the SA 508-Alloy 182 fusion boundary area. The higher magnification images were taken from the SA 508 base metal, 2 mm and 1 mm from the fusion boundary into the SA 508 HAZ, and immediately next to the fusion boundary.

   The SA 508 HAZ shows characteristics typical to a HAZ of a LAS. The SA 508 base metal has a ferritic-bainitic microstructure (i.e. ferrite and bainite with non-aligned and aligned second phase). The HAZ closer to the fusion boundary has experienced higher peak temperatures during welding and that has resulted in grain coarsening, see Figure 4.1d. In the partially grain-refined region, prior bainite blocks have transformed to austenite and grown slightly into prior ferrite grains upon heating and during cooling; consequently, this region has decomposed into fine blocks of bainite with the prior untransformed ferrite remaining unchanged. In the grain-refined region, the transformation of bainite blocks and ferrite grains into austenite has been complete. In the grain-coarsened region, the austenite grains are larger because the peak temperature during welding has been higher, hence triggering the austenite grain growth. The grain-coarsened HAZ microstructure consists of parallel, elongated ferrite laths with carbides mostly aligned between laths, hence resembling upper-bainite. In addition, ferrite with intra-lath carbides appears occasionally, hence resembling lower-bainite. The distribution of the resulting bainite and ferrite is non-uniform because the heating during welding has been rapid, preventing complete

dissolution of carbides. The width of the HAZ varies depending on the location but is overall around 2 to 3 mm.
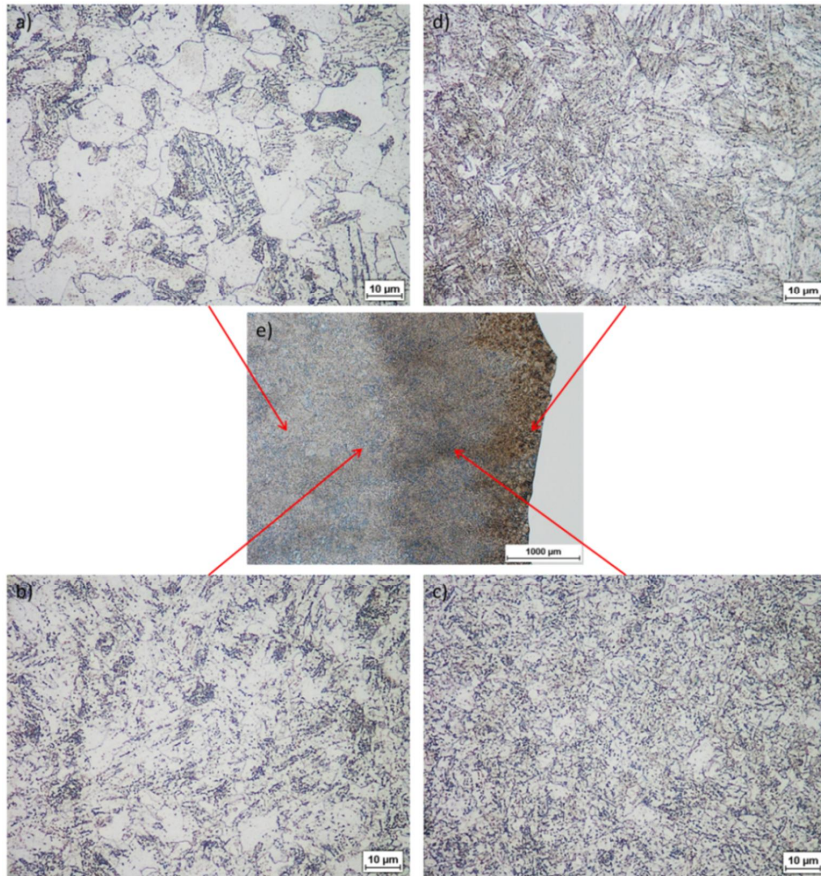


**Figure 4.1.** Optical micrographs showing the microstructure at the a) SA 508 base metal, b) partially grain-refined region, c) grain-refined region, and d) fusion boundary area of the BWR-DMW. Image e) represents a lower magnification overall image of the SA 508-Alloy 182 interface showing the different regions of the SA 508 HAZ and the fusion boundary.

Figure 4.2 shows EBSD band contrast, band contrast with high angle GBs and low angle GBs, inverse pole figure (IPF), and local mis-orientation maps of the SA 508 base metal. The microstructure of the SA 508 base metal is ferritic-upper bainitic consisting of ferrite grains surrounded by grains with lamellar sub-grain structure with a lot of low angle GBs. The ferrite plates in the SA 508 base metal are quite free of local mis-orientation. According to the EBSD measurements, the average grain size of the SA 508 base metal is about d = 8.3 μm.
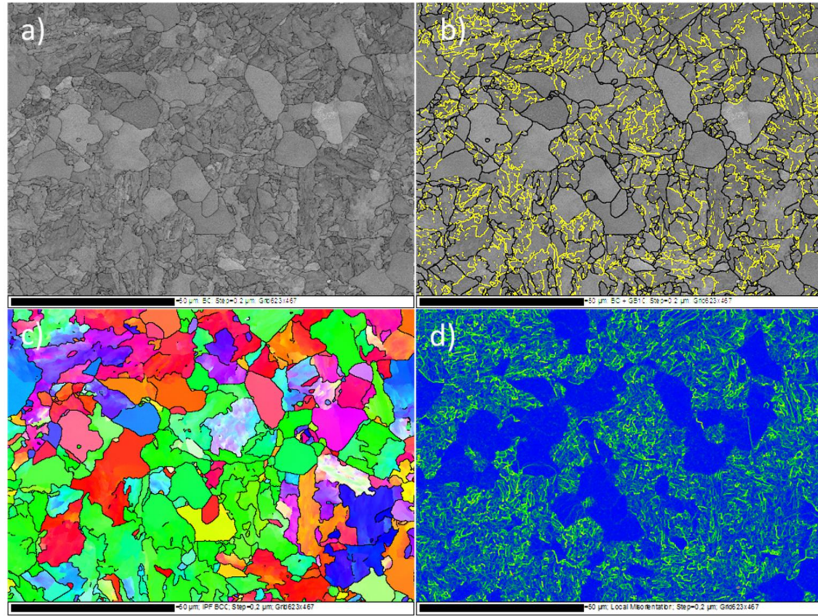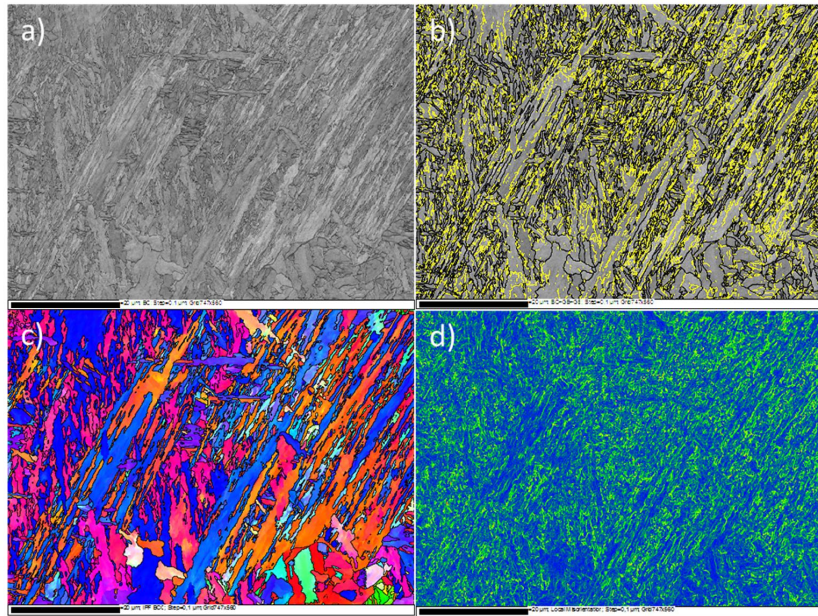
**Figure 4.2.** EBSD a) band contrast, b) band contrast with high angle GBs (black) and low angle GBs (yellow), c) IPF, and d) local mis-orientation maps showing the microstructure of the SA 508 base metal.

EBSD maps taken from the different regions of the SA 508 HAZ at locations corresponding to the locations of the images in Figure 4.1 are shown in Figures 4.3, 4.4, and 4.5. The grain size decreases moving towards the fusion boundary from the SA 508 base metal to the partially grain-refined region and further on to the grain-refined region. The average grain size of the partially grain-refined region is about d = 3.7 μm and the average grain size of the grain-refined region is about d = 2.4 μm, according to the EBSD measurements.

The metal has experienced its highest peak temperature and largest heat cycle in the coarse-grained region next to the fusion boundary. That has resulted in an austenitie grain growth followed by bainite and acicular ferrite formation during rapid cooling. The acicular ferrite and bainite formation has caused higher local mis-orientation in the microstructure, as can be seen from Figure 4.5. The ferrite grain structure in the partially grain-refined and grain-refined regions is equiaxial and in the coarse-grained region, due to the larger austenite grain size and the higher cooling rates, the ferrite grains have elongated needle-shaped structure. The local mis-orientation increases towards the fusion boundary indicating a higher strain near the fusion boundary.
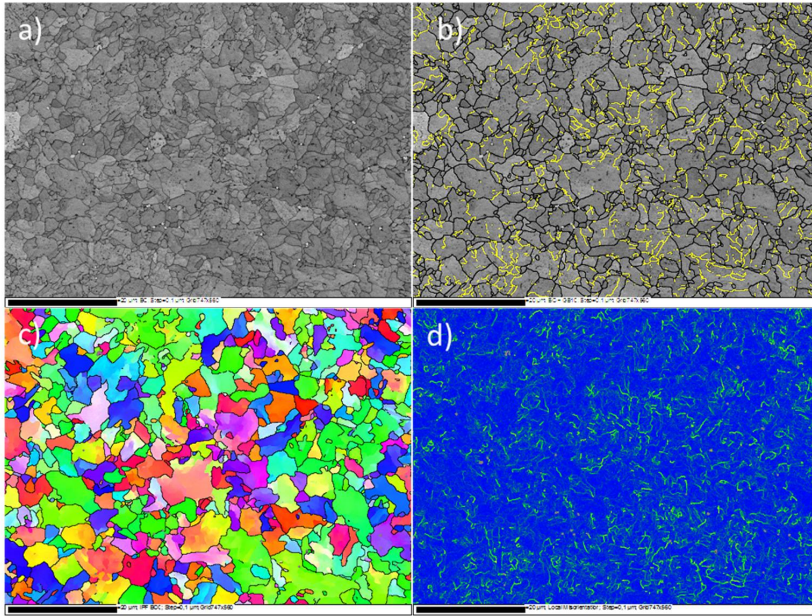
**Figure 4.3.** EBSD a) band contrast, b) band contrast with high angle GBs (black) and low angle GBs (yellow), c) IPF, and d) local mis-orientation maps showing the microstructure of the partially grain-refined region of the SA 508 HAZ.
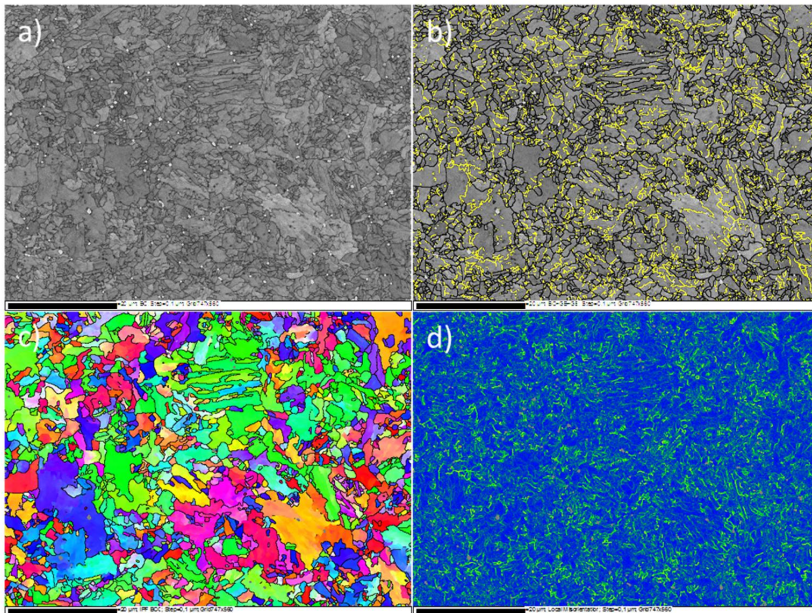


**Figure 4.4.** EBSD a) band contrast, b) band contrast with high angle GBs (black) and low angle GBs (yellow), c) IPF, and d) local mis-orientation maps showing the microstructure of the grain-refined region of the SA 508 HAZ.

**Figure 4.5.** EBSD a) band contrast, b) band contrast with high angle GBs (black) and low angle GBs (yellow), c) IPF, and d) local mis-orientation maps showing the microstructure of the grain-coarsened region of the SA 508 HAZ.

Figure 4.6 shows an optical micrograph and an SEM image of the SA 508-Alloy 182 interface of the BWR-DMW mock-up and Figure 4.7 shows EBSD band contrast and phase maps taken from the fusion boundary region. A narrow martensitic zone and a Type II boundary are present at the fusion zone of the BWR-DMW. The martensitic zone is located right at the fusion boundary and the Type II boundary is running at around some tens of µm from the fusion boundary into the Alloy 182 buttering. Both of these, the martensitic zone and the Type II boundary, are discontinuous. The width of the martensitic zone is around 10 µm. There is also a carbide-free zone present next to the fusion boundary in the Alloy 182 buttering.
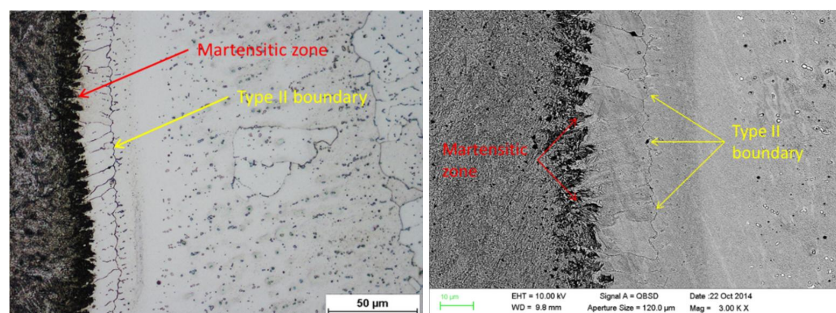


**Figure 4.6.** Optical micrograph and an SEM image showing the martensitic zone and the Type II boundary at the SA 508-Alloy 182 interface.
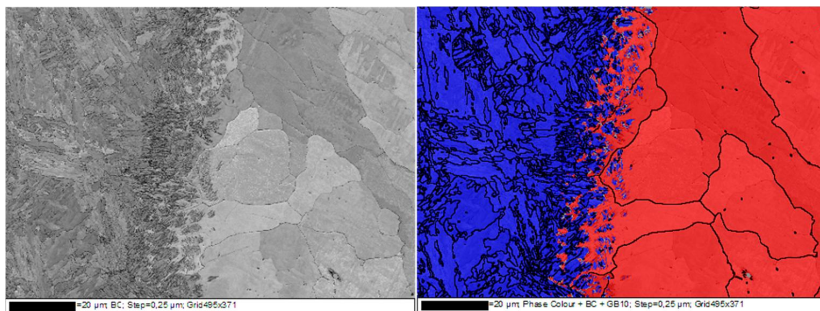
**Figure 4.7.** EBSD band contrast and phase maps showing the martensitic zone. Blue colour indicates BCC crystal structure and red color FCC crystal structure.

The microstructure of the Alloy 182 buttering layer is presented in Figure 4.8. The Alloy 182 has a dendritic microstructure consisting of columnar and cellular dendritic structure.
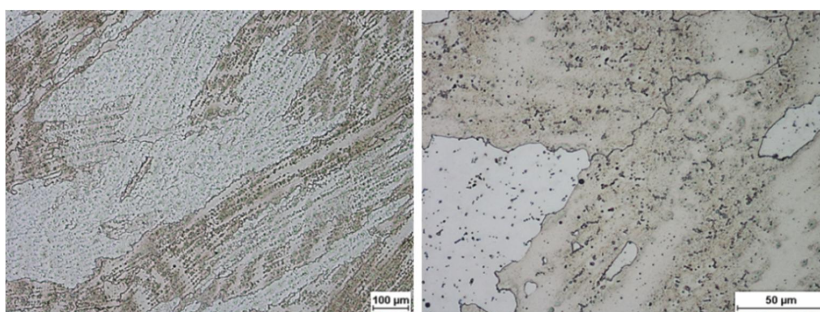


**Figure 4.8.** Optical micrographs showing the dendritic microstructure of Alloy 182 buttering layer.

Figure 4.9 shows EDS line scans across the SA 508-Alloy 182 fusion boundary of the BWR-DMW mock-up. The martensitic zone causes a Fe concentration drop and a Ni concentration increase at about 80 μm distance. The weld dilution causes an increased Fe and decreased Ni and Cr concentrations in the solidified weld metal next to the fusion boundary compared to the nominal composition of the Alloy 182 filler material. Another notable change in the Fe and Ni compositions can be seen at the Type II boundary, where there is an increase in the Fe compostion and decrease in the Ni composition. After the Type II boundary, the Fe concentration and Ni concentration settle down to about 25 wt. % and close to 60 wt. %, respectively.

64
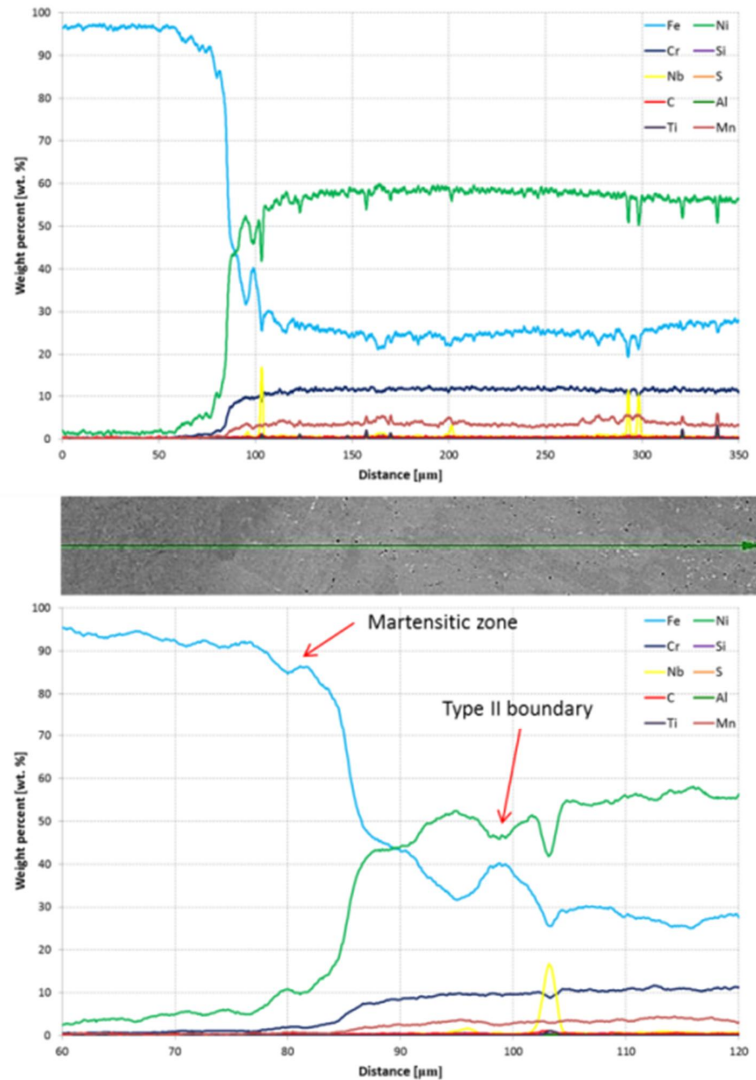
**Figure 4.9.** EDS line scans across the SA 508-Alloy 182 interface. The lower graph is a magnification of the upper graph in between 60 and 120 μm distances. Notice the composition changes in the Fe and Ni in the martensitic zone and at the Type II boundary.

Figures 4.10 and 4.11 show optical micrographs of the SA 508-Alloy 52 interface of as-welded and PWHT condition NG-DMW, respectively. The higher magnification images have been taken from the SA 508 base metal, 2 mm from the fusion boundary into the SA 508 HAZ, 1 mm from the fusion boundary into the SA 508 HAZ, and from the fusion boundary.
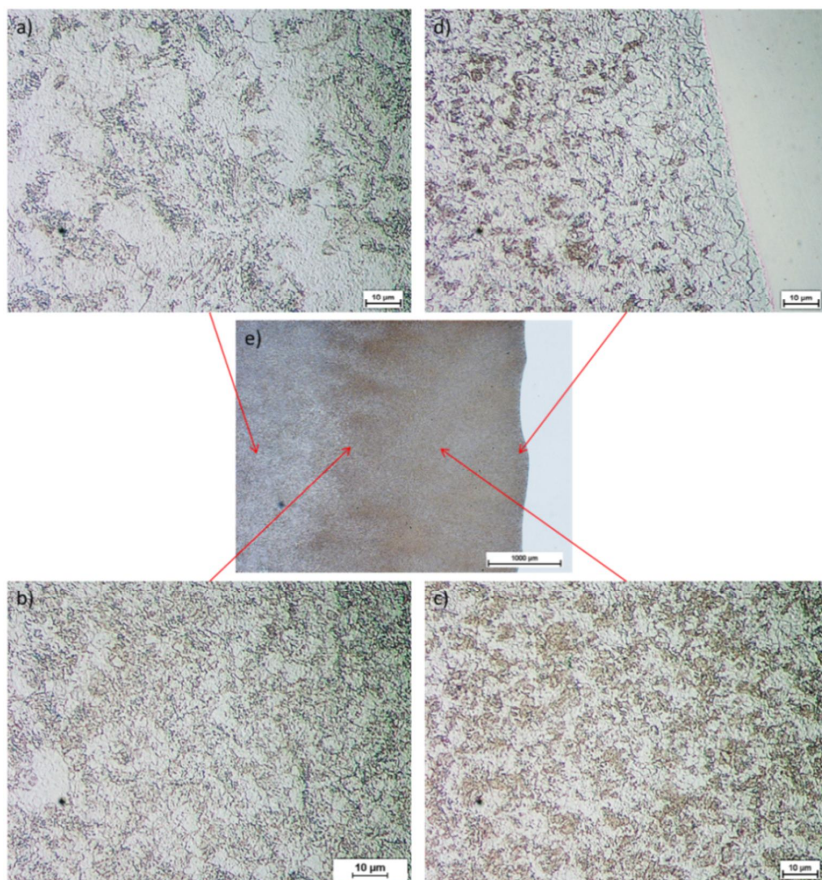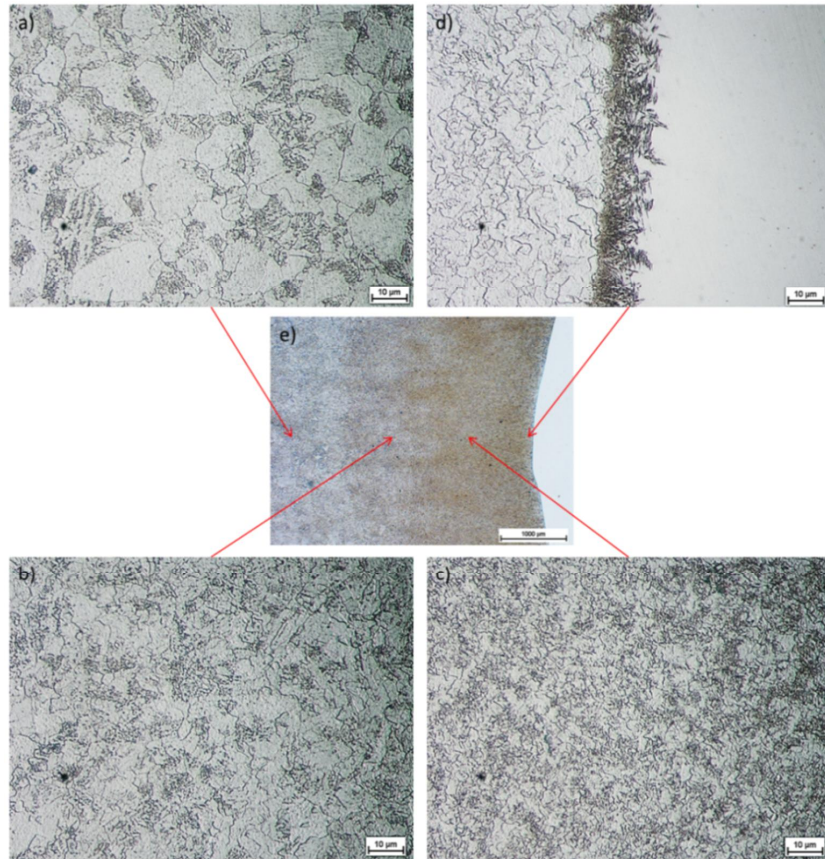
**Figure 4.10.** Optical micrographs showing the microstructure at the a) SA 508 base metal, b) partially grain-refined region, c) grain-refined region, and d) fusion boundary area of the as-welded state NG-DMW. Image e) represents a lower magnification overall image of the SA 508-Alloy 52 interface showing the different regions of the SA 508 HAZ and the fusion boundary.

Similarly to the SA 508 HAZ in the BWR-DMW, the SA 508 HAZ in the NG-DMW shows characteristics typical to a HAZ of a LAS. The SA 508 base metal has a ferritic-upper bainitic microstructure. The partially grain-refined region is decomposed of fine colonies and grains of ferrite and cementite with the prior untransformed ferrite remaining unchanged. In the grain-refined region, the transformation of bainite and ferrite grains into austenite has been complete and upon cooling, the austenite grains have decomposed into small colonies and grains of ferrite and cementite. The grain-coarsened region, however, differs from that of the BWR-DMW. The microstructure of the grain-coarsened region of the NG-DMW is quite similar to the microstructure of the grain-refined region instead of consisting of needle-shaped acicular ferrite, similarly to the BWR-DMW. Also, the grain-coarsened region of the SA 508 HAZ in the NG-DMW is clearly narrower than that of the BWR-DMW. The base material, partially grain-refined region, and grain-refined region are clearly distinguishable from the SA 508 HAZ of the NG-DMW of both heat treatment conditions and the overall microstructural characteristics were similar in the SA 508 HAZ of both heat treatment conditions. Another notable difference in the NG-DMW

with respect to the BWR-DMW is the existence of a CDZ next to the fusion boundary in the SA 508 side. The width of the SA 508 HAZ in the NG-DMW is approximately 3 mm.



**Figure 4.11.** Optical micrographs showing the microstructure at the a) SA 508 base metal, b) partially grain-refined region, c) grain-refined region, and d) fusion boundary area of the PWHT state NG-DMW. Image e) represents a low magnification overall image of the SA 508-Alloy 52 interface showing the different regions of the SA 508 HAZ and the fusion boundary.

EBSD maps taken from the different regions of the SA 508 HAZ of PWHT state NG-DMW at locations corresponding to the locations of the images in Figure 4.11 are shown in Figures 4.12, 4.13, and 4.14. The grain size decreases moving towards the fusion boundary from the SA 508 base metal to the partially grain-refined region and to the grain-refined region. The average grain size of the partially grain-refined region is about d = 2.9 μm and the average grain size of the grain-refined region is about d = 1.8 μm, according to the EBSD measurements.
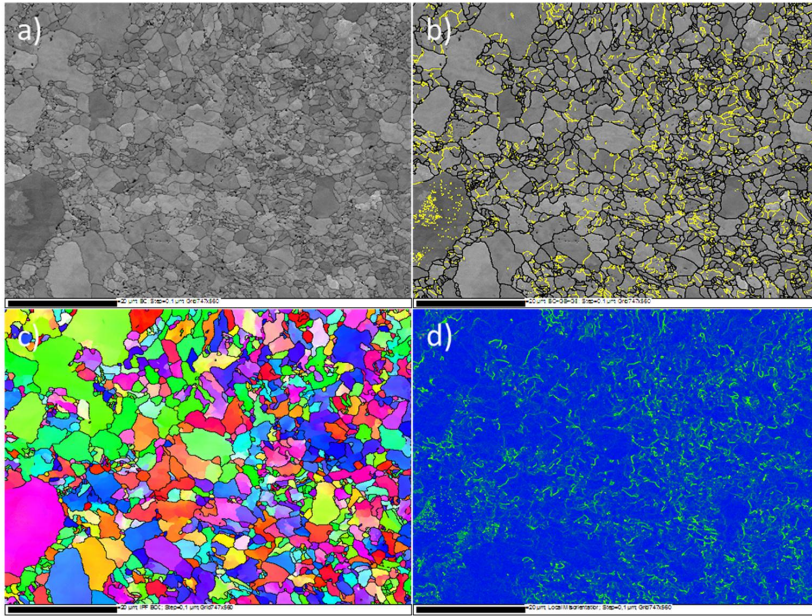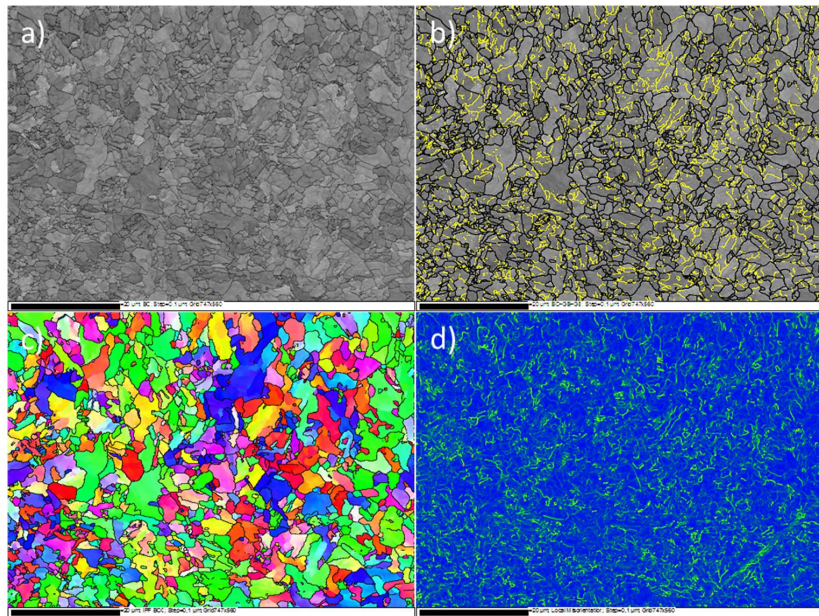
**Figure 4.12.** EBSD a) band contrast, b) band contrast with high angle GBs (black) and low angle GBs (yellow), c) IPF, and d) local mis-orientation maps showing the microstructure of the partially grain-refined region of the SA 508 HAZ.
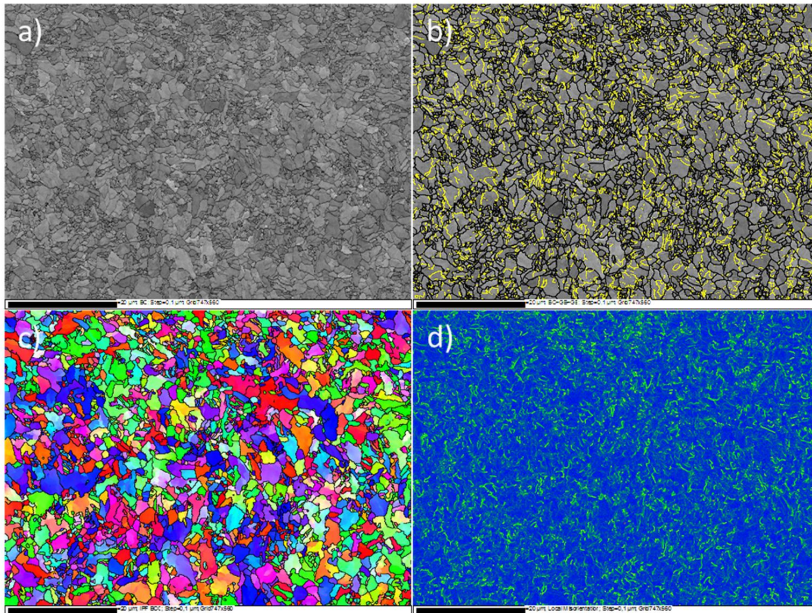


**Figure 4.13.** EBSD a) band contrast, b) band contrast with high angle GBs (black) and low angle GBs (yellow), c) IPF, and d) local mis-orientation maps showing the microstructure of the grain-refined region of the SA 508 HAZ.

The main difference in the microstructures of the SA 508 HAZ regions between the BWR-DMW and NG-DMW is the microstructure of the grain-coarsened region. The grain-coarsened region of the SA 508 HAZ of the NG-DMW consists

of equiaxial ferrite grains and cementite, whereas the grain-coarsened region of the SA 508 HAZ of BWR-DMW consisted of the lenticular, elongated microstructure. The difference suggests that, due to the lower net heat input of the NG-DMW, the peak temperature and, especially, the cooling rate near the fusion boundary region have been clearly lower in the NG-DMW than in the BWR-DMW. Thus, the austenite grain growth has not been as significant and the resulting microstructure is closer to the microstructure of the grain-refined region. Also, the local mis-orientation in the grain-coarsened region near the fusion boundary is clearly lower in the NG-DMW than it is in the BWR-DMW. The average grain size of the grain-coarsened region is about 2.6 μm, according to the EBSD.



**Figure 4.14.** EBSD a) band contrast, b) band contrast with high angle GBs (black) and low angle GBs (yellow), c) IPF, and d) local mis-orientation maps showing the microstructure of the grain-coarsened region of the SA 508 HAZ.

Similarly to the BWR-DMW, a discontinuous martensitic zone was present next to the fusion boundary in the NG-DMW. EBSD band contrast and phase maps showing the martensitic zone in the SA 508-Alloy 52 fusion boundary are presented in Figure 4.15. The width of the martensitic zone is around 10 μm. In addition to the martensitic zone, in BWR-DMW, there was a Type II boundary present next to the fusion boundary in the weld metal side and although it was discontinuous, it was still ordinarily present next to the fusion boundary. In the NG-DMW, a Type II boundary could be found from the fusion boundary region; however, the presence of it is very local and very often it was not present.
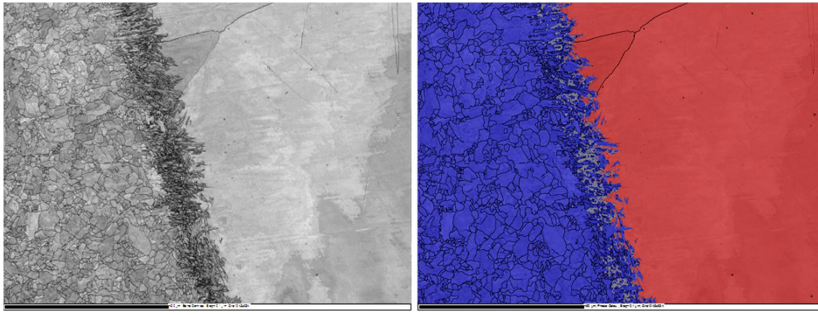
**Figure 4.15.** EBSD band contrast and phase maps showing the martensitic zone. Blue colour indicates BCC crystal structure and red color FCC crystal structure.
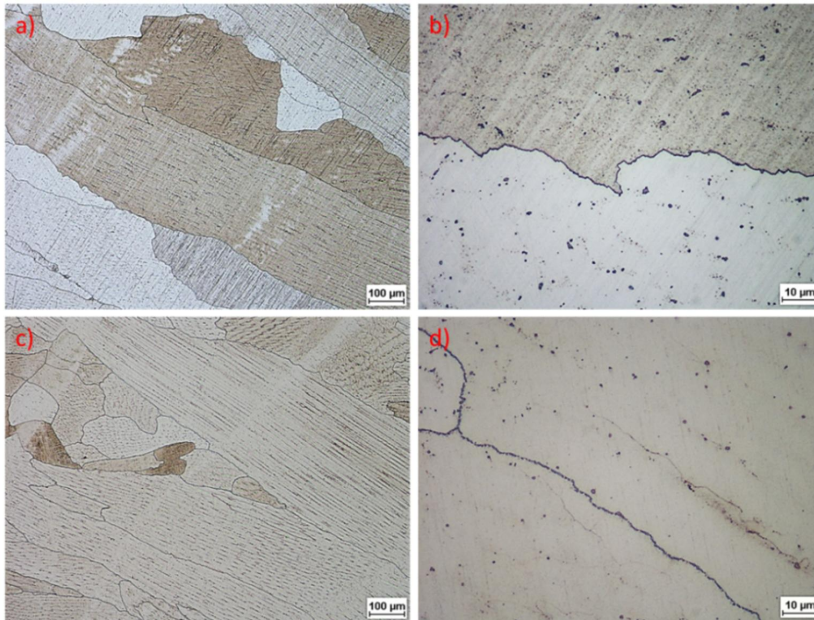


**Figure 4.16.** Optical micrographs showing the dendritic microstructure of Alloy 52 weld metal in a) and b) as-welded state and c) and d) PWHT state NG-DMW.

The microstructure of the Alloy 52 weld metal in as-welded and PWHT state is presented in Figure 4.16. The Alloy 52 has a dendritic microstructure consisting of columnar and cellular dendritic structure. The dendrite boundaries are full of Ti carbides and the amount of carbides in the dendrite boundaries increases as a result of PWHT.

Figure 4.17 shows EDS line scans across the SA 508-Alloy 52 fusion boundary of the NG-DMW mock-up from a location with the martensitic zone present and from a location without the martensitic zone. The Fe, Cr, and Ni composition gradients are less steep across the interface where there is a martensitic zone present and there are a small decrease in Fe concentration and a small increase in Ni concentration at the martensitic zone similar to the BWR-DMW. The dilution of Fe, Cr, and Ni occurs overall in a short distance after the fusion bound-

ary in the Alloy 52 side. The composition gradients varied depending on the location in the interface and the PWHT did not have a major effect on the dilution of the Fe, Cr, and Ni.
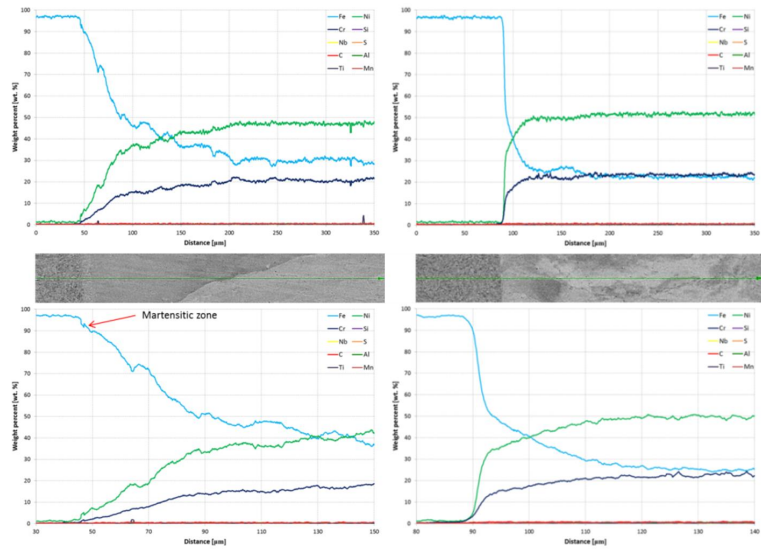


**Figure 4.17.** EDS line scans across the PWHT state SA 508-Alloy 52 interface with martensitic zone (left) and without a martensitic zone (right) present. The lower graphs are magnifications of the upper graphs near the fusion boundary areas.

From the microstructural point of view the PWHT had two significant effects on the SA 508-Alloy 52 interface of the NG-DMW mock-up. Figure 4.18 shows optical micrographs of the fusion boundary area of NG-DMW of as-welded and PWHT states. As can be seen, in the SA 508 side there is clearly a zone with a significantly lower amount of carbides in the interface of the weld in as-welded and PWHT condition. However, in the PWHT state weld, the CDZ is clearly wider than in the as-welded state weld. The width of the CDZ is roughly 10 μm in the as-welded state interface and around 50 μm in the PWHT state interface. The existence of the CDZ in the interface is caused by carbon migration from the SA 508 to the Alloy 52 and the PWHT increases the rate of carbon migration resulting in the wider CDZ.
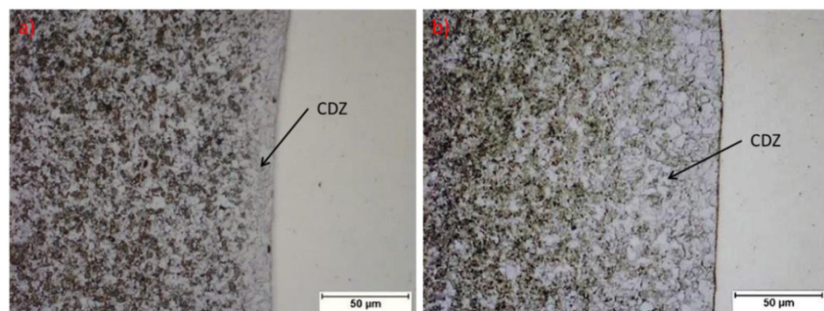


**Figure 4.18.** Optical micrographs showing the CDZ at the fusion boundary of a) as-welded and b) PWHT state NG-DMW. Note the difference in the width of the CDZ.

Another major difference in the microstructure between the weld in as-welded and PWHT condition can be seen in Figure 4.19, which shows optical micrographs of the fusion boundary area of NG-DMW of as-welded and PWHT states etched with aqua regia. In the PWHT state fusion boundary, there is a narrow white layer and a dark layer present next to the fusion boundary in the Alloy 52 weld metal side. The white and dark layers found from the PWHT state fusion boundary are not present in the as-welded state interface.
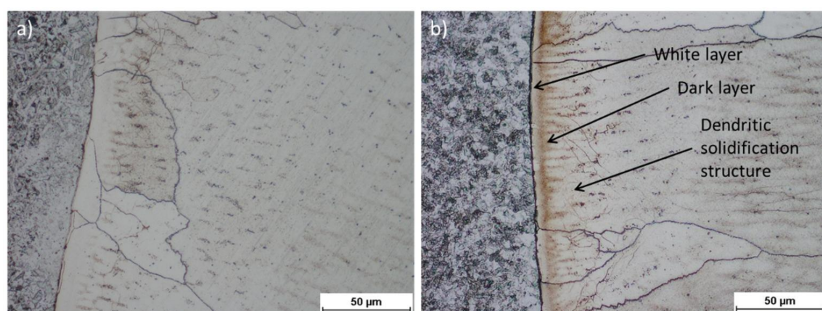


**Figure 4.19.** Optical micrographs showing the fusion boundary characteristics of a) as-welded state and b) PWHT state NG-DMW. Notice the difference in the Alloy 52 side of the fusion boundary between the as-welded and PWHT conditions.

Figures 4.20 and 4.21 show EDS maps of the fusion boundary area of the NG-DMW of as-welded and PWHT states, respectively. The EDS maps reveal that the extra feature in the PWHT state fusion boundary area is a zone with higher concentration of C. The EDS maps of the as-welded state fusion boundary area reveal also an enrichment of C next to the fusion boundary, however that is significantly narrower than the C-pileup in the PWHT state interface. Figure 4.22 shows SEM images of the fusion boundary area of as-welded and PWHT state NG-DMW showing the zone with high carbon concentration next to the fusion boundary.
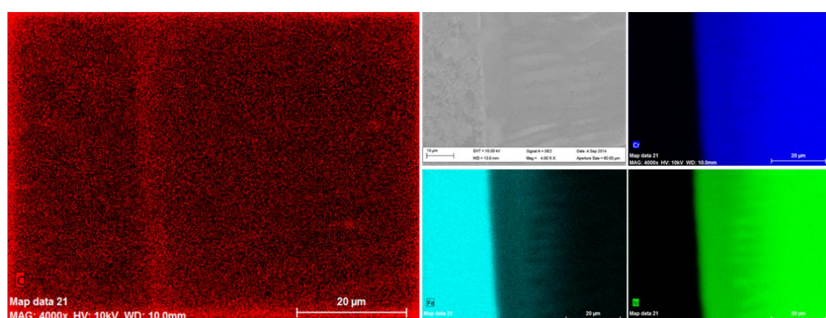


**Figure 4.20.** EDS maps showing the distribution of Fe, Ni, Cr, and C in the SA 508-Alloy 52 interface of the as-welded state NG-DMW. Notice the narrow pile-up of C next to the fusion boundary.
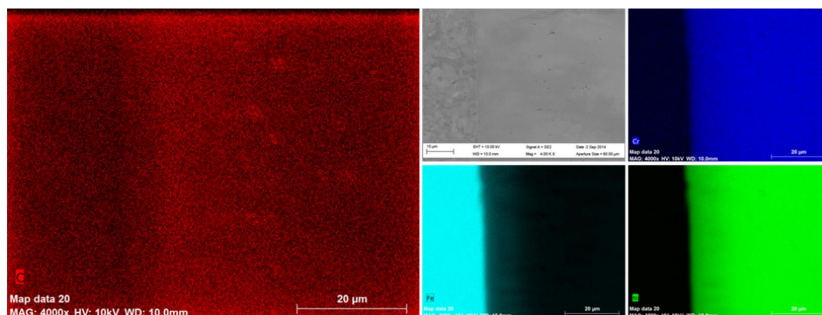
**Figure 4.21.** EDS maps showing the distribution of Fe, Ni, Cr, and C in the SA 508-Alloy 52 interface of the PWHT state NG-DMW. Notice the wider pile-up of C next to the fusion boundary.
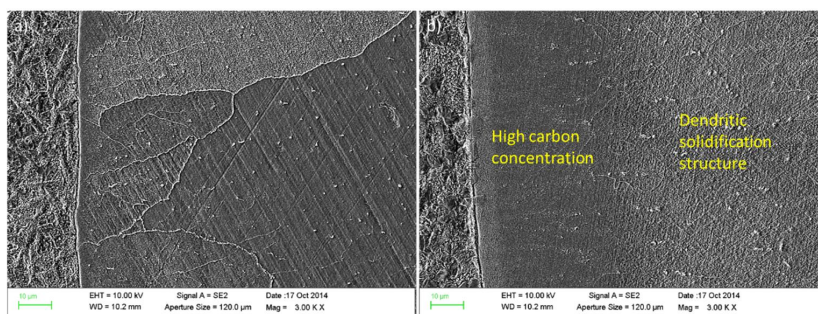


**Figure 4.22.** SEM images showing the fusion boundary characteristics of a) as-welded and b) PWHT state NG-DMW.

## 4.2 Hardness testing

HV0.3 hardness profile across the ferritic-austenitic SA 508-Alloy 182 interface of BWR-DMWs is shown in Figure 4.23 and HV0.3 hardness profiles across the ferritic-austenitic SA 508-Alloy 52 interface of as-welded and PWHT state NG-DMWs are shown in Figures 4.24 and 4.25. All the hardness profiles show quite similar, typical low alloy steel weld characteristics as the hardness increases step by step from base metal to partially grain refining HAZ to grain refining HAZ and starts to decrease near the fusion boundary in the grain-coarsening region of the HAZ. The hardness settles down to the average value of the weld metal quite fast after the fusion boundary. The PWHT decreases the average hardness of the SA 508 HAZ and the base metal whilst increasing the average hardness of the Alloy 52 weld metal.
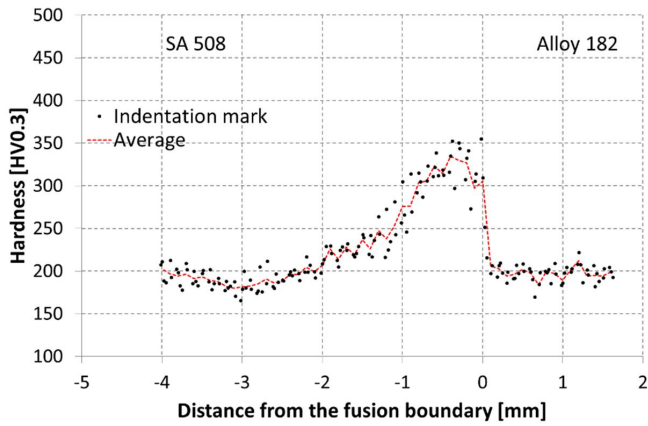
**Figure 4.23.** HV0.3 hardness profile across the SA 508-Alloy 182 interface of BWR-DMW.
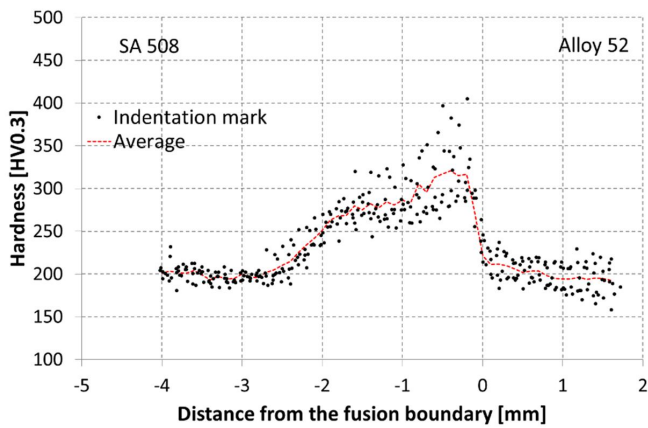


**Figure 4.24.** HV0.3 hardness profile across the SA 508-Alloy 52 interface of as-welded state NG-DMW.
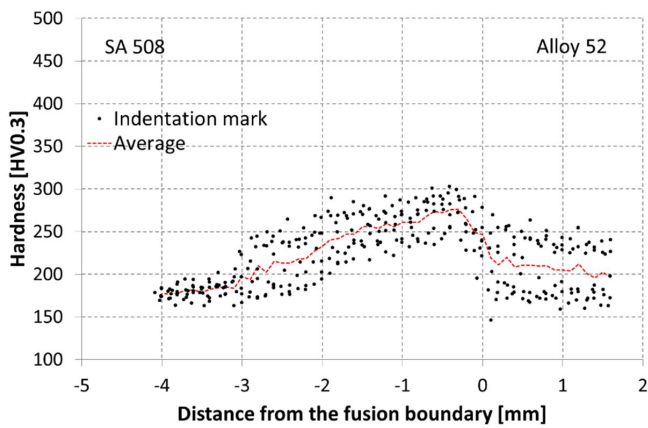


**Figure 4.25.** HV0.3 hardness profile across the SA 508-Alloy 52 interface of PWHT state NG-DMW.

Nanoindentation profiles, in contrast, show quite significant differences in the near-fusion boundary characteristics of the different interfaces of the different DMWs and different heat treatment conditions. Figure 4.26 shows 15 mN nanoindentation profile measured across the SA 508-Alloy 182 interface of the BWR-DMW and Figures 4.27 and 4.28 show 15 mN nanoindentation profiles measured across the SA 508-Alloy 52 interface of as-welded and PWHT states, respectively. In the SA 508-Alloy 182 interface, the lowest hardness exists next to the fusion boundary in the Alloy 182 side whereas in the SA 508-Alloy 52 interface the lowest hardness values are measured from the SA 508 side of the fusion boundary.

In the BWR-DMW, a couple of visibly higher hardness values are observed right next to the fusion boundary. These two indentations showing significantly higher hardness values have landed right on the martensitic zone explaining the higher hardness values. Since the martensitic zone is discontinuous, the hardness peak near the fusion boundary is also discontinuous. In the PWHT NG-DMW, there is a narrow zone with significantly higher hardness right next to the fusion boundary in the Alloy 52 weld metal side. In addition to the harder zone, the presence of the CDZ is clearly visible in the hardness measurement results as a softer narrow zone next to the fusion boundary in the SA 508 HAZ. The CDZ is softer and wider in the PWHT weld than in as-welded state weld.
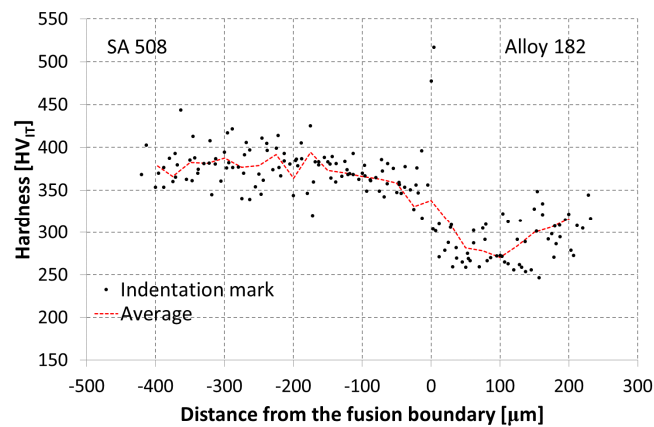


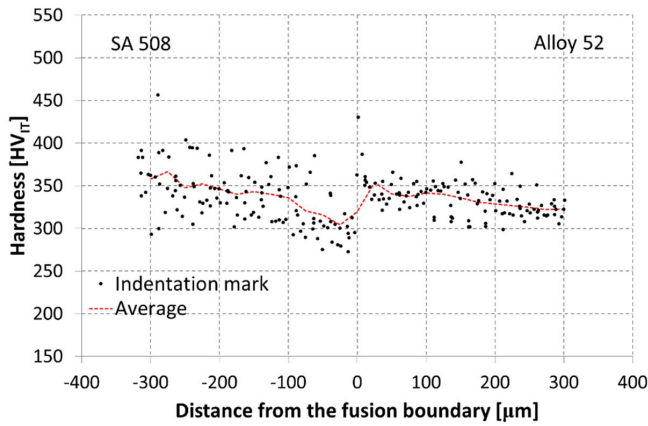**Figure 4.26.** 15 mN nanoindentation profile across the SA 508-Alloy 182 interface of BWR-DMW.

**Figure 4.27.** 15 mN nanoindentation profile across the SA 508-Alloy 52 interface of as-welded state NG-DMW.
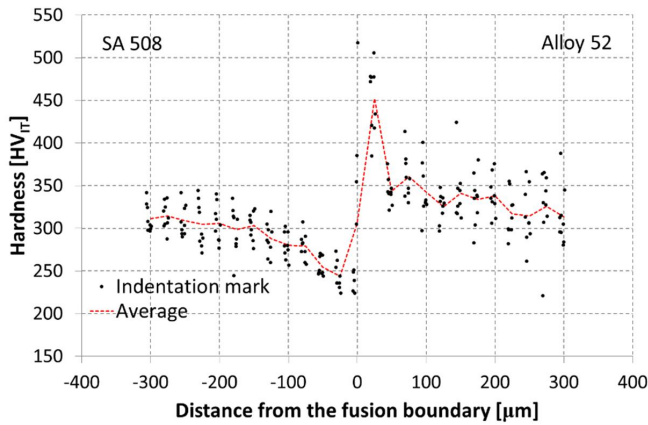


**Figure 4.28.** 15 mN nanoindentation profile across the SA 508-Alloy 52 interface of PWHT state NG-DMW.

Figures 4.29 and 4.30 show nanoindentation profiles measured across the SA 508-Alloy 52 interface of as-welded and PWHT states using an indentation load of 3 mN. The hardness profile of the PWHT state interface shows a small amount of scatter and the profile is quite consistent. The width of the zone with significantly higher hardness next to the fusion boundary is roughly 10 to 20 µm, which corresponds well with the width of the higher C-concentration zone found next to the fusion boundary of the PWHT state NG-DMW. The lower indentation load reveals high hardness values also at the fusion boundary area of the as-welded state NG-DMW. The higher hardness values are measured only from an area of around a couple microns wide right next to the fusion boundary. This also corresponds well with the width of the very narrow higher C- concentration zone next to the fusion boundary in the as-welded state NG-DMW.
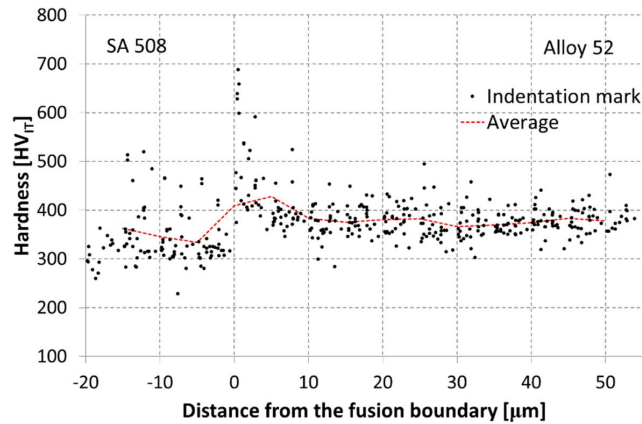
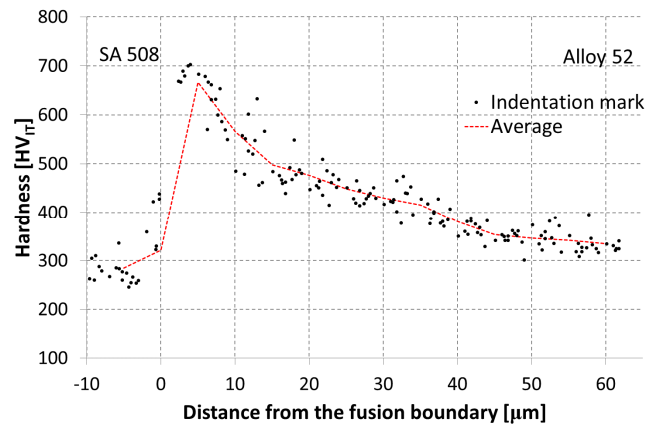**Figure 4.29.** 3.0 mN nanoindentation mapping across the SA 508-Alloy 52 interface of as-welded state NG-DMW.



**Figure 4.30.** 3.0 mN nanoindentation mapping across the SA 508-Alloy 52 interface of PWHT state NG-DMW.

## 4.3 Tensile testing

The tensile test results of the BWR-DMW specimens are shown in Table 4.1 and Figure 4.31 shows a true stress-strain curve of each BWR-DMW zone according to Hollomon equation using average tensile data from the Table 4.1. According to the tensile test results of the round bar specimens, the yield strength values of the SA 508 base metal, Alloy 182 buttering, and Alloy 182 weld metal are 426 MPa, 381 MPa, and 366 MPa and the tensile strength values are 602 MPa, 648 MPa, and 628 MPa, respectively. The fusion boundary specimens show the highest strength values with an average yield strength of 514 MPa and the specimens extracted from the SA 508 HAZ show strength values nearly as high as the fusion boundary specimens. The strength values of the specimens with different sizes and geometries correspond quite well with each other. The differences between the yield strength values fit within the standard deviation and

the differences between the tensile strength values are quite small as well, only few percents.

**Table 4.1.** Tensile test results showing the yield strength ($R_{p0.2}$), ultimate tensile strength ($R_m$), uniform elongation ($A_g$), elongation to fracture (A), strain hardening coefficient (n), and Young's modulus (E) of the tested BWR-DMW zones.

| Specimen | $R_{p0.2}$ [MPa] | $R_m$ [MPa] | $A_g$ [mm/mm] | A [mm/mm] | n | E [GPa] |
|---|---|---|---|---|---|---|
| SA 508 BM round bar | 426 | 602 | 0.111 | 0.287 | 0.189 | 210 |
| Standard deviation | 13 | 8 | 0.008 | 0.042 | 0.002 | 6 |
| Alloy 182 butter round bar | 381 | 648 | 0.327 | 0.456 | 0.442 | 168 |
| Standard deviation | 36 | 4 | 0.009 | 0.008 | 0.024 | 9 |
| Alloy 182 WM round bar | 366 | 628 | 0.353 | 0.467 | 0.442 | 163 |
| Standard deviation | 27 | 13 | 0.026 | 0.024 | 0.035 | 5 |
| SA 508 BM flat bar | 417 | 591 | 0.117 | 0.234 | 0.185 | - |
| Standard deviation | 4 | 7 | 0.007 | 0.011 | 0.002 | - |
| FB + 1 mm flat bar | 492 | 631 | 0.102 | 0.212 | 0.163 | - |
| Standard deviation | 52 | 36 | 0.013 | 0.018 | 0.023 | - |
| FB flat bar | 514 | 688 | 0.114 | 0.164 | 0.162 | - |
| Standard deviation | 116 | 77 | 0.047 | 0.046 | 0.056 | - |
| Alloy 182 butter flat bar | 347 | 603 | 0.383 | 0.441 | 0.477 | - |
| Standard deviation | 15 | 17 | 0.037 | 0.035 | 0.018 | - |
| Alloy 182 WM flat bar | 375 | 605 | 0.352 | 0.411 | 0.423 | - |
| Standard deviation | 7 | 11 | 0.038 | 0.040 | 0.018 | - |
| Transverse flat bar | 384 | 597 | 0.141 | 0.221 | 0.247 | - |
| Standard deviation | 17 | 8 | 0.025 | 0.021 | 0.016 | - |

The highest elongation values were measured from the Alloy 182 weld metal and the buttering layer. The uniform elongation of the Alloy 182 weld metal is 35 % and the elongation at fracture 47 %. The SA 508 base metal has lower ductility with measured elongation values of 11 % and 29 % of uniform elongation and elongation at fracture. The ductility is at its lowest in the fusion boundary specimens and nearly as low in the SA 508 HAZ specimens, which is expected since those specimens showed the highest strength values. The strain values do not correspond as well between the specimens of different dimensions as the strength values. This is due to the difference in constraint between the flat bar and the round bar specimens.
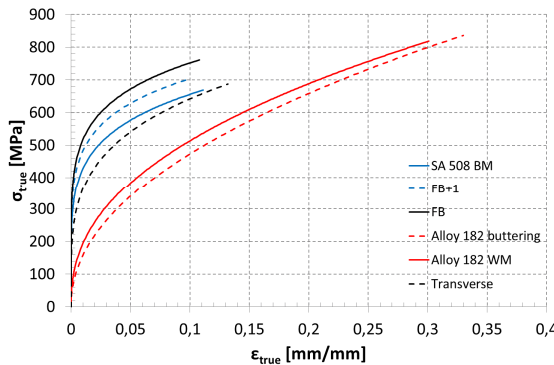


**Figure 4.31.** True stress-strain curves of each BWR-DMW zone according to Hollomon equation using average tensile data.

The strain hardening coefficient of Alloy 182 is significantly higher than that of the other tested weld zones. The lowest strain hardening coefficients, n = 0.162 and n = 0.163, are found from the fusion boundary and SA 508 HAZ. The lower strain hardnening coefficient means that the material is able to strengthen less due to plastic deformation. The strain hardening exponents of the specimens with different geometries correspond well with each other. The tensile properties of the transverse flat-bar specimens are similar to those of the SA 508 BM, HAZ and the FB which suggests that the transverse specimens have likely fractured from the SA 508 side of the fusion boundary.
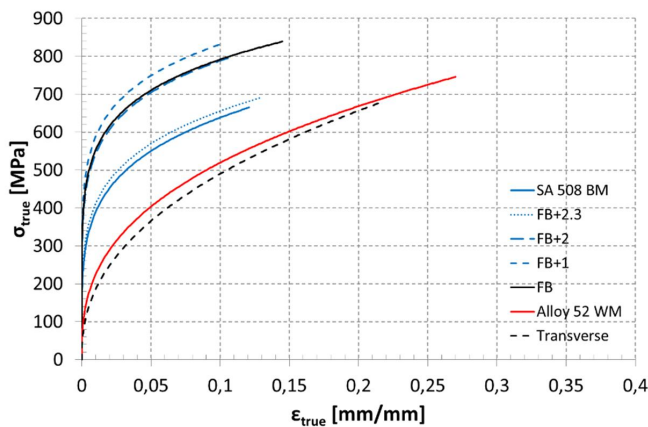
The tensile test results of the NG-DMW specimens are shown in Table 4.2 and Figure 4.32 shows true stress-strain curves of each NG-DMW zone according to Hollomon equation using average tensile data from Table 4.2. The yield and tensile strength values obtained from the round bar specimens are 409 MPa and 582 MPa for the SA 508 base metal and 434 MPa and 650 MPa for the Alloy 52 weld metal. The highest strength values are obtained from the SA 508 HAZ specimens extracted from 1 mm from the fusion boundary. The strength of the SA 508 HAZ and fusion boundary area in general is much higher compared to the strength of the SA 508 base metal or Alloy 52 weld metal. The SA 508 HAZ specimens extracted from 2.3 mm from the fusion boundary show strength values quite close to those of the SA 508 base metal. The strength values of the SA 508 base metal of the specimens with different geometries correspond very well with each other fitting within the standard deviation. The strength values between the round bar and flat-bar Alloy 52 specimens had significantly larger difference in them. It should be noted, however, that the flat-bar results showed quite a significant scatter in the case of Alloy 52 weld metal.

**Table 4.2.** Tensile test results showing the yield strength ($R_{p0.2}$), ultimate tensile strength ($R_m$), uniform elongation ($A_g$), elongation to fracture (A), strain hardening coefficient (n), and Young's modulus (E) of the tested NG-DMW zones.

| Specimen | $R_{p0.2}$ [MPa] | $R_m$ [MPa] | $A_g$ [mm/mm] | A [mm/mm] | n | E [GPa] |
|---|---|---|---|---|---|---|
| SA 508 BM round bar | 409 | 582 | 0.114 | 0.310 | 0.201 | 210 |
| Standard deviation | 9 | 5 | 0.008 | 0.014 | 0.010 | 2 |
| Alloy 52 WM round bar | 434 | 650 | 0.295 | 0.399 | 0.309 | 169 |
| Standard deviation | 35 | 20 | 0.039 | 0.031 | 0.035 | 2 |
| SA 508 BM flat bar | 416 | 580 | 0.129 | 0.235 | 0.215 | - |
| Standard deviation | 14 | 6 | 0.005 | 0.015 | 0.008 | - |
| FB + 2.3 mm flat bar | 453 | 599 | 0.139 | 0.252 | 0.203 | - |
| Standard deviation | 75 | 45 | 0.018 | 0.027 | 0.021 | - |
| FB + 2 mm flat bar | 617 | 711 | 0.112 | 0.203 | 0.162 | - |
| Standard deviation | 49 | 57 | 0.019 | 0.025 | 0.010 | - |
| FB + 1 mm flat bar | 668 | 754 | 0.106 | 0.193 | 0.151 | - |
| Standard deviation | 45 | 46 | 0.011 | 0.013 | 0.010 | - |
| FB flat bar | 643 | 727 | 0.158 | 0.240 | 0.156 | - |
| Standard deviation | 108 | 67 | 0.089 | 0.082 | 0.034 | - |
| Alloy 52 WM flat bar | 384 | 574 | 0.311 | 0.354 | 0.364 | - |
| Standard deviation | 70 | 47 | 0.061 | 0.063 | 0.090 | - |
| Transverse flat bar | 276 | 541 | 0.242 | 0.300 | 0.422 | - |
| Standard deviation | 6 | 7 | 0.015 | 0.026 | 0.007 | - |

The elongation is at its lowest in the SA 508 HAZ specimens extracted from 1 mm and 2 mm from the fusion boundary. The elongation of the SA 508 HAZ specimens extracted from 2.3 mm from the fusion boundary is similar to the elongation of the base metal. Alloy 52 weld metal shows the highest elongation values and, thus, has the highest ductility of the NG-DMW zones. The ductility as well as the strain hardnening exponent of Alloy 52 are, however, clearly lower than the corresponding properties of Alloy 182. The tensile results obtained from the fusion boundary specimen 1 are closer to the tensile results of the weld metal than the other fusion boundary specimens suggesting that the specimen consists of a larger volume of weld metal than the other fusion boundary specimens.

The strain hardening coefficients correspond to each other quite well when taking into account the large scatter within the results of the Alloy 52 flat-bar specimens. Similarly to the BWR-DMW results, the elongation values have a larger difference between the specimens with different dimensions due to the difference in constraint between the specimens with different geometries. The tensile properties of the transverse flat-bar specimens are, in contrast to the BWR-DMW, clearly closer to those of the weld metal than those of the SA 508 specimens. This suggests that the transverse specimens have likely fractured from the Alloy 52 side of the fusion boundary.



**Figure 4.32.** True stress-strain curves of each NG-DMW zone according to Hollomon equation using average tensile data.

## 4.4 Fracture resistance curves

The J-R curves of all BWR-DMW specimens are shown in Figure 4.33. Alloy 182 buttering layer specimens show the highest fracture resistance with the lowest J value at ductile fracture initiation being $J_Q$ = 908 kJ/m² and the lowest J value at 1 mm crack extension being $J_{1mm}$ = 1056 kJ/m². The SA 508 HAZ and the fusion boundary specimens showed very similar fracture resistance with and the lowest $J_Q$ values being $J_Q$ = 161 kJ/m² and $J_Q$ = 232 kJ/m² and the lowest $J_{1mm}$ values being $J_{1mm}$ = 345 kJ/m² and $J_{1mm}$ = 387 kJ/m². The similarity in the fracture resistance can also be seen clearly in the J-R curves. The J-R curves of the

SA 508 HAZ and the fusion boundary specimens are very close to each other and have similar shapes and slopes.
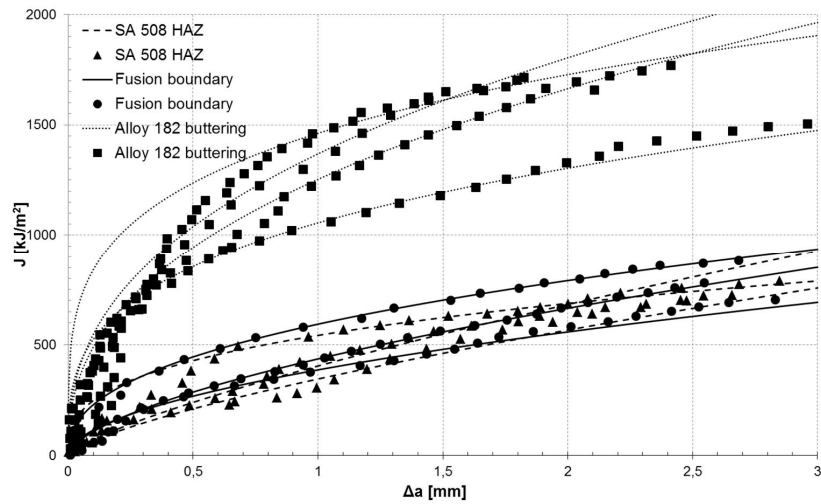


**Figure 4.33.** J-R curves of the BWR-DMW specimens.

Figure 4.34 shows the J-R curves of the different BWR-DMW zones fitted using the J versus crack extension points of all the tested specimens from each zone. Curve fits of each individual zone are presented in Annex C. Alloy 182 buttering clearly has the highest fracture resistance and the steepest J-R curve slope. SA 508 HAZ and the fusion boundary have very similar fracture res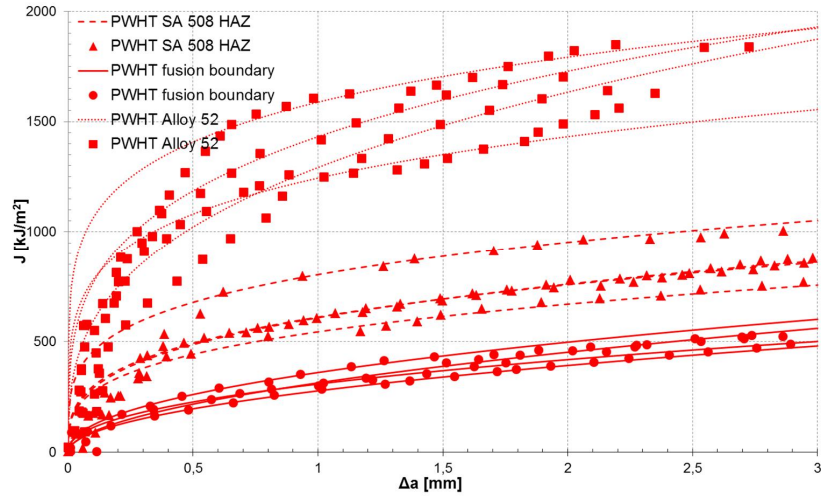istance and the average J-R curves show almost identical fracture resistances and J-R curve slopes. Table 4.3 shows fracture mechanical values of each BWR-DMW zone determined from the average J-R curves shown in Figure 4.34.
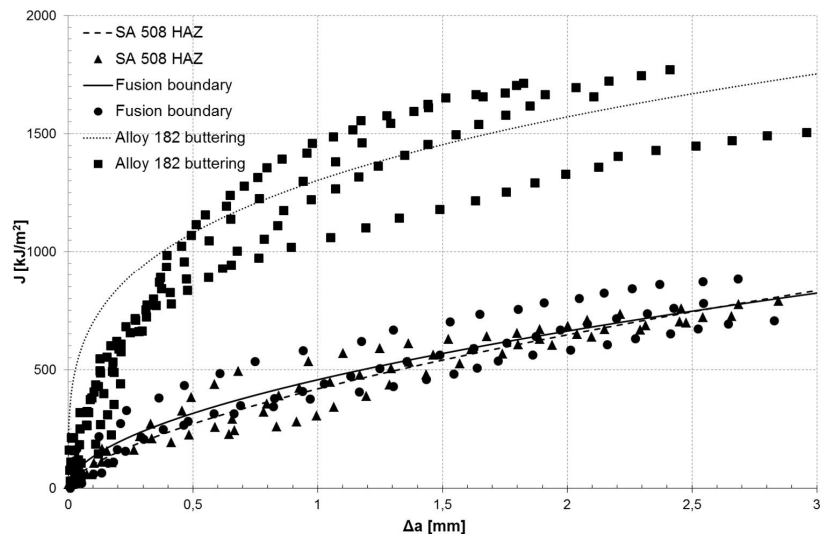


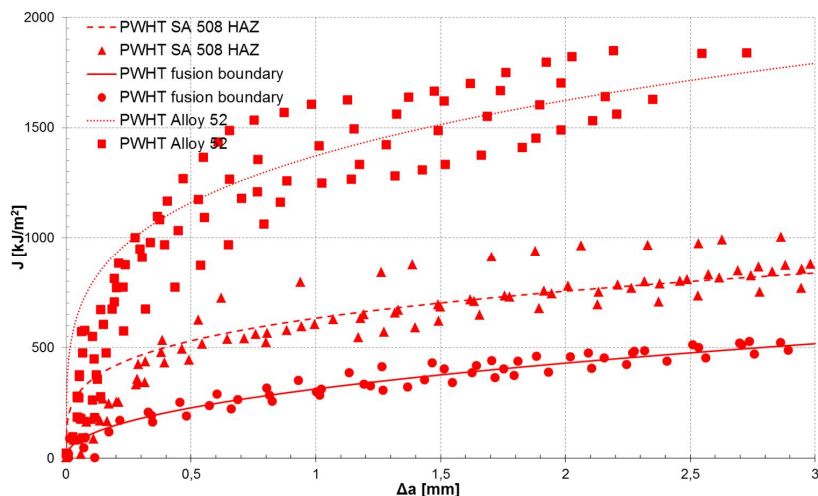**Figure 4.34.** J-R curves fitted using the data of all the specimens from each BWR-DMW zone.

**Table 4.3.** Fracture resistance values determined from the J-R curves of each BWR-DMW zone.

| Weld zone | $J_Q$ [kJ/m²] | $J_{1mm}$ | $C_2$ | M | $\sigma_Y$ [MPa] |
|---|---|---|---|---|---|
| **SA 508 HAZ** | 238 | 419 | 0,63 | 2 | 562 |
| **Fusion boundary** | 290 | 457 | 0,53 | 2 | 601 |
| **Alloy 182 buttering** | 1237 | 1303 | 0,27 | 3.49 | 515 |

The J-R curves of the NG-DMW specimens are shown in Figures 4.35 and 4.36. The Alloy 52 weld metal specimens showed the highest fracture resistance in the as-welded as well as in the PWHT condition with the lowest J values being $J_Q$ = 1126 kJ/m² and $J_{1mm}$ = 1092 kJ/m² for the as-welded Alloy 52 weld metal and $J_Q$ = 1075 kJ/m² and $J_{1mm}$ = 1244 kJ/m² for the PWHT Alloy 52 weld metal. In contrast to the BWR-DMW, the SA 508 HAZ NG-DMW specimens showed clearly higher fracture resistance than the NG-DMW fusion boundary specimens. The lowest J values of the as-welded SA 508 HAZ were $J_Q$ = 489 kJ/m² and $J_{1mm}$ = 729 kJ/m² and the lowest J values of the PWHT condition SA 508 HAZ were $J_Q$ = 434 kJ/m² and $J_{1mm}$ = 544 kJ/m². The lowest J values found from the fusion boundary specimens were $J_Q$ = 344 kJ/m² and $J_{1mm}$ = 503 kJ/m² for the as-welded specimens and $J_Q$ = 145 kJ/m² and $J_{1mm}$ = 277 kJ/m² for the PWHT state specimens.
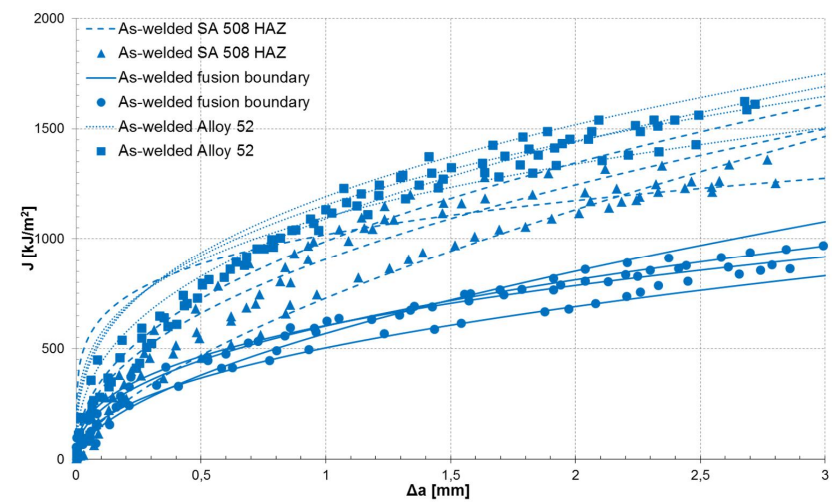


**Figure 4.35.** J-R curves of the as-welded state NG-DMW specimens.

**Figure 4.36.** J-R curves of the PWHT state NG-DMW specimens.

Figures 4.37 and 4.38 show J-R curves of the different NG-DMW zones fitted using the J versus crack extension points of all the tested specimens from each zone and Table 4.4 shows the fracture mechanical values of each NG-DMW zone determined from the average J-R curves. Curve fits of each individual zone are presented in Annex D. Alloy 52 weld metal clearly has the highest fracture resistance and the PWHT seems to increase the fracture resistance of Alloy 52 weld metal. In contrast to the Alloy 52 weld metal, the PWHT decreases the fracture mechanical properties of the SA 508 HAZ and the fusion boundary. In addition to lowering the $J_Q$ and $J_{1mm}$ values, the PWHT also descents the slopes of the J-R curves of the SA 508 HAZ and the fusion boundary.
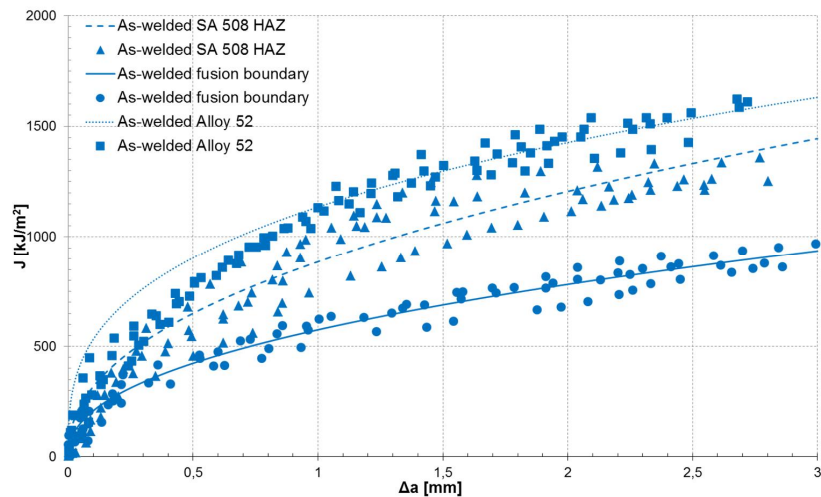


**Figure 4.37.** J-R curves fitted using the data of all the specimens from each as-welded state NG-DMW zone.

**Figure 4.38.** J-R curves fitted using the data of all the specimens from each PWHT state NG-DMW zone.

**Table 4.4.** Average fracture resistance values determined from the average J-R curves of the NG-DMW fracture mechanical specimens presented in Figures 4.37 and 4.38.

| Weld zone | $J_Q$ [kJ/m²] | $J_{1mm}$ | $C_2$ | M | $\sigma_Y$ [MPa] |
|---|---|---|---|---|---|
| As-welded SA 508 HAZ | 754 | 886 | 0,45 | 2 | 711 |
| PWHT SA 508 HAZ | 546 | 633 | 0,25 | 2 | |
| As-welded fusion boundary | 420 | 576 | 0,44 | 2 | 685 |
| PWHT fusion boundary | 187 | 313 | 0,46 | 2 | |
| As-welded Alloy 52 WM | 1204 | 1136 | 0,33 | 2,20 | 542 |
| PWHT Alloy 52 WM | 1284 | 1372 | 0,24 | 4,07 | |

## 4.5 Mismatch determination

The strength mismatch states across the fusion boundaries of the welds have been determined according to the SINTAP procedure from the tensile testing data of the sub-sized specimens. In addition to the mismatch determinated based on strength data, the mismatch states of the different weld zones with respect to the adjacent weld zones and the base metal are also presented based on ductility, strain hardening, Vickers hardness, nanoindentation, and fracture mechanical test data.

### 4.5.1 BWR-DMW

Table 4.5 shows the mismatch factors of the different BWR-DMW zones. The mismatch factors are calculated as ratios to the SA 508 base metal from the 1x2 mm flat-bar tensile test data. Alloy 182 buttering and weld metal are under-matched in strength compared to the base metal. The strength mismatch in the BWR-DMW is at its highest at the fusion boundary. Opposite of the strength mismatch, Alloy 182 buttering and weld metal are significantly overmatched in

elongation and strain hardening coefficient when compared to the SA 508 base metal and the SA 508 HAZ. The smallest elongation value and strain hard-nening coefficient was found from the SA 508 HAZ.

**Table 4.5.** Mismatch factors of the different BWR-DMW zones with respect to the properties of the SA 508 base metal.

| Weld zone | $(R_{p0.2})_i/(R_{p0.2})_{BM}$ | $(R_m)_i/(R_m)_{BM}$ | $(A_g)_i/(A_g)_{BM}$ | $n_i/n_{BM}$ |
|---|---|---|---|---|
| SA 508 Base metal | 1.00 | 1.00 | 1.00 | 1.00 |
| 1 mm from FB into the SA 508 HAZ | 1.18 | 1.07 | 0.87 | 0.88 |
| Fusion boundary | 1.23 | 1.16 | 0.98 | 0.88 |
| Alloy 182 buttering | 0.83 | 1.02 | 3.28 | 2.57 |
| Alloy 182 WM | 0.90 | 1.02 | 3.01 | 2.28 |

Figure 4.39 shows the changes in strength, elongation, and strain hardening mismatches, Vickers hardness, nanohardness, and fracture resistance across the SA 508-Alloy 182 interface of the BWR-DMW. The mismatch factors are presented with respect to the SA 508 base metal $((R_{p0.2})_{BM}, (R_m)_{BM}, (A_g)_{BM}, n_{BM})$, with respect to the preceding weld zone $((R_{p0.2})_{i-1}, (R_m)_{i-1}, (A_g)_{i-1}, n_{i-1})$, and with respect to the subsequent weld zone $((R_{p0.2})_{i+1}, (R_m)_{i+1}, (A_g)_{i+1}, n_{i+1})$.
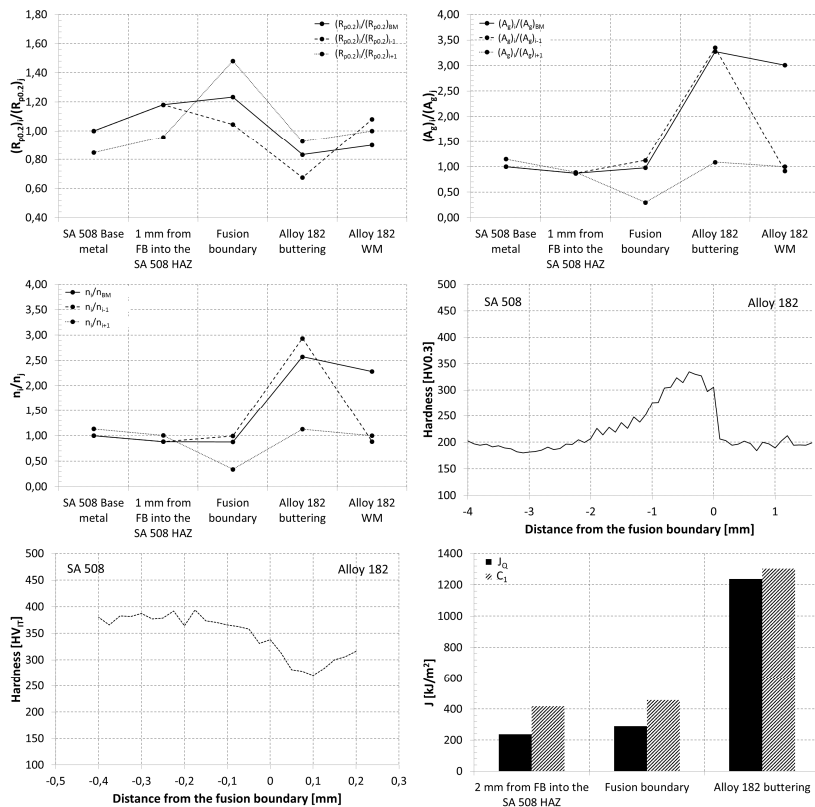


**Figure 4.39.** Change in a) yield strength mismatch, b) uniform elongation mismatch, c) strain hardening coefficient mismatch, d) Vickers hardness, e) nanohardness, and f) fracture resistance across the SA 508-Alloy 182 interface of BWR-DMW.

As can be seen, the strength mismatches and the Vickers hardness profiles show quite similar mismatch behavior. The strength mismatch and hardness increase in the SA 508 HAZ have their maximum values near the fusion boundary, right at the fusion boundary in the case of the strength mismatch and right next to the fusion boundary in the SA 508 HAZ in the case of the hardness. After the fusion boundary in the Alloy 182 buttering, the strength mismatch and hardness drop quite fast to the level of equal or below the base metal. The nanoindentation profile shows the mismatch state in the immediate vicinity of the fusion boundary. According to the nanoindentation profile, there is a drop in hardness immediately at the Alloy 182 side of the fusion boundary. This suggests that the crack propagation would proceed to the Alloy 182 side in a case in which the crack is located in the vicinity of the fusion boundary.

Elongation and strain hardening behave contrarily to the strength and hardness. The elongation and strain hardening coefficient mismatches are at their highest between the fusion boundary and Alloy 182 buttering. As mentioned already, the fusion boundary and the SA 508 HAZ have quite identical fracture resistance and the fracture resistance increases substantially at the Alloy 182 buttering.

### 4.5.2 NG-DMW

Table 4.6 shows the mismatch factors of the different NG-DMW zones. The mismatch factors are calculated as ratios to the SA 508 base metal from the 1x2 mm flat-bar tensile test data. Alloy 52 weld metal is undermatched in strength compared to the base metal. The strength mismatch in the NG-DMW is at its highest at 1 mm from the fusion boundary into the SA 508 HAZ. In contrary to the strength mismatch, Alloy 52 weld metal is overmatched in elongation and strain hardening when compared to the SA 508 base metal and the HAZ. The smallest elongation value and strain hardnening coefficient are found from 1 and 2 mm from the fusion boundary into the SA 508 HAZ, which is the coarse-grained zone of the HAZ.

**Table 4.6.** Mechanical mismatch factors of the different NG-DMW zones.

| Weld zone | $(R_{p0.2})_i/(R_{p0.2})_{BM}$ | $(R_m)_i/(R_m)_{BM}$ | $(A_g)_i/(A_g)_{BM}$ | $n_i/n_{BM}$ |
|---|---|---|---|---|
| SA 508 base metal | 1.00 | 1.00 | 1.00 | 1.00 |
| 2.3 mm from FB into the SA 508 HAZ | 1.09 | 1.03 | 1.07 | 0.94 |
| 2 mm from FB into the SA 508 HAZ | 1.48 | 1.23 | 0.87 | 0.76 |
| 1 mm from FB into the SA 508 HAZ | 1.61 | 1.30 | 0.82 | 0.70 |
| Fusion boundary | 1.55 | 1.25 | 1.22 | 0.73 |
| Alloy 52 weld metal | 0.92 | 0.99 | 2.41 | 1.69 |

Figure 4.40 shows the changes in strength, elongation, and strain hardening mismatches across the SA 508-Alloy 52 interface of the PWHT state NG-DMW. Identically to the BWR-DMW, the mismatch factors are presented with respect to the SA 508 base metal, the preceding weld zone, and the subsequent weld zone. Figure 4.40 also shows micro- and nanohardness profiles and change in fracture resistance across the SA 508-Alloy 52 interface of PWHT state and, in addition, as-welded state NG-DMW.
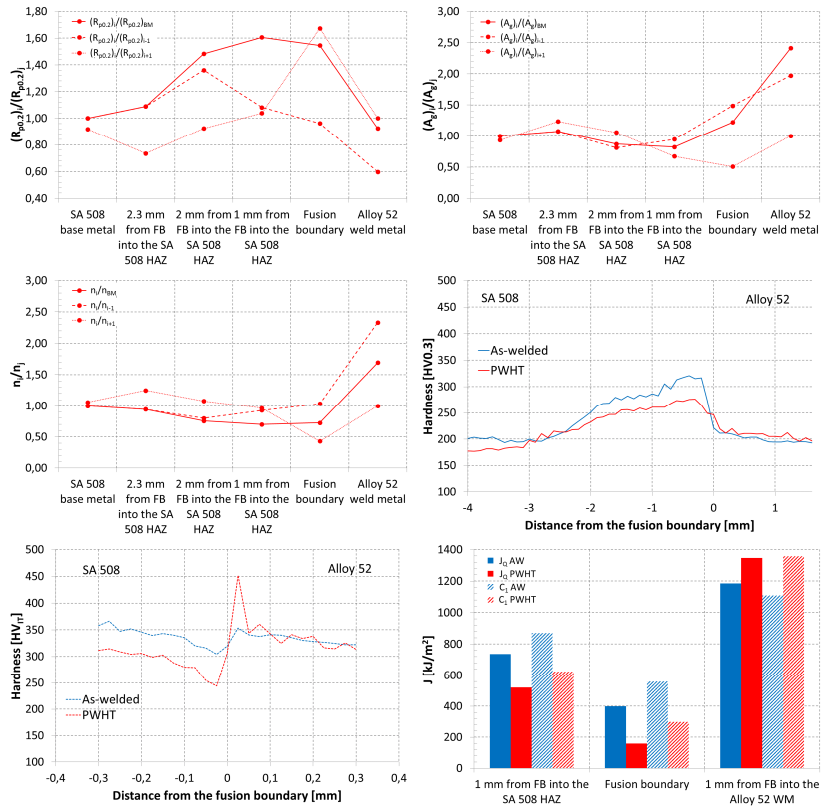
**Figure 4.40.** Change in a) yield strength mismatch, b) uniform elongation mismatch, c) strain hardnening coefficient mismatch, d) Vickers hardness, e) nanohardness, and f) fracture resistance across the SA 508-Alloy 52 interface of NG-DMW.

The strength mismatches and Vickers hardness profiles of the PWHT state interface show similar behavior in the weld zones with strength and hardness increasing in the SA 508 HAZ and decreasing in the Alloy 52 weld metal after the fusion boundary. The strength mismatch is at its highest between the 1 mm SA 508 HAZ specimens and Alloy 52 weld metal specimens. The highest mismatch factor between the weld zones adjacent to each other is the mismatch factor between the fusion boundary and Alloy 52 weld metal.

The nanoindentation profile shows quite significant difference in the near fusion boundary mismatch state of the PWHT state NG-DMW compared to the strength mismatch. According to the nanoindentation profile, in the PWHT state interface the hardness is at its lowest right next to the fusion boundary in the CDZ of SA 508 HAZ and at its highest in the Alloy 52 side right next to the fusion boundary. Thus, the highest hardness mismatch exists between the narrow hard zone in the Alloy 52 side of the fusion boundary and the CDZ in the SA 508 side of the fusion boundary. In addition, the existence of the CDZ creates a low point in hardness in the interface. Therefore, in addition of the CDZ being undermatched with respect to the hardness peak in the Alloy 52 weld metal, the CDZ is also undermatched with respect to the adjacent SA 508 HAZ. Similar behavior can be observed from the nanoindentation profile of the as-welded

state interface. However, in the as-welded state interface, the hardness in the Alloy 52 side of the fusion boundary is significantly lower and the CDZ is narrower and less soft than in the PWHT state interface. Elongation and strain hardening behave contrarily to the strength and hardness and are at their highest between the fusion boundary and Alloy 52 weld metal, Alloy 52 being the overmatched zone. Fracture resistance is at its highest in the Alloy 52 and at its lowest in the fusion boundary in the as-welded as well as in the PWHT condition.

## 4.6 Crack propagation characterization

The fracture surface morphology of the SA 508 HAZ and fusion boundary fracture mechanical specimens was studied using 3D profilometry and all the fracture surfaces were also characterized by FESEM-EDS. The crack propagation paths within the specimens with respect to the microstructures of the weld fusion boundary areas were studied from the cross-section samples prepared from the selected fracture mechanical specimens.

### 4.6.1 SA 508-Alloy 182 interface

Figure 4.41 shows an SEM image of a fracture surface of an Alloy 182 buttering layer specimen. The Alloy 182 buttering layer had significantly higher fracture resistance than the other tested BWR-DMW zones and, thus, the Alloy 182 buttering layer specimens had undergone higher amount of deformation during the fracture mechanical testing than the specimens from the other BWR-DMW zones. The fatigue precracks had grown more uneven in the Alloy 182 buttering layer specimens than in specimens from the other BWR-DMW zones. In addition, the fatigue precracks in the Alloy 182 buttering layer specimens had propagated in an angle of around 45 degrees with respect to the notch orientation. In the specimens from the other weld zones, the fatigue precracks had propagated in a direction parallel to the notch. The fracture surfaces of the Alloy 182 buttering layer specimens consisted of finely dimpled ductile fracture including a small and fine distribution of MnS particles around the fracture surface, example images shown in Figure 4.42.
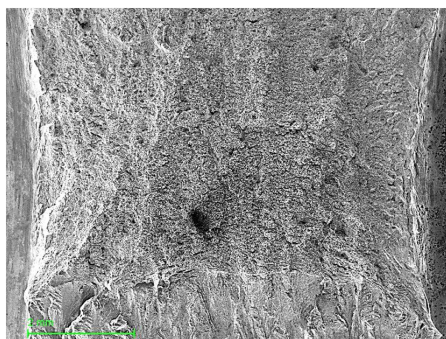


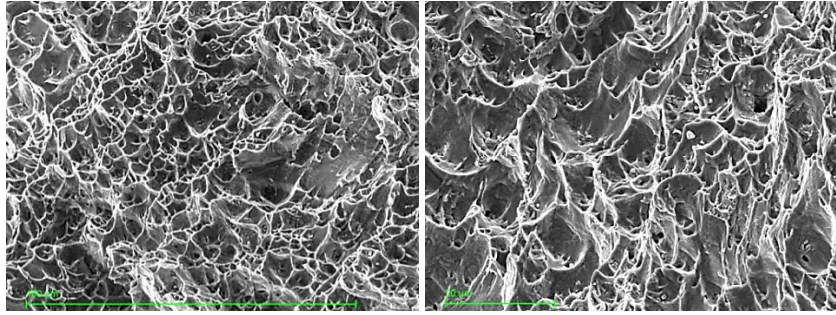**Figure 4.41.** An SEM image of a fracture surface of a typical Alloy 182 buttering layer specimen.

**Figure 4.42.** SEM images showing the ductile fracture surface on the Alloy 182 buttering layer specimens.

Figure 4.43 shows an SEM image and a 3D topography map of a typical fracture surface of a BWR-DMW SA 508 HAZ specimen. The crack propagation in the SA 508 HAZ specimens occurred towards the SA 508 base metal during the J-R testing and the final fracture caused the cracks to propagate towards the fusion boundary. The SA 508 HAZ specimens had undergone clearly less deformation during the testing than the Alloy 182 buttering layer specimens. The fracture surfaces of the SA 508 HAZ specimens consisted of larger dimples and at the bottom of the dimples there were clusters of larger, elongated MnS particles. SEM images of the typical fracture surface characteristics of the SA 508 HAZ specimens are shown in Figure 4.44.
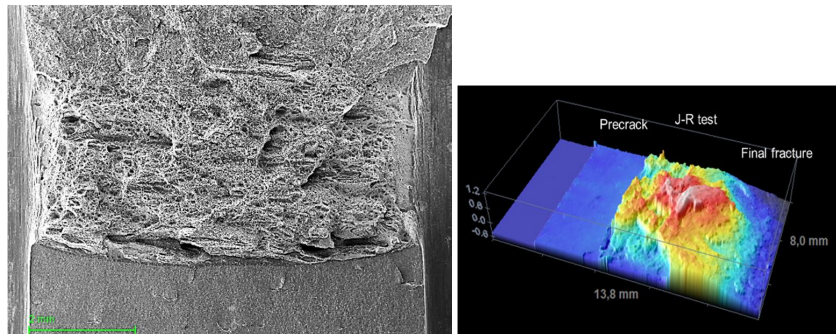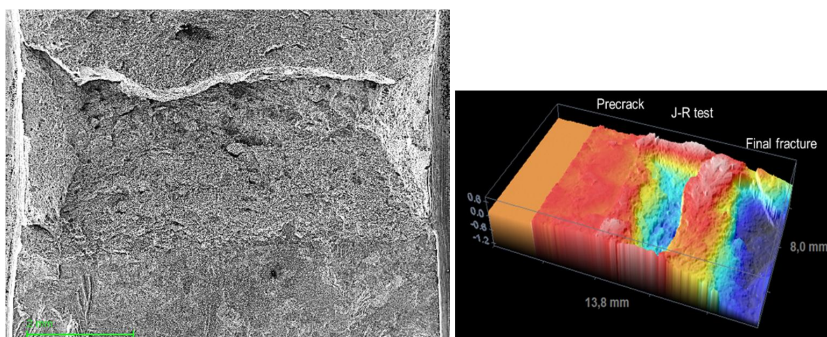


**Figure 4.43.** An SEM image of a fracture surface and a 3D topography map of a typical SA 508 HAZ specimen.
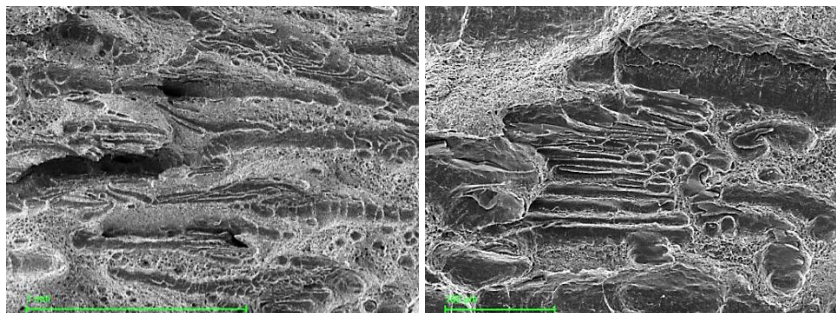


**Figure 4.44.** SEM images showing the ductile fracture surface with the elongated MnS particles found from the SA 508 HAZ specimens.

Figure 4.45 shows an SEM image and a 3D topography map of a typical fracture surface of a BWR-DMW fusion boundary specimen. In all the fusion boundary specimens, the crack propagation occurred towards the Alloy 182 buttering during the J-R testing and the cracks propagation turned towards the SA 508 base metal during the final fracture. The fusion boundary specimens had been able to deform clearly less during the fracture mechanical testing compared to the Alloy 182 buttering layer specimens, which is expected since the tearing resistance of the fusion boundary specimens was substantially lower than the tearing resistance of the Alloy 182 buttering layer specimens.

The fracture surfaces of the fusion boundary specimens had similar MnS distributions as the Alloy 182 buttering layer specimens. Figure 4.46 shows images of the typical fracture surface characteristics observed from the fusion boundary specimens. In the fusion boundary specimens, the final fracture propagated on a different plane. This suggests that during the testing the cracks propagated into the weld metal and when the fracture resistance of the ferritic SA 508 HAZ collapsed due to the lower temperature (final fracture made using liquid nitrogen), the cracks propagated back to the SA 508 side of the fusion boundary.



**Figure 4.45.** An SEM image of a fracture surface and a 3D topography map of a typical fusion boundary specimen.
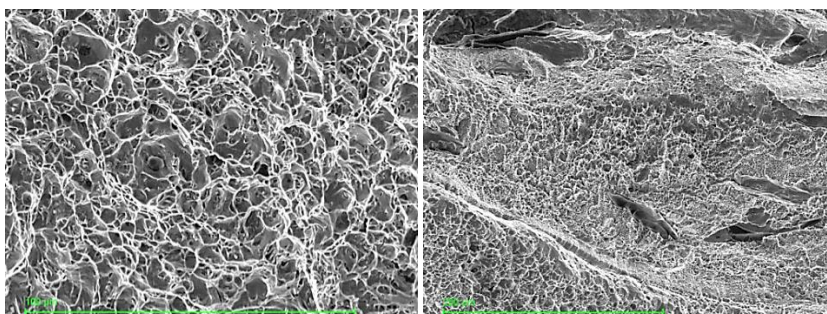


**Figure 4.46.** SEM images showing the ductile fracture surface on the BWR-DMW fusion boundary specimens.

Figure 4.47 shows an SEM image of a cross-section of a BWR-DMW fusion boundary specimen showing the crack propagation in the fusion boundary region. At the beginning of the testing, the exact location of the tip of the fatigue precrack was either in the Alloy 182 buttering side of the fusion boundary or in

the SA 508 HAZ side of the fusion boundary. Regardless of the location of the fatigue precrack with respect to the fusion boundary, the cracks have propagated to the Alloy 182 side of the fusion boundary and the propagation has continued in the Alloy 182 side until the end of the test.
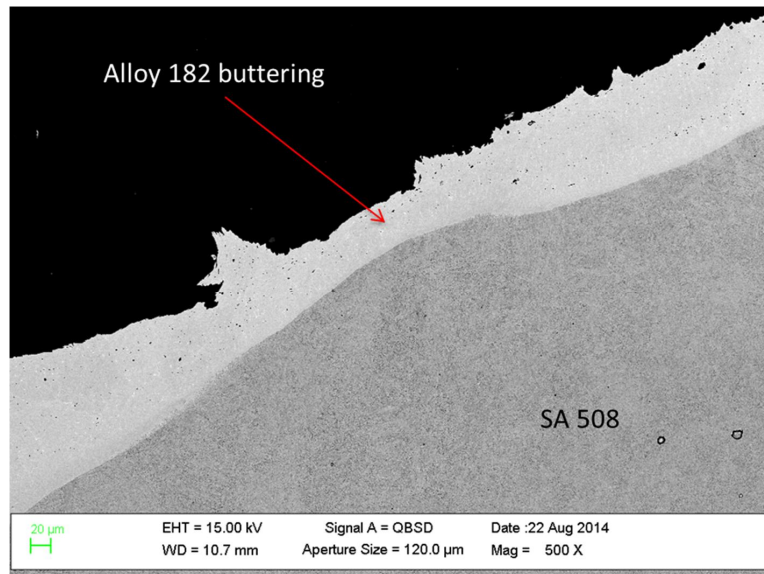


**Figure 4.47.** SEM image showing the crack propagation in the Alloy 182 buttering side of the fusion boundary in the BWR-DMW.

### 4.6.2 SA 508-Alloy 52 interface

Figure 4.48 shows SEM images of fracture surfaces of Alloy 52 weld metal specimens of as-welded and PWHT states. Fracture surfaces of the weld metal specimens showed higher amount of deformation than specimens from the other weld zones and the fracture surfaces were ductile. The fracture resistance of the Alloy 52 weld metal specimens was very high all around.
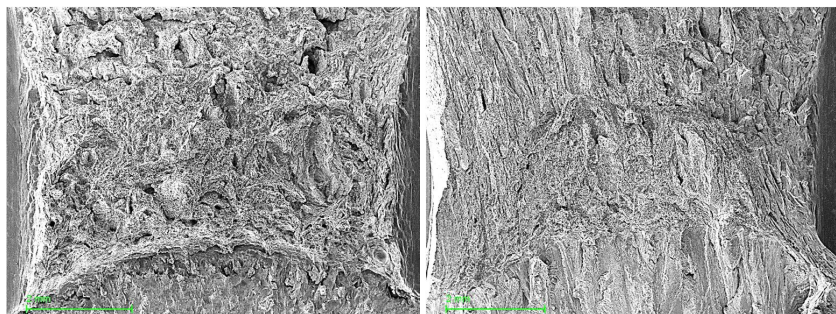


**Figure 4.48.** SEM images showing the fracture surfaces of as-welded (left) and PWHT (right) state Alloy 52 weld metal specimens.

Similarly to the Alloy 182 buttering specimens in the BWR-DMW, the fatigue precracks had grown more uneven in the Alloy 52 weld metal specimens than in

specimens from the other NG-DMW zones. The fatigue precracks in the Alloy 52 weld metal specimens had also propagated in an angle of around 30 to 45 degrees with respect to the notch orientation. In the specimens from the other weld zones, the fatigue precracks had propagated in a direction parallel to the notch. Figure 4.49 presents SEM images showing typical ductile fracture surface found from the fracture surfaces of Alloy 52 weld metal specimens. The crack propagation in the Alloy 52 weld metal specimens of both states has occurred away from the fusion boundary towards the Alloy 52 weld metal throughout the whole test.
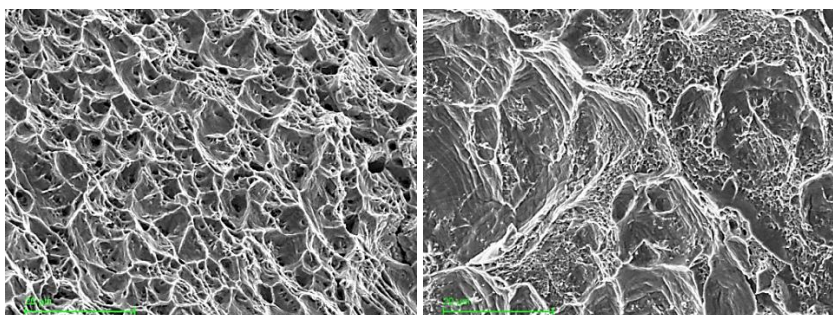


**Figure 4.49.** SEM images showing the ductile fracture surface found from the fracture surfaces of the Alloy 52 weld metal specimens.

Figures 4.50 and 4.51 show SEM images and 3D topography maps of typical fracture surfaces of NG-DMW SA 508 HAZ specimen of as-welded and PWHT states, respectively. At the start of the test, the crack propagation in the NG-DMW SA 508 HAZ specimens has occurred towards the Alloy 52 weld metal during the fracture mechanical testing with the exception of one as-welded state specimen in which the crack propagation has occurred towards the SA 508 base metal. Once the crack has reached the fusion boundary region, the crack propagation has continued along the fusion boundary in the CDZ of the SA 508 HAZ throughout the test. The only exeption to this was one as-welded state specimen in which the crack propagation has occurred away from the fusion boundary towards the SA 508 base metal. This is due to the exact location of the fatigue pre-crack tip, which in this particular specimen has been farther away from the fusion boundary than in the other SA 508 HAZ specimens. Thus, the mismatch state with respect to the exact precrack tip location has been different in this specimen and that has caused the crack propagation to occur to the opposite direction with respect to the other specimens.

In the as-welded state specimens, the crack has made occasional steps to the Alloy 52 side of the fusion boundary and back to the CDZ of the SA 508 HAZ. In addition, the crack propagation from the tip of the fatigue precrack to the location in which the crack has reached a plateau seems to have occurred within a shorter distance in the PWHT state specimens than in the as-welded state specimens. The fracture surfaces of the SA 508 HAZ specimens showed only ductile fracture.
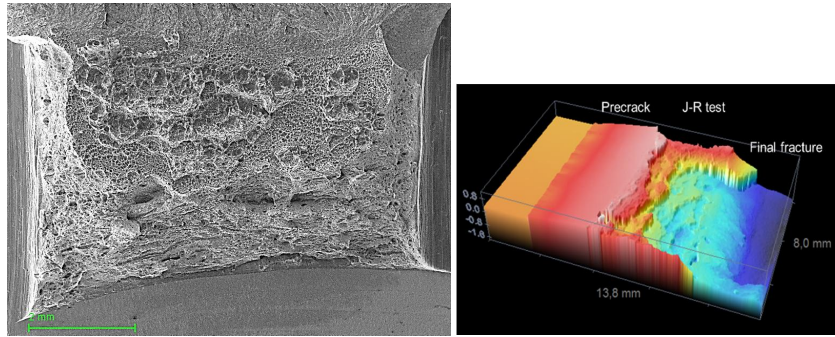
**Figure 4.50.** An SEM image of a fracture surface and a 3D topography map of a typical as-welded state SA 508 HAZ specimen.
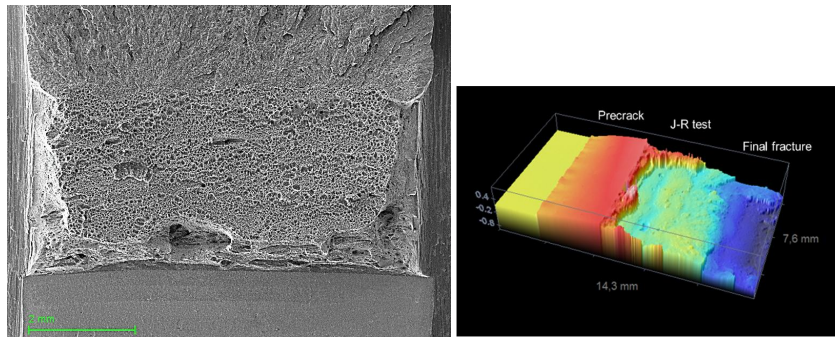


**Figure 4.51.** An SEM image of a fracture surface and a 3D topography map of a typical PWHT state SA 508 HAZ specimen.
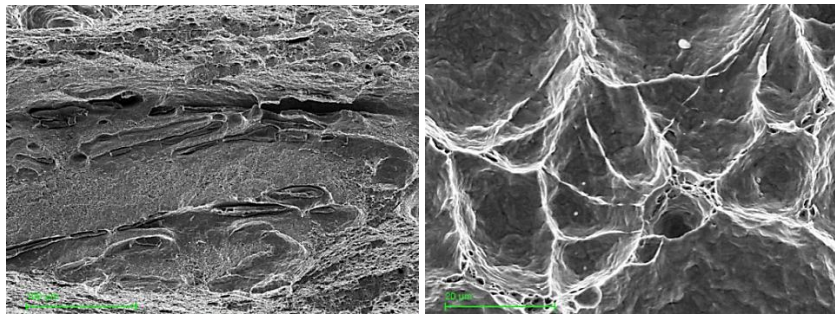


**Figure 4.52.** SEM images showing the larger ductile dimples with the elongated MnS particles and the smaller ductile dimples with the small MnS particles found from the fracture surfaces of the SA 508 HAZ specimens.

Figure 4.52 shows typical fracture surface characteristics found from the SA 508 HAZ specimens. At the beginning of the fracture mechanical test, when the crack propagation has occurred at a distance from the fusion boundary in the SA 508 HAZ, the fracture surfaces of NG-DMW SA 508 HAZ specimens contain larger dimples and in the bottom of these dimples there are clusters of larger, elongated MnS inclusions. When the crack propagation has achieved the fusion boundary, the fracture surface shows characteristics similar to those of the fusion boundary specimens. The fracture surfaces of the PWHT specimens contain very finely distributed small dimples with a small, micron-size MnS particle

in the bottom of the each dimple. The fracture surfaces of the as-welded state specimens contain finely distributed small dimples and larger dimples with large porous-like structures in the bottom of them.

Figures 4.53 and 4.54 show SEM images and 3D topography maps of typical fracture surfaces of NG-DMW fusion boundary specimen of as-welded and PWHT states, respectively. In all the fusion boundary specimens, the crack has found a propagation plane immediately at the start of the test. The fracture surfaces of the PWHT fusion boundary specimens appear quite flat and smoooth whereas in the case of the as-welded specimens, the crack has made occasional jumps back and forth across the the plane of propagation.
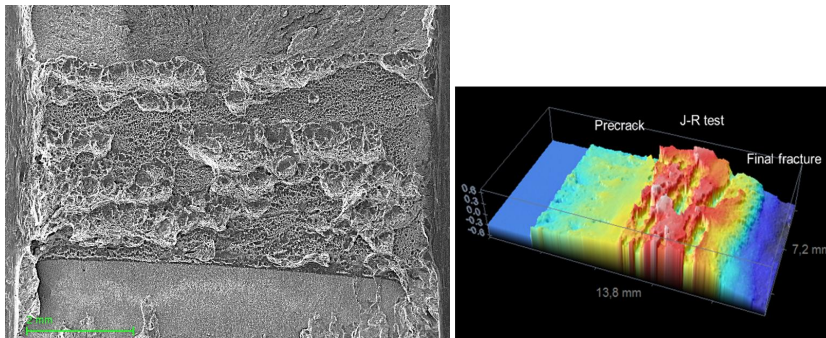


**Figure 4.53.** An SEM image of a fracture surface and a 3D topography map of a typical as-welded state fusion boundary specimen.
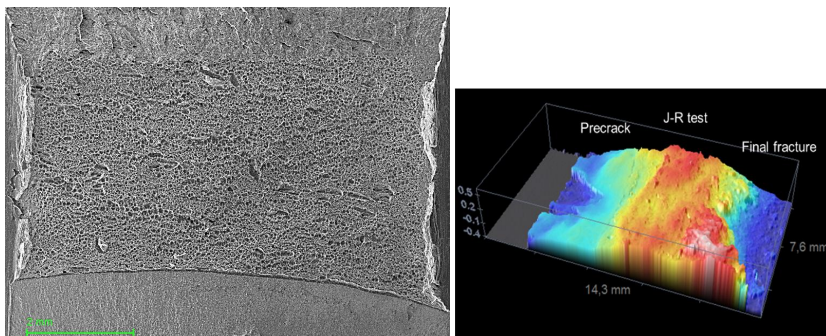


**Figure 4.54.** An SEM image of a fracture surface and a 3D topography map of a typical PWHT state fusion boundary specimen.

In specimens of both heat treatment conditions, the cracks have continued to propagate near the fusion boundary and the specimens have not been able to deform nearly as much as the Alloy 52 weld metal specimens. However, the fracture surfaces are clearly very different. The fracture surface of the PWHT state specimens contains a distribution of very small dimples, whereas the fracture surface of the as-welded state specimens also contains clusters of larger dimples.

Figure 4.55 shows typical fracture surface characteristics found from the fusion boundary specimens. The fracture surfaces of the PWHT specimens contain very finely distributed small dimples with a small, micron-size MnS particle

in the bottom of the each dimple. The fracture surfaces of the as-welded state specimens contain finely distributed small dimples and larger dimples with large porous-like structures in the bottom of them. The porous-like structures, which are likely weld defects, have initiated a dimple formation in the weld metal and caused the crack to make a step across the fusion boundary into the Alloy 52 weld metal and then back to the CDZ of SA 508 HAZ. Unlike in the as-welded specimens, the cracks in the PWHT specimens do not step across the fusion boundary.
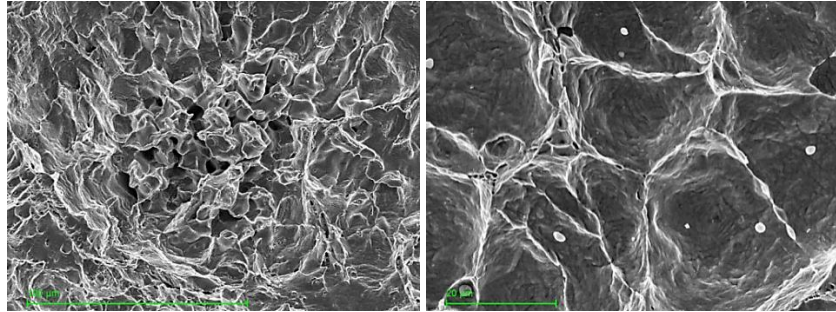


**Figure 4.55.** SEM images showing the porous weld defects and the small ductile dimples with the micron-size MnS particles found from the fracture surfaces of the fusion boundary specimens.

Figures 4.56 and 4.57 show SEM images of cross-sections of NG-DMW fusion boundary specimen of as-welded and PWHT states showing the crack propagation in the fusion boundary region. If the fatigue precrack tip has been away from the CDZ of SA 508 HAZ at the beginning of the test, the crack has immediately jumped to the CDZ of SA 508 HAZ and the crack propagation has continued along the fusion boundary in the CDZ of the SA 508 HAZ throughout the whole test in the specimens of both heat treatment conditions. As mentioned earlier, the reasons for the steps in the crack propagation in the as-welded specimens are the porous-like weld defects, which have initiated a dimple formation in the weld metal and caused the crack to jump across the fusion boundary into the Alloy 52 weld metal and then back to the CDZ of SA 508 HAZ. In the as-welded state specimens, the cracks have made occasional steps to the Alloy 52 side of the fusion boundary and in the PWHT state specimens the crack has propagated in the CDZ of SA 508 throughout the test.
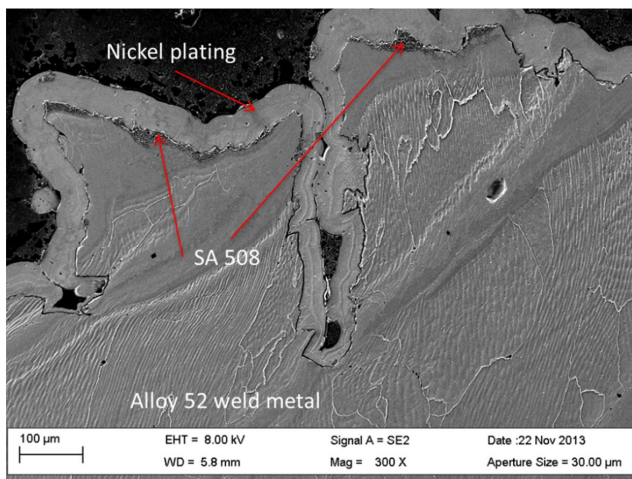
**Figure 4.56.** SEM image showing the crack propagation in the CDZ of SA 508 HAZ side of the fusion boundary in the as-welded state NG-DMW.
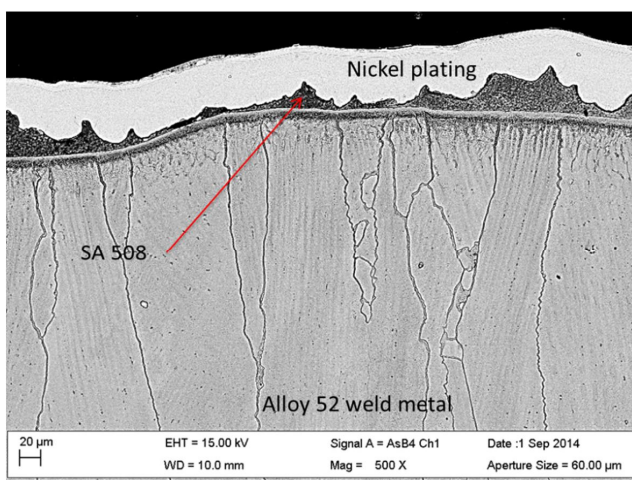


**Figure 4.57.** SEM image showing the crack propagation in the CDZ of SA 508 HAZ side of the fusion boundary in the PWHT state NG-DMW.

# 5 Discussion

The traditional approach of dealing with the effects of mechanical mismatch in welds has been to calculate the ratio of the yield strengths between the weld metal and the base metal, a value known as yield strength mismatch factor M, and assess the effects of mechanical mismatch on structural integrity of the weld based on the of ratio of yield strengths. The yield strength mismatch factors determined across the ferritic-austenitic interfaces of the studied dissimilar metal welds are presented in Figure 5.1. The yield strength mismatch factor has been developed and used for similar metal welds. However, in the case of ferritic-austenitic dissimilar metal welds, the situation is more complicated due to a number of reasons caused mostly by the differing crystallographic properties across the weld fusion boundary. From the fracture mechanical and, thus, the structural integrity point of view, one of the most important aspects regarding the mismatch in dissimilar metal welds is the mechanical mismatch between the microstructural zones adjacent to each other.
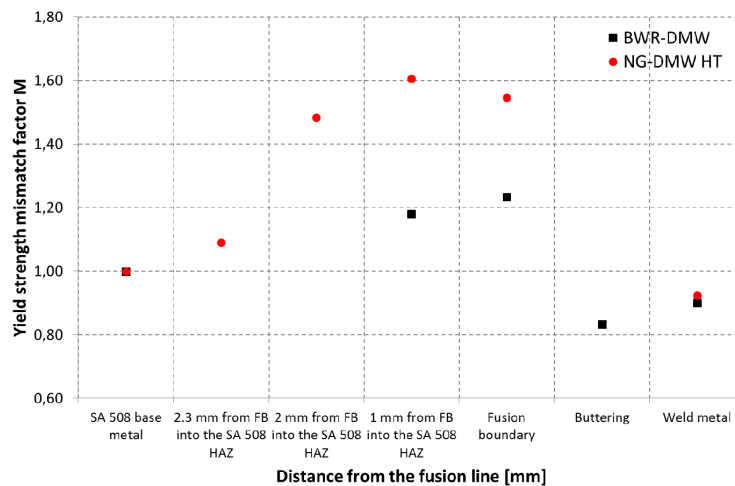


**Figure 5.1.** Change in the yield strength mismatch factor, M, across the ferritic-austenitic interface of the studied DMWs.

In the dissimilar metal welds, the crystallographic differences between the weld metal and the base metals induce a formation of narrow, local zones with distinct microstructural and mechanical properties near the fusion boundary of the weld. These zones may have significantly varying mechanical properties causing the weld to have significant mechanical mismatches between the narrow zones

near the fusion boundary. Thus, the traditional strength mismatch factor approach may not describe the mismatch situation in dissimilar metal welds nearly as well as in similar metal welds due to the significantly small width of the local softer and harder zones near the fusion boundary. Due to the narrowness of these zones, the mechanical properties and mismatches determined using tensile testing may not take into account these zones because of large sample size of even a small-sized tensile testing specimen.

Figure 5.2 shows the change in hardness across the ferritic-austenitic interfaces of the studied dissimilar metal welds measured with an indentation load of 300 g and a step size of 0.1 mm between the indentations. Figure 5.3 shows the change in hardness across the ferritic-austenitic interfaces of the studied dissimilar metal welds measured using an indentation load of 15 mN and a step size of 25 µm. As clearly seen in the hardness profiles measured using the 300 g indentation load, the hardness across the different weld zones behaves similarly to the yield strength if the indentation load is reasonably high and, thus, the hardness has a tendency of averaging the microstructural features more. However, if the hardness measurement is performed using a smaller indentation load and, therefore, the hardness averages the microstructural features less and the hardness profile has a better resolution, the mechanical features of the narrow microstructural zones near the fusion boundary, which may not be revealed by the tensile testing, may be revealed by the hardness measurement.
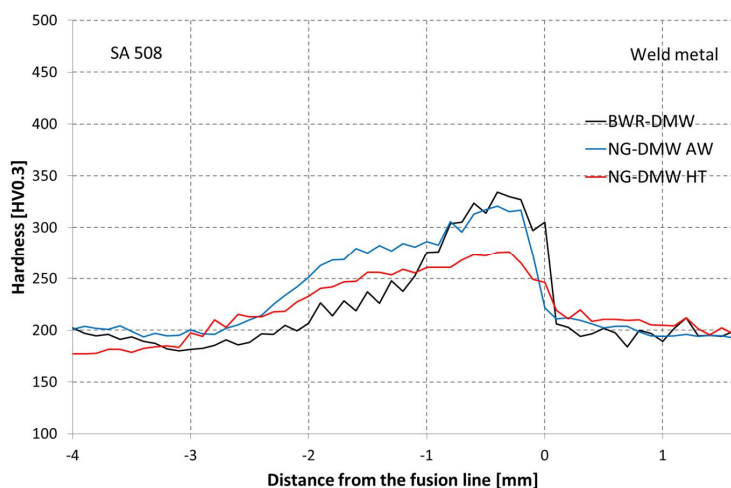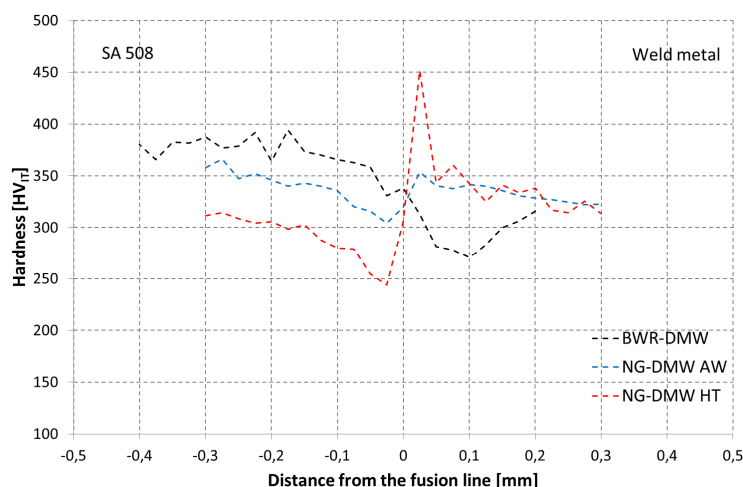


**Figure 5.2.** Change in hardness across the ferritic-austenitic interface of the studied DMWs measured using a microindenter with an indentation load of 300 g and a step size of 0.1 mm.

The diffenrences in the measurement techniques' ability of revealing the local mechanical mismatches created by the existence of narrow microstructural zones in the vicinities of the fusion boundaries of dissimilar metal welds is clearly illustrated in Figures 5.1, 5.2, and 5.3. In the BWR-DMW, where the CDZ or the carbon pile-up were not present in the immediate vicinity of the fusion boundary, all the different measurement techniques, tensile testing, Vickers

hardness testing, and nanoindentation testing, provided similar results regarding the strength or hardness mismatch state across the ferritic-austenitic interface of the weld. According to each measurement technique, the Alloy 182 weld metal is undermatched compared to the SA 508 HAZ side of the fusion boundary and the crack propagation near the fusion boundary occurs towards the Alloy 182 weld metal. This observation excludes the existence of the martensitic zone next to the fusion line due to the fact that the martensitic zone is discontinuous and, hence, does not affect the mismatch state throughout the whole ferritic-austenitic interface.



**Figure 5.3.** Change in hardness across the ferritic-austenitic interface of the studied DMWs measured using a nanoindenter with an indentation load of 15 mN and a step size of 25 μm.

In the case of the NG-DMW, on the other hand, there were a couple of local, significantly narrow zones with distinct microstructural characteristics, i.e. the CDZ in the SA 508 HAZ side and the carbon pile-up in the Alloy 52 side of the fusion boundary, present in the vicinity the fusion boundary. This results in difference in the mismatch state depending on whether the mismatch state is defined by the tensile testing, Vickers hardness measurement, or nanoindentation measurement. According to the tensile testing and the Vickers hardness measurement results, the Alloy 52 weld metal is undermatched compared to the SA 508 HAZ and the crack propagation occurs towards the Alloy 52 weld metal. Nanoindentation, on the other hand, shows a significantly different mechanical mismatch in the immediate vicinity of the fusion boundary and according to the nanoindentation, the mismatch state is at its highest in between the CDZ and the carbon pile-up in the immediate vicinity of the fusion boundary. Hence, the crack propagation occurs the CDZ of the SA 508 HAZ instead of occuring towards the Alloy 52 weld metal.

In assessing the effect of mechanical mismatch on the fracture mechanical properties and the structural integrity of the dissimilar metal welds, the crack propagation examination in comparison with the microstructure in the weld zones becomes significantly important. The crack propagation through specific

weld zones depends on the microstructural and mechanical mismatch between the different weld zones. As predicted by the mismatch states acquired from the nanoindentation measurements, the crack propagation occurs toward and in the Alloy 182 weld metal in the BWR-DMW and toward and in the CDZ of the SA 508 HAZ in the NG-DMW. There is also a difference between the crack propagation in the NG-DMWs of different states. In the PWHT state NG-DMW, the cracks do not step across the fusion boundary but propagate at the CDZ of the SA 508 HAZ at a distance of around less than ten to a few tens of microns from the fusion boundary. In the as-welded state NG-DMW, the crack propagation occurs even closer to the fusion boundary in the CDZ of SA 508 HAZ. However, the crack makes occasional jumps across the fusion boundary into the Alloy 52 weld metal and back. This difference in the crack propagation behavior is due to the wider and softer CDZ in the SA 508 HAZ of the PWHT state NG-DMW caused by the increased carbon migration due to the post-weld heat treatment.

The effect of mechanical mismatch on the fracture mechanical behavior is noticeable in the fracture resistance of the different weld zones. Figure 5.4 shows the J-R curves determined from the fusion boundary specimens of the studied welds. When the crack tip was in the vicinity of the fusion boundary area, the fracture resistance seemed to correspond to the hardness of the zone it propagated in during the fracture mechanical testing.
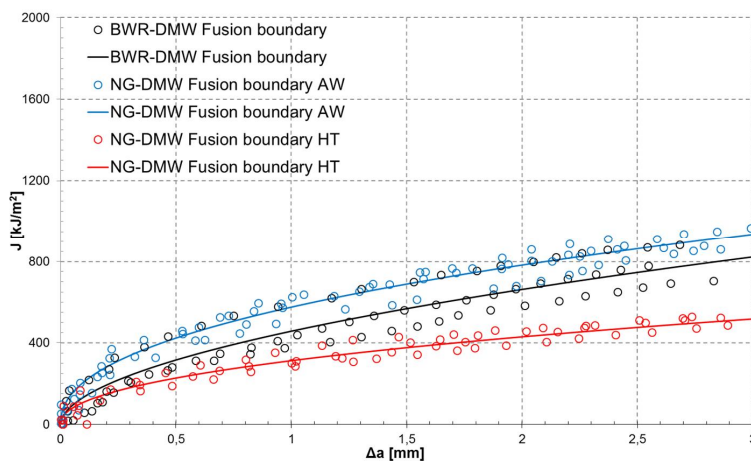


**Figure 5.4.** J-R curves showing the fracture resistances of the fusion boundary specimens of the studied dissimilar metal welds.

In the NG-DMW, the crack propagation occurred mainly in the soft CDZ of the SA 508 HAZ, whereas in the BWR-DMW the crack propagation occurred in the softer Alloy 182 side of the fusion boundary. Out of these zones, the CDZ of the PWHT NG-DMW showed the lowest hardness, the highest mismatch state, and, consequently, the lowest fracture resistance. The CDZ of the as-welded NG-DMW, on the other hand, showed the highest hardness and, simultaneously, the highest fracture resistance. Similarly to the PWHT NG-DMW, there was a thin zone with higher hardness present in the Alloy 52 side of the fusion boundary in

the as-welded NG-DMW. However, the effect of this zone to the crack propagation behavior in the fusion boundary area seemed to be quite negligible, since the crack was able to make occasional steps back and forth the fusion boundary during the fracture mechanical testing. The discontinuous martensitic zone present in the fusion boundary region of each weld was not able to arrest the cracks from propagating to the softer side of the fusion boundary, nor was there any signs of cleavage or quasi-cleavage fracture caused by the existence of the martensitic zone either.

The effect of the existence of the local microstructural zones with distinct mechanical properties on the fracture mechanical behavior of the ferritic-austenitic interfaces of the studied welds is clearly observable in the J-R curves of the SA 508 HAZ specimens shown in Figure 5.5. The NG-DMW SA 508 HAZ specimens were extracted 1 mm from the fusion boundary, whereas the BWR-DMW specimens were extracted 2 mm from the fusion boundary. The SA 508 HAZ at a distance of 1 mm from the fusion boundary is significantly harder and has higher strength than at 2 mm from the fusion boundary. The difference in hardness and strength has a remarkable effect on the fracture resistance behavior of the different HAZ regions. The BWR-DMW SA 508 HAZ specimens show clearly lower fracture resistance than the NG-DMW SA 508 HAZ specimens, which have been extracted from a HAZ region with remarkably higher hardness.
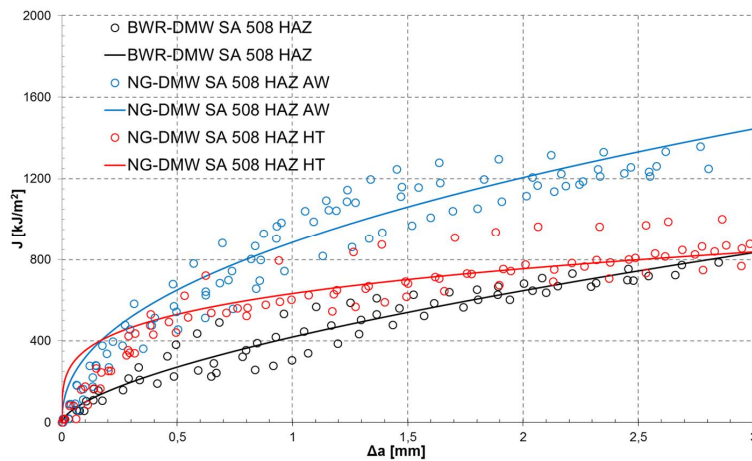


**Figure 5.5.** J-R curves showing the fracture resistances of the fusion boundary specimens of the studied dissimilar metal welds.

On the other hand, the SA 508 HAZ specimens of the PWHT state NG-DMW show clearly lower J-R curve slope compared to the other SA 508 HAZ specimens. This means that the SA 508 HAZ CDZ of the PWHT state NG-DMW exhibits more limited tearing resistance behavior compared to the crack propagation zones of the other studied DMWs. The more limited tearing resistance behavior is at least partially caused by the lower hardness and strength of the particular microstructural zone compared to the corresponding zones of the other studied DMWs.

Predicting the remaining lifetime of NPP main components and structures is very important and, since the SCC field failures of LWR pressure boundary components have caused significant amounts of forced outages, much effort has been made to understand the underlying mechanisms of SCC in the LWR components and structures (Hänninen 2003, Xue et al. 2009). Traditional prediction approach to SCC growth rate is based on linear-elastic fracture mechanics and obtaining the data of the relation of SCC growth rate and the stress intensity factor (Xue et al. 2009). However, evidence and experiments indicate that the materials plasticity also has a great effect on SCC growth rate (Andresen 2002, Andresen et al. 2003, Shoji et al. 2003). Thus, the crack tip stress and strain fields and the elastic-plastic fracture behavior of the different DMW zones are important not only from the mechanical point of view, but also from the environmentally-assisted cracking (EAC) point of view.

# 6 Conclusions

The microstructural, mechanical, and fracture mechanical properties of the ferritic-austenitic interfaces of the DMW mock-ups representing a safe-end nozzle DMW of a traditional BWR pressure vessel design and a modern PWR pressure vessel design were studied. The microstructural characterization revealed HAZ regions typical to LAS welds in both DMWs. A discontinuous Type II boundary and a discontinuous martensitic zone were present in the vicinity of the SA 508-Alloy 182 fusion boundary in the BWR-DMW. The Type II boundary located at approximately 30 to 60 μm from the weld interface into the Alloy 182 and the martensitic zone located in the ferritic SA 508 steel CGHAZ immediately next to the weld interface. A discontinuous martensitic zone was also found from the vicinity of the SA 508-Alloy 52 fusion boundary. In the NG-DMW, there was a CDZ present next to the fusion boundary in the SA 508 HAZ. The PWHT of the NG-DMW resulted in wider and softer CDZ as well as the formation of a carbon-rich zone next to the fusion boundary to the Alloy 52 weld metal side. The presence of the carbon-rich zone is a result of the increased carbon migration during PWHT across the fusion boundary to form a local carbon pile-up in the austenitic Alloy 52 next to the fusion boundary. The CDZ as well as the carbon-rich zone did not exist in the BWR-DMW.

The Vickers hardness measurement showed peak hardnesses in the SA 508 HAZ at approximately 0.5 mm from the fusion boundary in both ferritic-austenitic DMW interfaces. The hardness peaks are caused by the grain-refined microstructure resulting from the high peak temperature and subsequent rapid cooling during the welding process. The hardness peak in the NG-DMW was decreased as a result of the PWHT. The highest strengths and the lowest elongations in the BWR-DMW were measured from the specimens extracted from the fusion boundary. In the NG-DMW, the highest strengths and the lowest elongations were measured from the specimens extracted from the SA 508 grain-refined HAZ at a distance of 1 mm from the fusion boundary.

The strength mismatch states calculated from the tensile testing results corresponded well with the Vickers hardness results measured using 300 g indentation load. In the case of the BWR-DMW, the Alloy 182 buttering layer and weld metal were found to be undermatched in comparison to the SA 508 base metal, the SA 508 HAZ and the fusion boundary area. The highest mismatch between two adjacent zones was found at the weld fusion boundary area between the fusion boundary and the buttering layer specimens. In the NG-DMW, the Alloy 52 weld metal was found undermatched with respect to the other tested weld zones. The highest mismatch in the NG-DMW was also found at the weld fusion

boundary area between the fusion boundary and the Alloy 52 weld metal specimens.

The nanoindentation measurements revealed different characteristics near the fusion boundary region. High hardness mismatch existed in the fusion boundary region of the NG-DMW due to the existence of the soft CDZ next to the fusion boundary in the SA 508 HAZ. The PWHT increased the hardness mismatch in the fusion boundary due to the wider and softer CDZ and the formation of the narrow carbon-rich zone with significantly higher hardness next to the fusion boundary in the Alloy 52 weld metal side. In the case of the BWR-DMW, the nanoindentation measurements revealed a zone with lower hardness next to the fusion boundary in the Alloy 182 side.

The fracture resistance of all the tested zones of both DMWs was high and all the specimens fractured with a ductile mechanism. The Ni-base Alloys 52 and 182 had very high fracture resistance in general. In the BWR-DMW, the fusion boundary and the SA 508 HAZ exhibited fracture resistance quite identical with each other. In the case of the NG-DMW, the SA 508 HAZ exhibited clearly higher fracture resistance than the fusion boundary and the PWHT state fusion boundary specimens had the lowest fracture resistance of all the tested DMW zones. The PWHT increased the fracture resistance of Alloy 52 weld metal and, in contrast, decreased the fracture resistance of the SA 508 HAZ and the fusion boundary. In addition to lowering the separate J values, the PWHT drops the slopes of the J-R curves of the SA 508 HAZ and the fusion boundary.

In the BWR-DMW SA 508 HAZ specimens and in one as-welded state NG-DMW specimen, the crack propagation occurred towards the SA 508 base metal whereas in the other NG-DMW SA 508 HAZ and in the fusion boundary specimens, the crack propagation occurred towards the Alloy 182 buttering/Alloy 52 weld metal. In the BWR-DMW fusion boundary specimens, the crack continued its propagation to the Alloy 182 buttering and in it at a distance of about 100 μm from the SA 508-Alloy 182 interface. In the NG-DMW SA 508 HAZ and fusion boundary specimens, the crack propagation occurred towards the CDZ of the SA 508 HAZ. In the PWHT state specimens, the crack propagated only along the softer CDZ of the SA 508 HAZ, while in the as-welded state specimens, the crack made occasional jumps across the fusion boundary to the Alloy 52 weld metal and back. These jumps were due to the large dimple formation close to the fusion boundary in the Alloy 52 weld metal caused by porous weld defects.

Thereby the crack propagation occurred towards and in the DMW zone with undermatched hardness compared to the surrounding microstructural zones. This is as long as the tip of the precrack was close enough to the softer zone for the mismatch state to affect the crack propagation. This behavior is clearly demonstrated in the SA 508 HAZ specimens. In all the BWR-DMW SA 508 HAZ specimens, in which the tip of the precrack was around 2 mm from the fusion boundary, and in one NG-DMW SA 508 HAZ specimen, in which the tip of the precrack was around 1.6 mm from the fusion boundary, the strength/hardness mismatch caused the crack to propagate towards the SA 508 base metal. In contrast, in all the other NG-DMW SA 508 HAZ specimens, in which the precracks were less than 1.5 mm from the fusion boundary, the crack propagated towards

the softer CDZ next to the fusion boundary due to the strength/hardness mismatch. The crack propagation in the fusion boundary specimens also demonstrates that the crack propagation is influenced by the strength/hardness mismatch state produced by the different microstructural zones in the weld interface. In the NG-DMW, the crack propagation occurred towards and in the softer CDZ, whereas in the BWR-DMW, the crack propagated to the Alloy 182 side of the fusion boundary, where there was the softest zone according to the nanoindentation measurements.

The status of the strength/hardness mismatch affecting the crack propagation behavior was best predicted by the hardness measurements performed using a small enough indentation load which takes into account the local, relatively narrow zones with distinct strength/hardness compared to the surrounding microstructural zones. Due to the narrowness of these zones, the mechanical mismatches determined using tensile testing, even with smaller specimens, did not take into account these zones because of too large sample size of the specimens.

# References

Alexandrov, B.T., Lippold, J.C., Sowards, J.W., Hope, A.T., and Saltzmann, D.R. (2012) Fusion Boundary Microstructure Evolution Associated with Embrittlement of Ni-base Alloy Overlays Applied to Carbon Steel. Welding in the World. Vol. 57. pp. 39-53.

Anderson T.L. (2005) Fracture Mechanics: Fundamentals and Applications, 3rd Edition. Taylor & Francis, Boca Raton, Florida, USA. 621 p. ISBN: 0-8493-1656-1.

Andresen, P.L. (2002) Similarity of Cold Work and Radiation Hardening in Enhancing Yield Strength and SCC Growth of Stainless Steel in Hot Water. NACE. Corrosion 2002. Paper 02509.

Andresen, P.L., Young, L.M., Emigh, P.W., and Horn, R.M. (2002) Stress Corrosion Crack Growth Rate Behavior of Ni Alloys 182 and 600 in High Temperature Water. NACE. Corrosion 2002. Paper 02510.

Andresen, P.L., Emigh, P.W., Morra, M.M., and Horn, R.M. (2003) Effects of Yield Strength, Corrosion Potential, Stress Intensity Factor, Silicon and Grain Boundary Character on the SCC of Stainless Steels. Proceedings of the 11th International Conference on Environmental Degradation of Materials in Nuclear Systems. Stevensson, Washington, USA. 17 p.

Andresen, P.L., and Morra, M.M. (2008) Stress Corrosion Cracking of Stainless Steels and Nickel Alloys in High-Temperature Water. Corrosion the Journal of Science and Engineering. Vol. 64. No. 1. pp. 15-29.

ASTM E384 – 11e1 Standard Test Method for Knoop and Vickers Hardness of Materials. ASTM, Pennsylvania, USA. 43 p.

ASTM E1820 – 99a Standard Test Method for Measurement of Fracture Toughness. ASTM, Pennsylvania, USA. 43 p.

Bhadeshia, H.K.D.H. and Honeycombe, R.W.K. (2006) Steels: Microstructures and Properties, 3rd Edition. Butterworth-Heinemann, Jordan Hill, Oxford, UK. 343 p. ISBN-13: 978-0-750-68084-4.

Biswas, P., Mandal, N.R., Vasu, P., and Padasalag, S.B. (2010) Analysis of Welding Distortion due to Narrow-Gap Welding of Upper Port Plug. Fusion Engineering and Design. Vol. 85. pp. 780-788.

Callister, W.D. and Rethwisch, D.G. (2011) Materials Science and Engineering: an Introduction, 8th Edition. John Wiley & Sons, Inc., Hoboken, New Jersey, USA. 885 p. ISBN: 978-0-470-50586-1.

Celik, A., and Alsaran, A. (1999) Mechanical and Structural Properties of Similar and Dissimilar Steel Joints. Materials Characterization. Vol. 43. pp. 311-318.

Chalmers, B. (1964) Principles of Solidification. John Wiley & Sons, Inc., New York, USA. 319 p. ISBN 13: 9780471143253.

Chen, Z.R., and Lu, Y.H. (2015) TEM Observation of Martensite Layer at the Weld Interface of an A508III to Inconel 82 Dissimilar Metal Joint. Metallurgical and Material Transactions A. Vol. 46A. pp. 5494-5498.

Choi, K.J., Kim, J.J., Lee, B.H., Bahn, C.B., and Kim, J.H. (2012) Effects of Thermal Aging on Microstructures of Low Alloy Steel-Ni Base Alloy Dissimilar Metal Weld Interfaces. Journal of Nuclear Materials. Vol. 441. pp. 493-502.

Chung, W.-C., Huang, J.-Y., Tsay, L.-W., and Chen, C. (2011) Microstructure and Stress Corrosion Cracking Behavior of the Weld Metal in Alloy 52-A508 Dissimilar Welds. Materials Transactions. Vol. 52, No. 1. pp. 12-19.

Danko, J.C. (1987) Corrosion in the Nuclear Power Industry. In: Metal Handbook Volume 13: Corrosion, 9th Edition. ASM International, Metals Park, Ohio, USA. 1415 p. ISBN-13: 978-0871700193.

Davis, J.R. (2000) ASM Speciality Handbook: Nickel, Cobalt, and Their Alloys. ASM, USA. 442 p. ISBN: 0-87170-685-7.

Doi, M., Miki, D., Moritani, T., and Kozakai, T. (2004) Gamma/Gamma-Prime Microstructure Formed by Phase Separation of Gamma-Prime Precipitates in Ni-Al-Ti Alloy. The Minerals, Metals & Materials Society. Superalloys 2004. pp. 109-114.

DuPont, J.N., Robino, C.V., Mader, A.R., Notis, M.R., and Michael, R.J. (1988) Solidification of Nb-Bearing Superalloys: Part I. Reaction Sequences. Metallurgical and Material Transactions A. Vol. 29A. pp. 2785-2796.

DuPont, J.N., and Kusko, C.S. (2007) Techincal Note: Martensite Formation in Austenitic/Ferritic Dissimilar Alloy Welds. Welding Journal. Vol. 86. pp. 51-54.

DuPont, J.N., and Mizia, R.E. (2010) Review of Dissimilar Metal Welding for the NGNP Helical-Coil Steam generator. INL/EXT-10-18459.

Engelhard, G., Habip, L.M., Pellkofer, D., Schmidt, J., and Weber, J. (2000) Optimization of Residual Welding Stresses in Austenitic Steel Piping: Proof-Testing and Numerical Simulation of Welding and Post-Welding Processes. Nuclear Engineering and Design. Vol 198. pp. 141-151.

Faidy, C., Martin, G., Taylor, N., Youtsos, A., Katsareas, D., Keinänen, H., Laukkanen, A., Wintle, J., Sherry, A., Lidbury, D., Safa, N., Cipiere, M. F., Gilles, P., Chapuliot, S., Kaiser, Y., and Lenkey, G. (2004) Assessment of Aged Piping Dissimilar Metal Weld Integrity. ADIMEW Synthesis report. Contract FIKS-CT-2000-00047. European Commission. 45 p.

FITNET FFS - MK8 (2008) FITNET Fitness-for-Service (FFS) Procedure – Volume 1, Revision MK8. Editors: Koçak, M., Webster, S., Janosch, J.J., Ainsworth, R.A., and Koers, R. ISBN: 978-3-940923-00-4.

Francis, J.A., Bhadeshia, H.K.D.H., and Withers, P.J. (2007) Welding Residual Stresses in Ferritic Power Plant Steels. Materials Science and Technology. Vol. 23, No. 9. pp. 1009-1019.

Goldstein, J., Newbury, D., Joy, D., Lyman, C., Echlin, P., Lifshin, E., Sawyer, L., and Michael, J. (2003) Scanning Electron Microscopy and X-Ray Microanalysis, 3rd Edition. Springer Science + Business Media, Inc., New York City, New York, USA. 690 p. ISBN: 0-306-47292-9.

Gooch, T.G. (1977) Welding Martensitic Stainless Steels. TWI Res. Bull. Vol. 18. pp. 343-349.

Hertzberg, R.W. (1996) Deformation and Fracture Mechanics of Engineering Materials, 4th Edition. John Wiley & Sons, Inc., Hoboken, New Jersey, USA. 786 p. ISBN: 978-0-471-01214-6.

Hilkes, J., Neesen, F., and Caballero, S. (2004) Electrodes for Welding 9 % Nickel Steel. Welding Journal. Vol. 83, No. 1. pp. 30-37.

Hollomon, J.H. (1945) Tensile Deformation. Metals Technology. Vol. 12. pp. 268-290.

Holmström, P., Sarikka, T., Brederholm, A., Karjalainen-Roikonen, P., Saukkonen, T., Nevasmaa, P., and Hänninen, H. (2013) Effect of Strength Mismatch on Mechanical Properties of BWR Dissimilar Metal Safe-End Weld. 16th International Conference on Environmental Degradation of Materials in Nuclear Power Systems – water Reactors. Asheville, North Carolina, USA. NACE International. 18 p.

Homma, H., Kanto, Y., Kubo, T., and Tanaka, Y. (1995) Crack Growth Resistance in Bi-Metallic Weldment. International Journal of Pressure Vessels and Piping. Vol. 63. pp. 225-236.

Hou, J., Peng, Q.J., Takeda, Y., Kuniya, J., Shoji, T., Wang, J.Q., Han, E.-H., and Ke, W (2010A) Microstructure and Mechanical Property of the Fusion Boundary Region in an Alloy 182 – Low Alloy Steel Dissimilar Weld Joint. Journal of Material Science. Vol. 45. pp. 5332-5338.

Hou, J., Peng, Q.J., Takeda, Y., Kuniya, J., and Shoji, T. (2010B) Microstructure and Stress Corrosion Cracking of the Fusion Boundary Region in an Alloy 182-A533B Low Alloy Steel Dissimilar Metal Joint. Corrosion Science. Vol. 52. pp. 3949-3954.

Hutchinson, J.W., Mear, M.E., and Rice, J.R. (1987) Crack Paralleling an Interface between Dissimilar Materials. Journal of Applied Mechanics. Vol. 54. pp. 828-832.

Hänninen, H., Aho-Mantila, I., and Törrönen, K. (1987) Environment Sensitive Cracking in Pressure Boundary Materials of Light Water Reactors. International Journal of Pressure Vessels and Piping. Vol. 30. pp. 253-291.

Hänninen, H. (2003) Comprehensive Structural Integrity Volume 6: Stress Corrosion Cracking. Editors-in-Chief: Milne, I., Ritchie, R.O., and Karihaloo, B. Volume Editors: Petit, J., and Scott, P.M. Elsevier Inc., San Diego, California, USA. 412 p. ISBN: 0-08-043749-4.

Hänninen, H., Toivonen, A., Brederholm, A., Saukkonen, T., Ehrnstén, U., and Aaltonen, P. (2007) Environment-Assisted Cracking and Hot Cracking of Ni-Base Alloy Dissimilar Metal Welds. Proceedings of the 13th International Conference on Environmental Degradation of Materials in Nuclear Systems – Water Reactors. Whistler, British Columbia, Canada. 19 p.

Hänninen, H., Brederholm, A., Saukkonen, S., Gripenberg, H., Toivonen, A., Ehrnstén, U., and Aaltonen, P. (2008) Hot Cracking and Environment-Assisted Cracking Susceptibility of Dissimilar Metal Welds. VTT Research Notes 2399. VTT Technical Research Centre of Finland, Espoo, Finland. 177 p.

Hänninen, H., Toivonen, A., Saukkonen, T., Brederholm, A., Aaltonen, P., and Ehrnstén, U. (2009) EAC Crack Initiation in Nickel-Based Dissimilar Metal Welds Using Doped Steam Test. Proceedings of the 14th International Conference on Environmental Degradation of Materials in Nuclear Systems – Water Reactors. Virginia Beach, VA, USA. pp. 333–343.

Hänninen, H., Brederholm, A., Saukkonen, T., Ivanchenko, M., Toivonen, A., Karlsen, W., Ehrnstén, U., and Aaltonen, P. (2011) Environment-Assisted Cracking and Hot Cracking Susceptibility of Nickel-Base Alloy

Weld Metal. VTT Research Notes 2582. VTT Technical Research Centre of Finland, Espoo, Finland. 155 p.

Hänninen, H., Brederholm, A., Sarikka, T., Mouginot, R., Holmström, P., Saukkonen, T., Toivonen, A., Karjalainen-Roikonen, P., Nevasmaa, P., Keinänen, H., Leskelä, E., Ahonen, M., Ehrnsten, U., and Aaltonen, P. (2014) Structural Integrity of Ni-Base Alloy Welds. VTT Technology 175. VTT. Espoo. 257 p.

IAEA (2016) International Atomic Energy Agency (IAEA) Power Reactor Information System (PRIS). URL: https://www.iaea.org/pris/. Referred 30th January 2016.

ISO 6507-1:2005 Metallic Materials – Vickers Hardness Test – Part 1: Test Method. European Committee for Standardization.

Jang, C., Lee, J., Kim, J.S., and Jin, T.E. (2008) Mechanical Property Variation within Inconel 82/182 Dissimilar Metal Weld between Low Alloy Steel and 316 Stainless Steel. International Journal of Pressure Vessels and Piping. Vol. 85. pp. 635-646.

Jiang, F., Zhao, K., and Sun, J. (2003) Evaluation of Interfacial Crack Growth in Bimaterial Metallic Joints Loaded by Symmetric Three-Point Bending. International Journal of Pressure Vessels and Piping. Vol. 80. pp. 129-137.

Jones, R.H. (1987) Stress-Corrosion Cracking. In: Metal Handbook Volume 13: Corrosion, 9th Edition. ASM International, Metals Park, Ohio, USA. 1415 p. ISBN-13: 978-0871700193.

Joly, P., Yescas, M., and Keim, E. (2014) Fracture Toughness in the Ductile-Brittle Transition and Thermal Ageing Behavior of Decarburized Heat Affected Zone of Alloy 52 Dissimilar Metal Welds of Nuclear Components. Proceedings of the ASME-2014 Pressure Vessel and Piping Conference. July 20-24, Anaheim, California, USA.

Karlsen, W. and Pakarinen, J. (2009) TEM Investigation of Cracks in Dissimilar Metal Weld Inconel 182 Following Doped Steam Testing. Research Report VTT-R-05722-09. VTT Technical Research Centre of Finland, Espoo, Finland. 29 p.

Karlsson L. (1995) Welding of Dissimilar Metals. Welding in the World. Vol. 36. P. 125-132.

Keinänen, H., Laukkanen, A., and Nevasmaa, P. (2003) Fracture and Tensile Testing of the 'AD01' Mock-Up (ADIMEW - Work Package 2: Material Characterization). Research Report TUO72-033337. VTT Industrial Systems, Espoo, Finland. 41 p.

Kekkonen, T., Aaltonen, P., and Hänninen, H. (1985) Metallurgical Effects on the Corrosion Resistance of a Low Temperature Sensitized Welded AISI Type 304 Stainless Steel. Corrosion Science. Vol. 25, No. 8. pp. 821-836.

Kilian, R, and Roth, A. (2002) Corrosion Behavior of Reactor Coolant System Materials in Nuclear Power Plants. Materials and Corrosion. Vol. 53. pp. 727-739.

Kim, Y.-J., Koçak, M., Ainsworth, R.A., and Zerbst, U. (2000A) SINTAP Defect Assessment Procedure for Strength Mismatched Structures. Engineering Fracture Mechanics. Vol. 67. pp. 529-546.

Kim, J.W., Lee, K., Kim, J.S., and Byun, T.S. (2009) Local Mechanical Properties of Alloy 82/182 Dissimilar Weld Joint Between SA508 Gr.1a and F316 SS at RT and 320 °C. Journal of Nuclear Materials. Vol. 384. pp. 212-221.

Kiser, S. (1990) Nickel-Alloy Consumable Selection for Severe Service Conditions. Welding Journal. Vol. 69, No. 1. pp. 30-35.

Kou, S. (2003) Weld Metallurgy, 2nd Edition. John Wiley & Sons, Inc., Hoboken, New Jersey, USA. 461 p. ISBN: 0-471-43491-4.

Kuo, T., and Lee, H. (2002) Effects of Filler Metal Composition on Joining Properties of Alloy 690 Weldments. Materials Science and Engineering. Vol. 338. pp 202-212.

Kurdjumov, G. V., and Sachs, G. (1930). Over the Mechanisms of Steel Hardening. Zeitschrift für Physik. Vol.64. pp. 325-343.

Laha, K., Chandravathi, K.S., Bhanu Sankara Rao, K., Mannan, S.L., and Sastry, D.H. (2001) An Assessment of Creep Deformation and Fracture Behavior of 2.25Cr-1Mo Similar and Dissimilar Weld Joints. Metallurgical and Materials Transactions A. Vol. 32A. pp. 115-124.

Laukkanen, A., Nevasmaa, P., Ehrnstén, U. & Rintamaa, R. (2001) Mapping of Characteristic Features of Bimetallic Welds from the Standpoint of Engineering Critical Analysis. Proceedings of the 16th International Conference on Structural Mechanics in Reactor Technology (SMiRT-16); Div. G, Fracture Mech. Washington DC. Eds. Vernon C. Matzen and C.C. David Tung. International Association for Structural Mechanics in Reactor Technology (IASMiRT), USA. Paper #1566. 8 p.

Laukkanen, A., Nevasmaa, P., Ehrnstén, U., and Rintamaa, R. (2007) Characteristics Relevant to Ductile Failure of Bimetallic Welds and Evaluation of Transferability of Fracture Properties. Nuclear Engineering and Design. Vol. 237. pp. 1-15.

Lee, H.T., and Jeng, S.L. (2001) Characteristics of Dissimilar Welding of Alloy 690 to 304L Stainless Steel. Science and Technology of Welding & Joining. Vol. 6. No. 4. pp. 225-234.

Lee, H.T., Jeng, S.L., Yen, C.H., and Kuo, T. (2004) Dissimilar Welding of Nickel-Based Alloy 690 to SUS 304L with Ti Addition. Journal of Nuclear Materials. Vol. 335. No. 1. pp. 59-69.

Lin, G., Meng, X.-G., Cornec, A., and Schwalbe, K.-H. (1999) The Effect of Strength Mis-Match on Mechanical Performance of Weld Joints. International Journal of Fracture. Vol. 96. pp. 37-54.

Lippold, J.C., Clark, W.A.T., and Tumuluru, M. (1992) An Investigation of Weld Metal Interfaces. The Metal Science of Joining. The Metals, Minerals, and Materials Society. Warrendale, Pennsylvania, USA. pp. 141-146.

Lippold, J.C., and Kotecki, D.J. (2005) Welding Metallurgy and Weldability of Stainless Steels. John Wiley & Sons, Inc., Hoboken, New Jersey, USA. 376 p. ISBN: 978-0471-47379-4.

Lippold, J.C., Kiser, S.D., and DuPont, J.N. (2009) Welding Metallurgy and Weldability of Nickel-Base Alloys. John Wiley & Sons, Inc., Hoboken, New Jersey, USA. 440 p. ISBN 978-0-470-08714-5.

Messler, R.W. (1999) Principles of Welding: Processes, Physics, Chemistry, and Metallurgy. John Wiley & Sons, Inc., Hoboken, New Jersey, USA. 662 p. ISBN: 0-471-25376-6.

Moran, P.M., and Shih, C.F. (1998) Crack Growth and Cleavage in Mismatched Welds: a Micromechanics Study Using Cell Model. International Journal of Fracture. Vol. 92. pp. 153-174.

Morra, M., Othon, M., Willis, E., and McCracken, S. (2011) Characterization of Structures and Strains in 52-Type and 152 Welds. Alloy 690/52/152

PWSCC Research Collaboration Meeting. November 29 – December 2, Tampa, Florida, USA. pp. 1-183.

Naffakh, H., Shamanian, M., and Ashrafizadeh, F. (2009) Dissimilar Welding of AISI 310 Austenitic Stainless Steel to Nickel-based Alloy Inconel 657. Journal of Materials Processing Technology. Vol. 209. pp. 3628-3639.

Nelson, J.W. and Lewis, W.J. (1967) Process for Narrow Gap Welding. United States Patent Office. Patent 3328556.

Nelson, T.W., Lippold, J.C., and Mills, M.J. (1999) Nature and Evolution of the Fusion Boundary in Ferritic-Austenitic Dissimilar Weld Metals, Part 1 – Nucleation and Growth. Welding Journal. Vol. 78(10). pp. 329-337.

Nelson, T.W., Lippold, J.C., and Mills, M.J. (2000) Nature and Evolution of the Fusion Boundary in Ferritic-Austenitic Dissimilar Weld Metals – Part 2: On-Cooling Transformations. Welding Journal. Vol. 79(10). pp. 267-277.

Nevasmaa, P., Laukkanen, A., and Ehrnstén, U. (2000) Fracture Resistance and Failure Characteristics of AISI 304/SA508 Bimetallic Weld in Ductile Regime. Proceedings of the 13th European Conference on Fracture – Fracture Mech.: Applications and Challenges (ECF 13). San Sebastian, Spain. ESIS / Eng. Mat. Advisory Services Ltd. Paper No. 1N.49. 8 p.

Neves, J. and Loureiro, A. (2004) Fracture Toughness of Welds – Effect of Brittle Zones and Strength Mismatch. Journal of Materials Processing Technology. Vol. 153-154. pp. 537-543.

Northern Arizona University (2016) Electron Microprobe Laboratory website. URL: http://nau.edu/cefns/labs/electron-microprobe/glg-510-class-notes/signals/. Referred February 12th 2016.

Oliver, W.C. and Pharr, G.M. (1992) An Improved Technique for Determining Hardness and Elastic Modulus Using Load and Displacement Sensing Indentation Experiments. Journal of Materials Research. Vol. 7. Issue 6. pp. 1565-1583.

Oliver, W.C. and Pharr, G.M. (2004) Measurement of Hardness and Elastic Modulus by Instrumented Indentation: Advances in Understanding and Refinements to Methodology. Journal of Materials Research. Vol. 19. No. 1. pp. 3-20.

Oxford Instruments (2016) Educational website. URL: http://ebsd.com/ebsd-explained/basics-of-ebsd/interpreting-the-diffraction-pattern. Referred February 12th 2016.

Pan, C., Wang, R., and Gui, J. (1990) Direct TEM Observation of Microstructures of the Austenitic/Carbon Steels Welded Joint. Journal of Materials Science. Vol. 25. pp. 3281-3285.

Peckner, D. and Bernstein, I.M. (1977) Handbook of Stainless Steels. McGraw-Hill. USA. 800 p. ISBN: 0-07-049147-X.

Peng, Q., Shoji, T., Ritter, S., and Seifert, H.-P. (2005) SCC Behavior in the Transition Region of an Alloy 182-SA 508 Cl.2 Dissimilar Weld Joint under Simulated BWR-NWC Conditions. Proceedings of the 12th International Conference on Environmental Degradation of Materials in Nuclear Power System – Water Reactors. pp. 589-598.

Peng, Q., Shoji, T., Yamauchi, H., and Takeda, Y. (2007) Intergranular Environmentally Assisted Cracking of Alloy 182 Weld Metal in Simulated Normal Water Chemistry of Boiling Water Reactor. Corrosion Science. Vol. 49. pp. 2767-2780.

Peng, Q., Xue, H., Hou, J., Sakaguchi, K., Takeda, Y., Kuniya, J., and Shoji, T. (2011) Role of Water Chemistry and Microstructure in Stress Corrosion Cracking in the Fusion Boundary Region of an Alloy 182-A533B Low Alloy Steel Dissimilar Weld Joint in High Temperature Water. Corrosion Science. Vol. 53. pp. 4309-4317.

Peng, Q., Hou, J., Yonezawa, T., Shoji, T., Zhang, Z.M., Huang, F., Han, E.-H., and Ke, W. (2012) Environnmentally Assisted Crack Growth in One-Dimensionally Cold Worked Alloy 690TT in Primary Water. Corrosion Science. Vol. 57. pp. 81-88.

R6 (2007) Procedure R6 - Revision 4. Nuclear Electric Ltd. Gloucester, UK.

Rajeev, R., Samajdar, I., Raman, R., Harendranath, C.S., and Kale, G.B. (2001) Origin of Hard and Soft Zone Formation during Cladding of Austenitic/Dublex Stainless Steel on Plain Carbon Steel. Materials Science and Technology. Vol. 17. pp. 1005-1011.

Samal, M.K., Balani, K., Seidenfuss, M., and Roos, E. (2009) An Experimental and Numerical Investigation of Fracture Resistance Behaviour of a Dissimilar Metal Welded Joint. Proceedings of the Institution of Mechanical Engineers, Part C: Journal of Mechanical Engineering Science. Vol. 223. No. 7. pp. 1507-1523.

Samal, M.K., Seidenfuss, M., Roos, E., and Balani, K. (2011) Investigation of Failure Behavior of Ferritic-Austenitic Type of Dissimilar Steel Welded Joints. Engineering Failure Analysis. Vol. 18. pp. 999-1008.

Sarikka, T., Ahonen, M., Karjalainen-Roikonen, P., Brederholm, A., Mouginot, R., Saukkonen, T., Nevasmaa, P., and Hänninen, H. (2014) Effect of Strength Mismatch on Fracture Mechanical Behavior of NG-DMW. The International Symposium Fontevraud 8 on Contribution of Materials Investigations and Operating Experience to LWRs' Safety, Performance and Reliability. Avignon, France. SFEN. 15 p.

Sarikka, T., Ahonen, M., Mouginot, R., Nevasmaa, P., Karjalainen-Roikonen, P., Ehrnstén, U., and Hänninen, H. (2016A) Microstructural, Mechanical, and Fracture Mechanical Characterization of SA 508-Alloy 182 Dissimilar Metal Weld in View of Mismatch State. International Journal of Pressure Vessels and Piping. Vol. 145. pp 13-22.

Sarikka, T., Ahonen, M., Mouginot, R., Nevasmaa, P., Karjalainen-Roikonen, P., Ehrnstén, U., and Hänninen, H. (2016B) Effect of Mechanical Mismatch on Fracture Mechanical Behavior of SA 508 – Alloy 52 Narrow Gap Dissimilar Metal Weld. (to be published). 20 p.

Schwalbe, K.-H., Cornec, A., and Lidbury, D. (2004) Fracture Mechanics Analysis of the BIMET Welded Pipe Tests. International Journal of Pressure Vessels and Piping. Vol. 81. pp. 251-277.

Scott, P.M. (1985) A Review of Environment-Sensitive Fracture in Water Reactor Materials. Corrosion Science. Vol. 25. No. 8. pp. 583-606.

Seifert, H.-P., Ritter, S., Shoji, T., Peng, Q.J., Takeda, Y., and Lu, Z.P. (2008) Environmentally-Assisted Cracking Behaviour in the Transition Region of an Alloy182/SA 508 Cl.2 Dissimilar Metal Weld Joint in Simulated Boiling Water Reactor Normal Water Chemistry Environment. Journal of Nuclear Materials. Vol. 378. pp. 197-210.

Shoji, T., Li, G., Kwon, J., Matsushima, S., and Lu, Z. (2003) Quantification of Yield Strength Effects on IGSCC of Austenitic Stainless Steels in High Temperature Water. Proceedings of the 11th International Conference on

Environmental Degradation of Materials in Nuclear Systems. Stevensson, Washington, USA. 10 p.

SINTAP (1999) European SINTAP Procedure. British Steel Report. Sheffield, UK.

Sireesha, M., Shankar, V., Albert, S.K., and Sundaresan, S. (2000) Microstructural Features of Dissimilar Welds Between 316LN Austenitic Stainless Steel and Alloy 800. Materials Science and Engineering: A. Vol. 292. pp. 74-82.

Soares, B., De Abreu Mendonça Schvartzmanm M.M., and Reis da Costa Campos, W. (2007) Characterization of the Dissimilar Welding - Austenitic Stainless Steel with Nickel Alloy Filler Metal. International Nuclear Atlantic Conference. 6 p. ISBN 978-85-99141-02-1.

Sudha, C., Terrance, A.L.E., Albert, S.K., and Vijayalakshmi, M. (2002) Systematic Study of Formation of Soft and Hard Zones in the Dissimilar Weldments of Cr-Mo Steels. Journal of Nuclear Materials. Vol. 302. pp. 193-205.

Thewlis, G., Whiteman, J.A., and Senogles, D.J. (1997) Dynamics of Austenite to Ferrite Phase Transformation in Ferrous Weld Metals. Materials Science and Technology. Vol. 13. pp. 257-274.

Thomas, L.E., Olzsta, M.J., Johnson, B.R., and Bruemmer, S.M. (2009) Microstructural Characterization of Primary Stress-Corrosion Cracks in Alloy 182 Weld from PWR Components and Laboratory Tests. In: Proceedings of the 14th International Symposium on Environmental Degradation of Materials in Nuclear Power Systems - Water Reactors. Breckenridge, Colorado, USA.

Vander Voort, G.F. (1984) Metallography: Principles and Practice. ASM International, Materials Park, Ohio, USA. 752 p. ISBN-13: 978-0871706720.

Vander Voort, G.F. (1989A) Results of an ASTM E-4 Round-Robin on the Precision and Bias of Measurements of Microindentation Hardness Impressions, Factors that Affect the Precision of Mechanical Tests. ASTM STP 1025. ASTM, Philadelphia, USA. pp 3-39.

Vander Voort, G.F. (1989B) Operator Errors in the Measurement of Microindentation Hardness, Accreditation Practices for Inspections, Tests, and Laboratories. ASTM STP 1057. ASTM, Philadelphia, USA. pp 47-77.

Wallin, K. (2011) Fracture Toughness of Engineering Materials – Estimation and Application. EMAS Publishing, Birchwood Park, Warrington, UK. 543 p. ISBN: 0-9552994-6-2.

Wang, G.Z., and Wang, Y.L. (2007) Effects of Loading Rate, Notch Geometry and Loading Mode on the Local Cleavage Fracture Stress of a C-Mn Steel. International Journal of Fracture. Vol. 146. pp. 105-121.

Wang, H.T., Wang, G.Z., Xuan, F.Z., and Tu, S.T. (2011) Numerical Investigation of Ductile Crack Growth Behavior in a Dissimilar Metal Welded Joint. Nuclear Engineering and Design. Vol. 241. pp. 3234-3243.

Wang, H.T., Wang, G.Z., Xuan, F.Z., and Tu, S.T. (2013A) Fracture Mechanism of a Dissimilar Metal Welded Joint ín Nuclear Power Plant. Engineering Failure Analysis. Vol. 28. pp. 134-148.

Wang, H.T., Wang, G.Z., Xuan, F.Z., Liu, C.J., and Tu, S.T. (2013B) Local Mechanical Properties of a Dissimilar Metal Welded Joint in Nuclear Power Systems. Materials Science and Engineering: A. Vol 568. pp. 108-117.

Wang, H.T., Wang, G.Z., Xuan, F.Z., and Tu, S.T. (2013C) An Experimental Investigation of Local Fracture Resistance and Crack Growth Paths in a

Dissimilar Metal Welded Joint. Materials and Design. Vol. 44. pp. 179-189.

Xue, H., Ogawa, K., and Shoji, T. (2009) Effect of Welded Mechanical Heterogeneity on Local Stress and Strain Ahead of Stationary and Growing Crack Tips. Nuclear Engineering and Design. Vol. 239. pp. 628-640.

Yang, J., Wang, G.Z., Xuan, F.Z., Tu, S.T., and Liu, C.J. (2013) Out-of-Plane Constraint Effect on Local Fracture Resistance of a Dissimilar Metal Welded Joint. Materials and Design. Vol. 55. pp. 542-550.

Yang, J., Wang, G.Z., Xuan, F.Z., Tu, S.T., and Liu, C.J. (2014) An Experimental Investigation of In-Plane Constraint Effect on Local Fracture Resistance of a Dissimilar Metal Welded Joint. Materials and Design. Vol. 53. pp. 611-619.

# Appendices

## Appendix A: Stress-strain curves of BWR-DMW tensile specimens
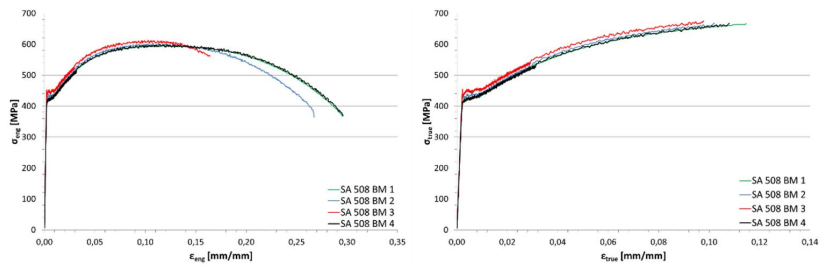


**Figure A.1.** Stress-strain curves of the SA 508 base metal ⌀8 mm round bar specimens.
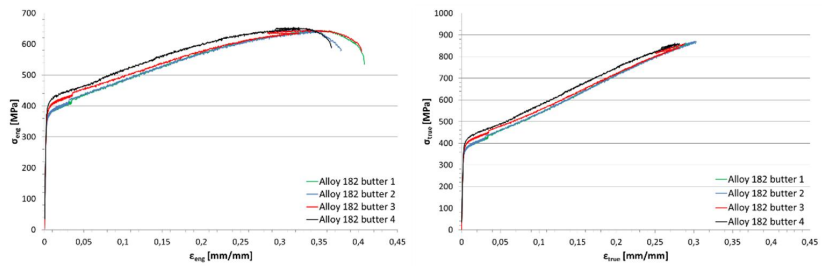


**Figure A.2.** Stress-strain curves of the Alloy 182 buttering ⌀8 mm round bar specimens.
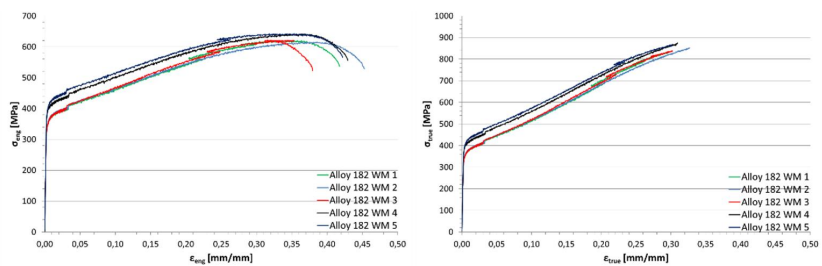


**Figure A.3.** Stress-strain curves of the Alloy 182 weld metal ⌀8 mm round bar specimens.
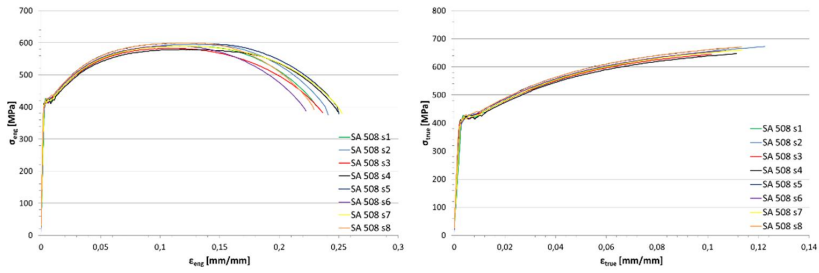
**Figure A.4.** Stress-strain curves of SA 508 base metal 1x2 mm flat-bar specimens.
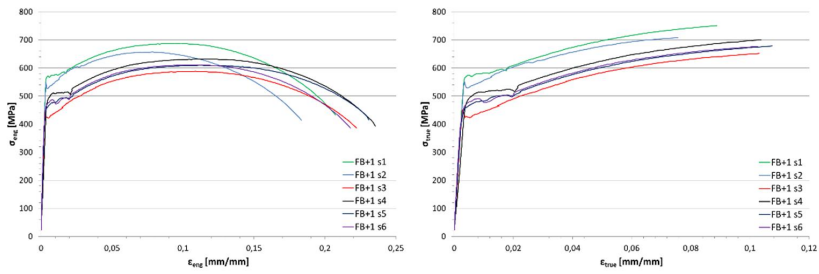


**Figure A.5.** Stress-strain curves of fusion boundary + 1 mm 1x2 mm flat-bar specimens.
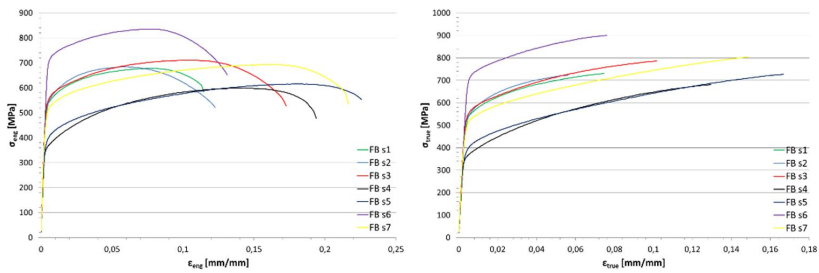


**Figure A.6.** Stress-strain curves of fusion boundary 1x2 mm flat bar-specimens.
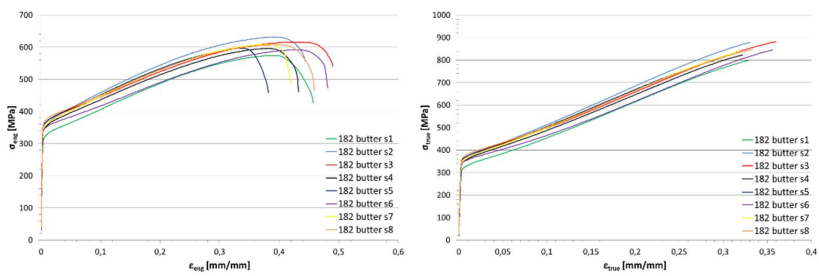


**Figure A.7.** Stress-strain curves of Alloy 182 buttering 1x2 mm flat-bar specimens.
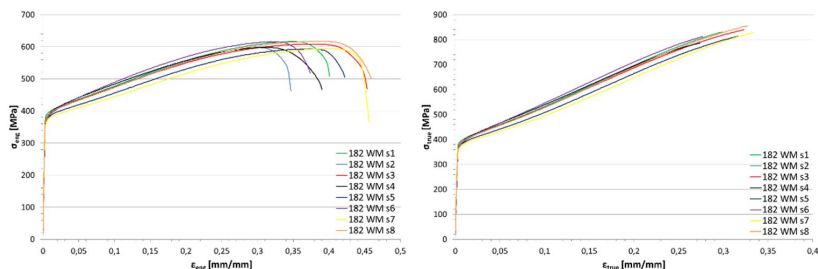
**Figure A.8.** Stress-strain curves of Alloy 182 weld metal 1x2 mm flat-bar specimens.
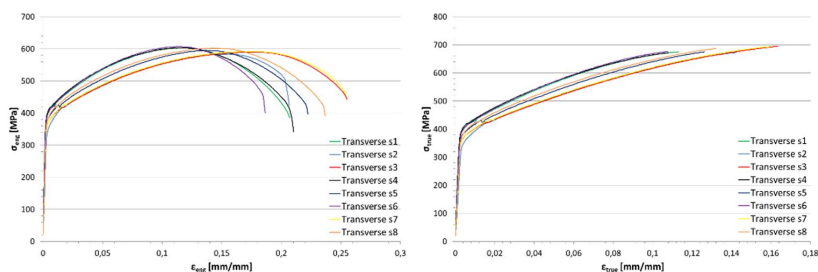


**Figure A.9.** Stress-strain curves of transverse 1x2 mm flat bar-specimens.

## Appendix B: Stress-strain curves of NG-DMW tensile specimens
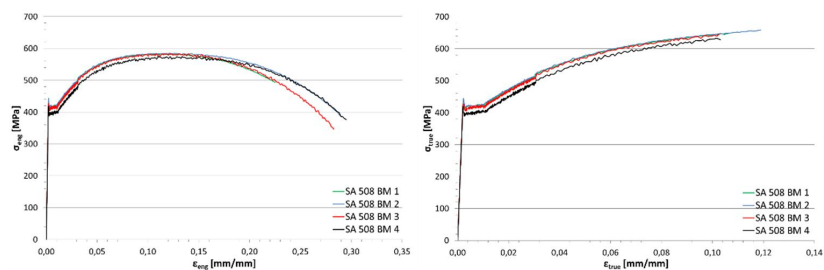


**Figure B.1.** Stress-strain curves of SA 508 base metal ⌀8 mm round bar specimens.
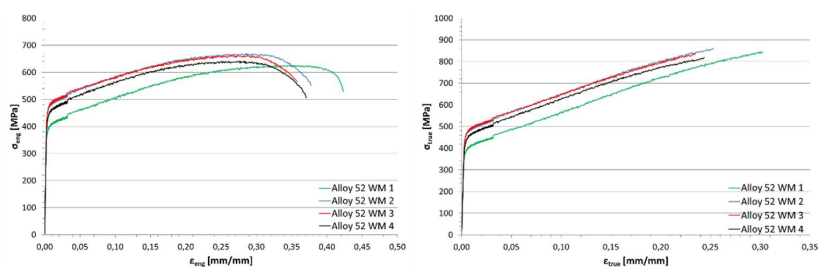


**Figure B.2.** Stress-strain curves of Alloy 52 weld metal ⌀8 mm round bar specimens.
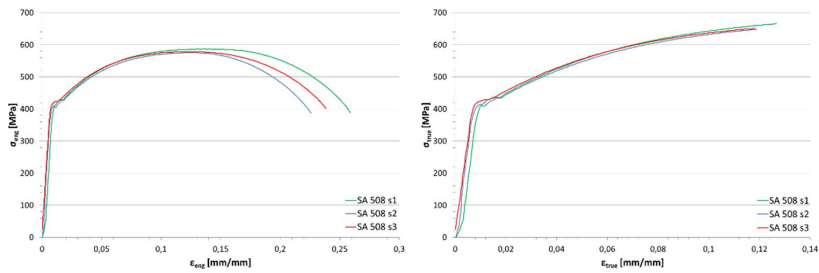
**Figure B.3.** Stress-strain curves of SA 508 base metal 1x2 mm flat-bar specimens.
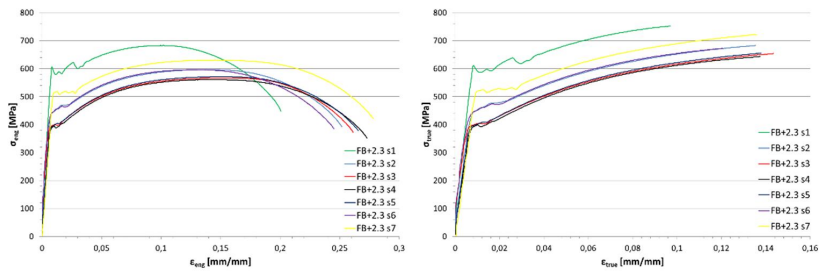


**Figure B.4.** Stress-strain curves of fusion boundary + 2.3 mm 1x2 mm flat-bar specimens.
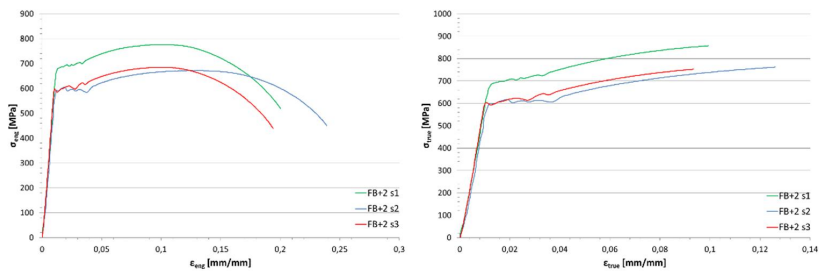


**Figure B.5.** Stress-strain curves of fusion boundary + 2 mm 1x2 mm flat-bar specimens.
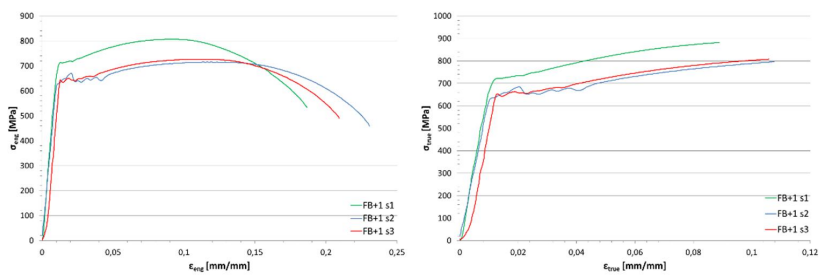


**Figure B.6.** Stress-strain curves of fusion boundary + 1 mm 1x2 mm flat-bar specimens.
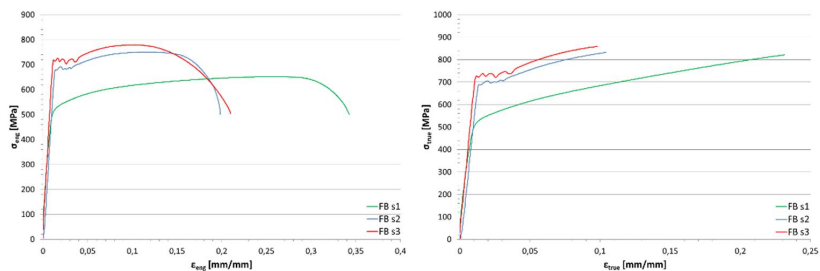
**Figure B.7.** Stress-strain curves of fusion boundary 1x2 mm flat-bar specimens.
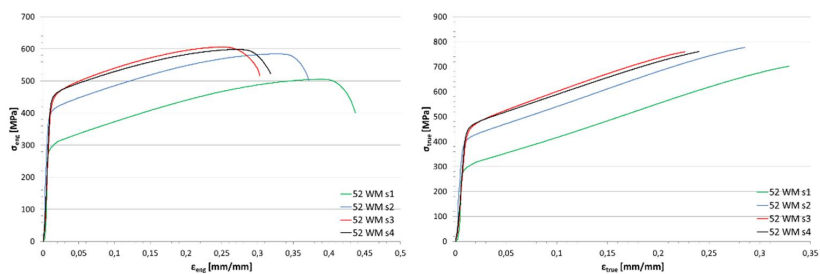


**Figure B.8.** Stress-strain curves of Alloy 52 weld metal 1x2 mm flat-bar specimens.
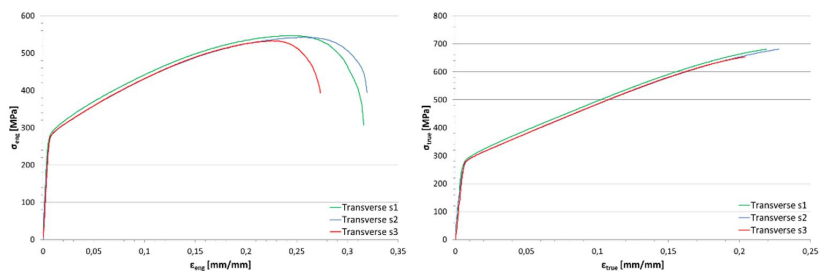


**Figure B.9.** Stress-strain curves of transverse 1x2 mm flat-bar specimens.

## Appendix C: J-R curves of BWR-DMW fracture mechanical specimens
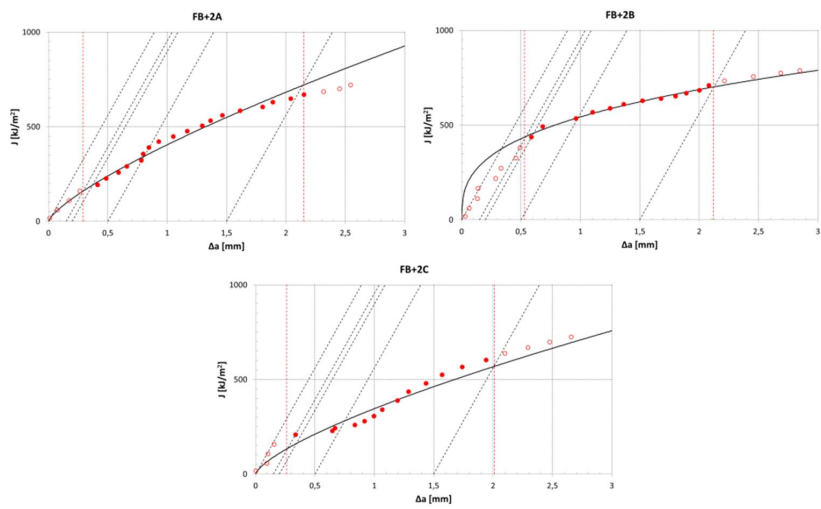


**Figure C.1.** J-R curves of the SA 508 HAZ specimens.
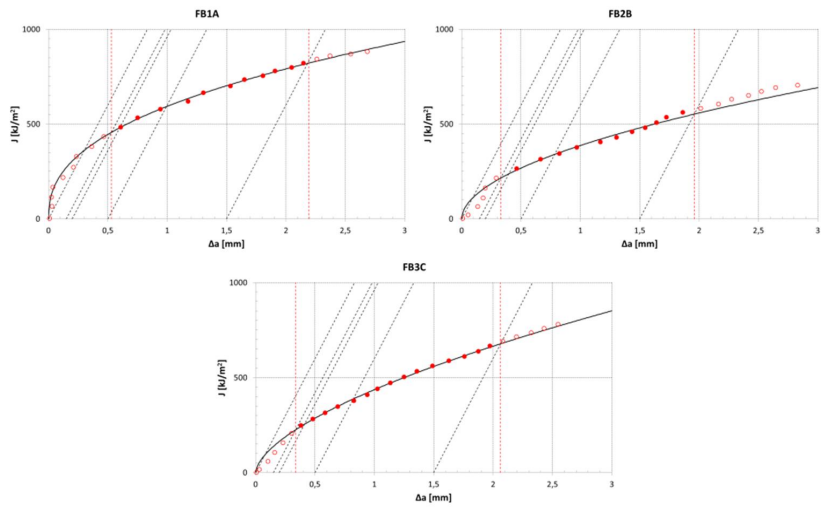


**Figure C.2.** J-R curves of the fusion boundary specimens.
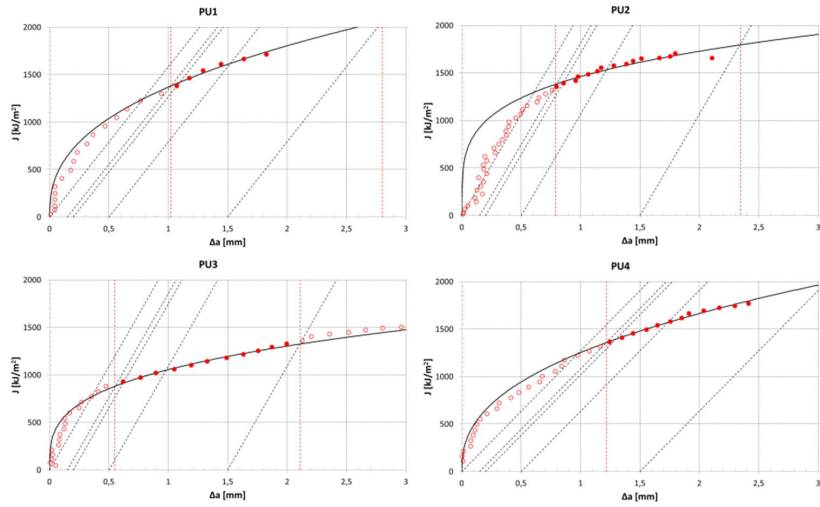
**Figure C.3.** J-R curves of the Alloy 182 buttering layer specimens.
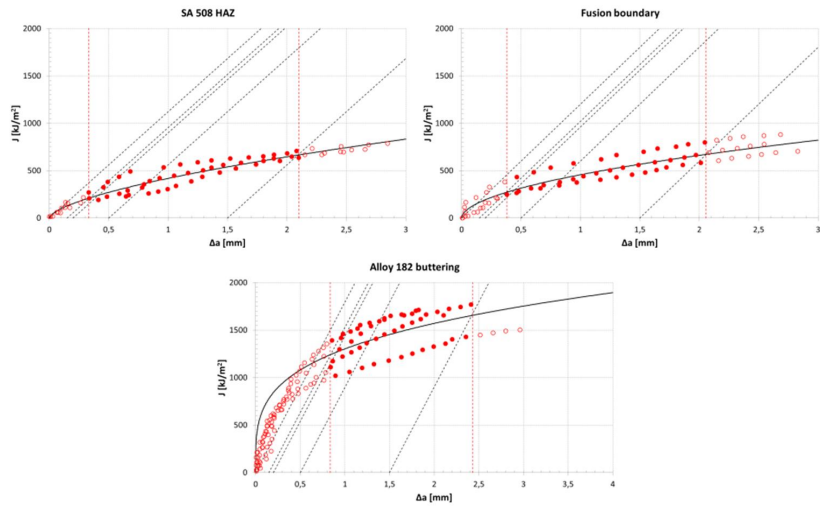


**Figure C.4.** J-R curves of tested BWR-DMW zones calculated using J versus crack extension points of all the tested specimens from the specific zone.

# Appendix D: J-R curves of NG-DMW fracture mechanical specimens
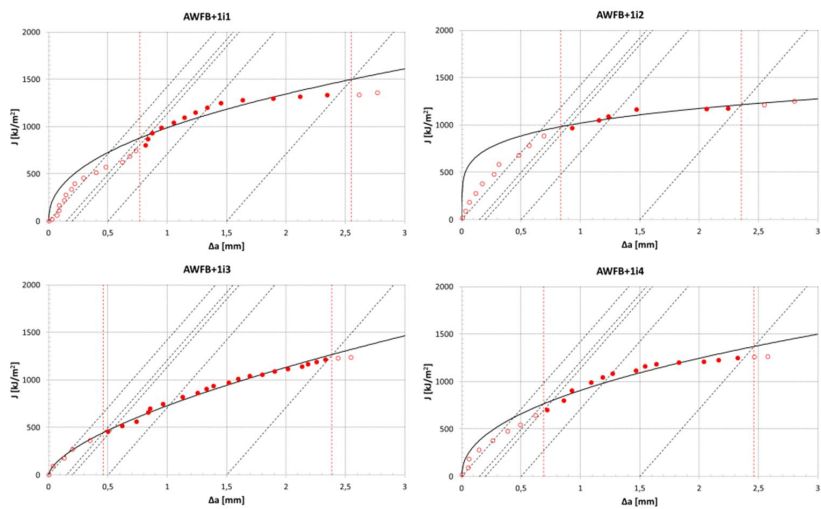


**Figure D.1.** J-R curves of the as-welded condition SA 508 HAZ specimens.
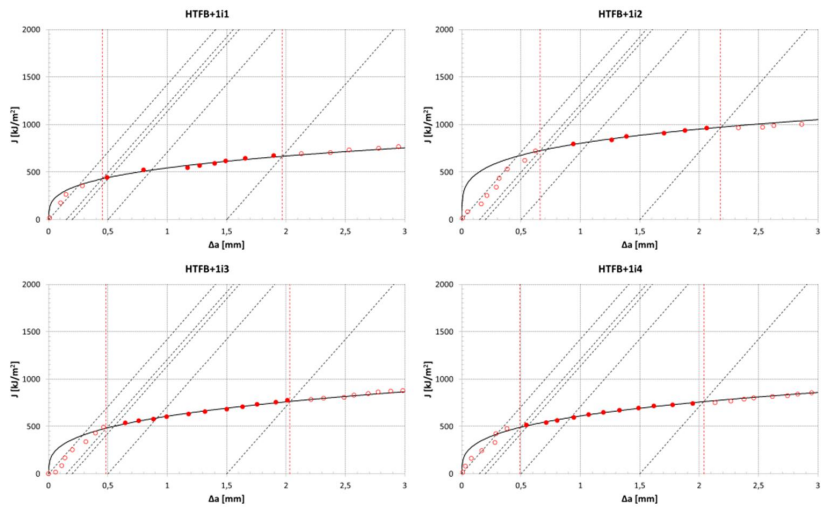


**Figure D.2.** J-R curves of the PWHT condition SA 508 HAZ specimens.
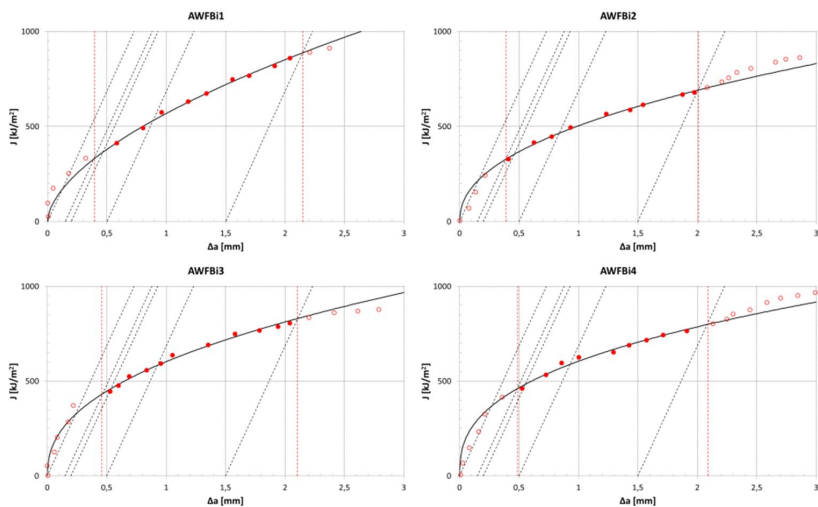
**Figure D.3.** J-R curves of the as-welded condition fusion boundary specimens.
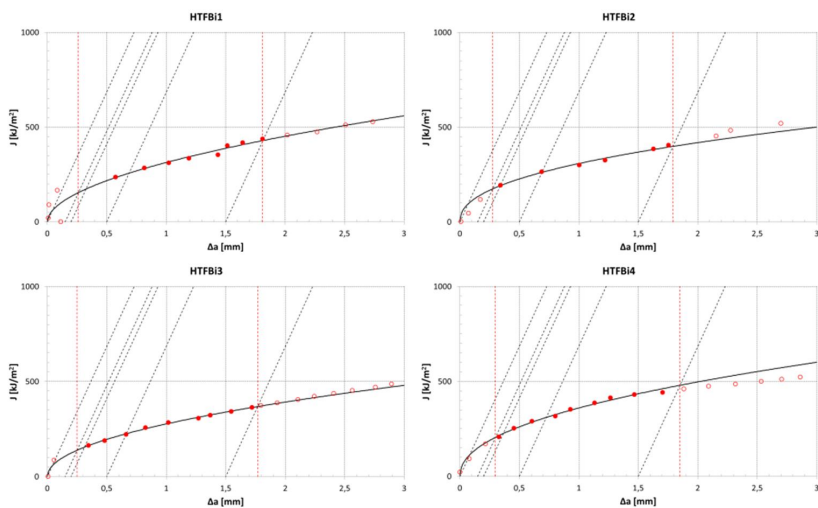


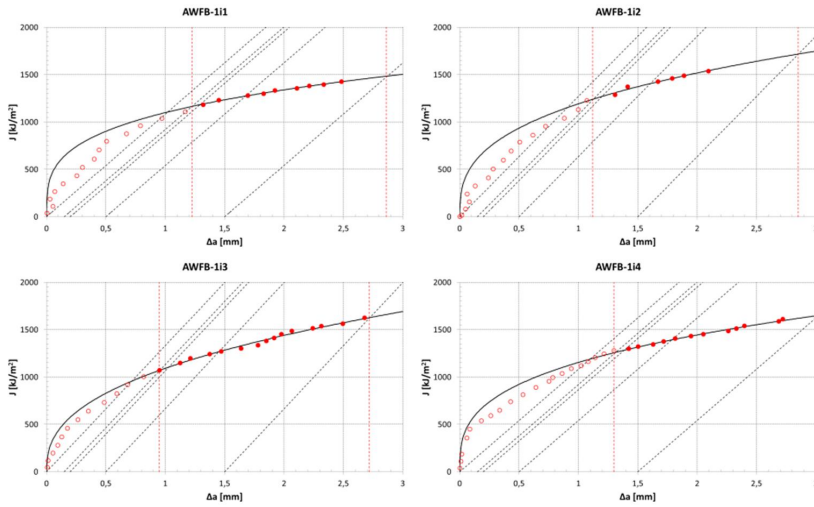**Figure D.4.** J-R curves of the PWHT condition fusion boundary specimens.

**Figure D.5.** J-R curves of the as-welded condition Alloy 52 weld metal specimens.
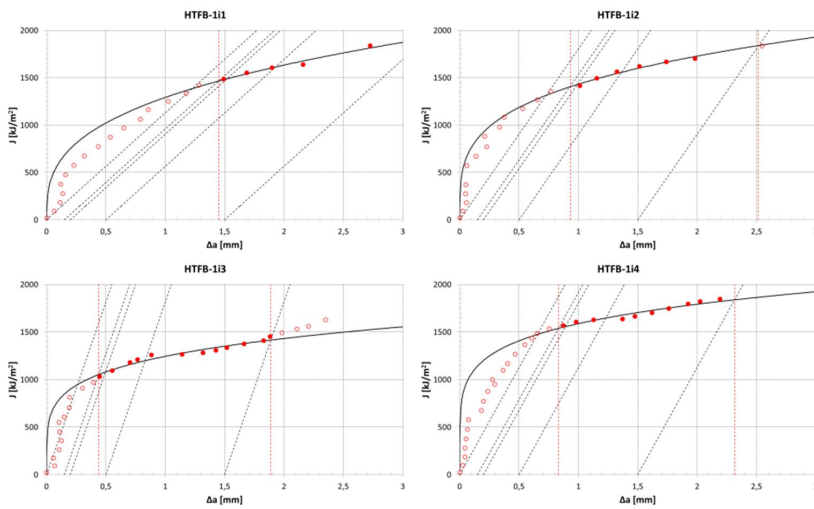


**Figure D.6.** J-R curves of the PWHT condition Alloy 52 weld metal specimens.
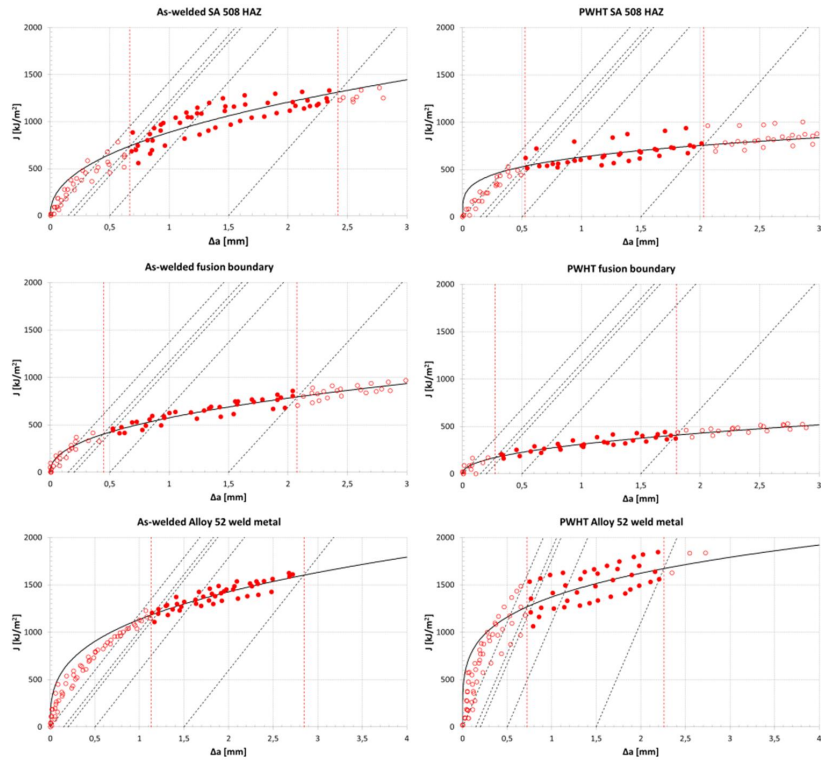
**Figure D.7.** J-R curves of tested NG-DMW zones calculated using J versus crack extension points of all the tested specimens from the specific zone.

Ferritic steels are used as the structural material of the nuclear power plant reactor pressure vessels because of their relatively good mechanical properties and low cost whereas austenitic stainless steels are used in components in which a good corrosion resistance is mandatory. The simultaneous use of these two types of crystallographically different materials makes the presence of dissimilar metal welds in nuclear power plants obligatory. One of the most critical dissimilar metal weld in a nuclear power plant is the one joining the reactor pressure vessel through its nozzle to the main coolant piping using a transition piece called safe-end. In this thesis, the microstructure and mechanical properties of two different weld mock-ups representing the Ni-base safe-end dissimilar metal welds used in commercial light water reactor pressure vessel designs are examined and the effect of the microstructure and mechanical properties on the fracture mechanical behavior of the ferrite-austenite interface of each studied dissimilar metal weld is determined.

BUSINESS +
ECONOMY

ART +
DESIGN +
ARCHITECTURE

SCIENCE +
TECHNOLOGY

CROSSOVER

**DOCTORAL
DISSERTATIONS**